Chapter II.6

Superconducting magnets

Paolo Ferracin
LBNL, Berkeley, USA

This chapter summarizes the material covered on this subject during a course of about eight hours to provide an introduction on superconducting magnets for particle accelerators, and in particular dipole and quadrupole magnets, with low-temperature superconducting materials. The course, focusing on the basic principles, physical parameters, and analytical and numerical tools related to superconducting magnet design, is subdivided in five parts. After a brief introduction in Section II.6.2 on the function of dipole and quadrupole magnets in particle accelerators, Section II.6.3 discusses the properties and characteristics of the superconducting strands and cables, with emphasis on the motivations behind their design features and dimensions. The main concepts governing the magnetic design are dealt in Section II.6.4, starting from the analytic description of field profiles, proceeding with the explanation of field errors and their minimization, and concluding with an overview of different coil configurations. The mechanical aspects of superconducting magnet are then presented in Section II.6.5, with focus on all the components used to contain the electro-magnetic forces and to manage the resulting stresses. Finally, in Section II.6.6, we will deal with the quench phenomenon and with the systems designed to protect the magnet when superconductivity is lost. A case study, composed by exercises aimed at the conceptual design of a 11 T dipole magnet, is also included at the end of the chapter, and solutions are provided.

II.6.1 Introduction

Superconducting magnets for particle accelerators, are an extremely fascinating technology and a beautiful research topic. This statement may sound biased, considering that the author has spent by now the vast majority of his professional career working on such magnets.

However, the statement can be understood if one considers the very broad spectrum of scientific and technical disciplines involved in the development of this technology: they range from chemistry and material science (the superconducting materials), to quantum physics (the key mechanisms that explain superconductivity), to electro-magnetism (magnets produce high quality magnetic fields with electrically powered windings), to cryogenics (superconductors need to operate at very low temperatures). In addition, a second very fascinating aspect is the fact that superconducting magnet technology covers a very large spectrum of physical dimensions (see Fig. II.6.1): as a simple example, one can mention the diameter of the superconducting filaments where the current flows (few microns), the dimensions of magnets (meters), and the size of accelerators (km).

This chapter summarizes the material covered on this subject during a course of about eight hours aimed at providing an introduction on superconducting magnets for particle accelerators. The course was

This chapter should be cited as: Superconducting magnets, P. Ferracin, DOI: 10.23730/CYRSP-2024-003.1155, in: Proceedings of the Joint Universities Accelerator School (JUAS): Courses and exercises, E. Métral (ed.),
CERN Yellow Reports: School Proceedings, CERN-2024-003, DOI: 10.23730/CYRSP-2024-003, p. 1155.

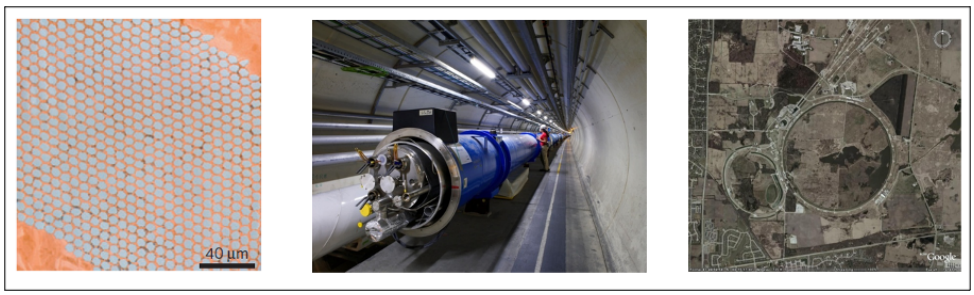

Fig. II.6.1: Orders of magnitude in superconducting magnet technology: from left to right, superconducting filaments (µm), superconducting magnets (m), particle accelerators (km).

subdivided in four main sub-sections of two hours each which followed essentially the life of a magnet (see Fig.II.6.2), starting from superconducting materials and practical superconductors, and continuing to magnetic design and fabrication of coils, followed by mechanical design and fabrication of the cold-mass, and concluding with magnet powering, and the description of quench phenomena and protection systems.

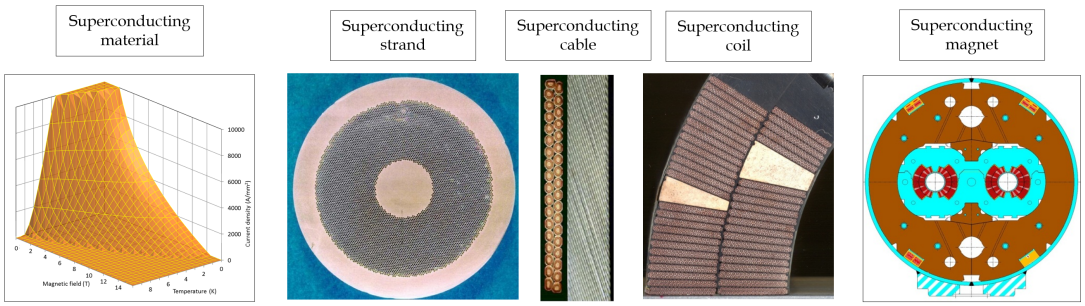

Fig. II.6.2: From superconducting materials to superconducting magnets.

II.6.1.1 Further readings

Because of the limited time, this class is aimed at providing a preliminary introduction on the many scientific and technological aspects governing the magnet design. It was intended for students and researchers who plan to start working on superconducting magnets, and would like to have a first overview of this beautiful technology. The course material is fundamentally a short summary of a series of more detailed lectures that were given at the U.S. Particle Accelerator School [1] from 2009 to 2015, and of the "Masterclass of Design of superconducting magnets for particle accelerators" given at CERN by Ezio Todesco in 2020 during the first wave of Covid-19 pandemic [2]. Additional key references for this course notes are the books considered fundamental tools by any superconducting magnet designers, namely the ones written by Martin N. Wilson [3], by K.-H. Mess, P. Schmuser, S. Wolff [4], and by F.M. Asner [5]. Besides other texts that can be a reference and whose material are also used during the course are: A. Devred [6] on practical superconductors; S. Russenschuck [7] and S. Izquierdo Bermudez [8] on field quality; D. Shoerling and A. Zlobin [9] and the LHC design report [10] on magnet design and fabrication; E. Todesco on quench stability and quench protection [11]. Note that all

equations in these notes are given for the international system (m, kg and A), unless specifically stated. Practical units (for instance, A/mm^2 rather than A/m^2—or MPa rather than Pa) are also used.

II.6.2 Particle accelerators and magnets

In synchrotron colliders, two counter rotating beams are present, sharing the same beam pipe if they accelerate particles and antiparticles (as Tevatron), or two different beam pipes if they accelerate the same type of particles (as LHC). In a synchrotron collider, i.e. CERN LHC, two beams of charged particles are accelerated in a circular path, one clock-wise and the other anti-clock wise. The charged particle trajectory is bent in the magnetic arcs made up by many magnets (see Fig. II.6.3) by a force (called electro-magnetic (e.m.) force, or Lorentz force) perpendicular to the trajectory and given by

$$\vec{F} = q\,\vec{v} \times \vec{B} \quad , \tag{II.6.1}$$

where $\vec{v}$ is the particle velocity and the $\vec{B}$ is the magnetic field. The elctric charge q indicates the charge and its sign (positive or negative). Here we treat the simpler case of a proton (or ion) with charge e.

The particles are accelerated in a straight part of the accelerator, indicated as straight section (SS), see Fig. II.6.3, by an electric force produced by an electric field $\vec{E}$. The electric force is defined as:

$$\vec{F} = q\,\vec{E} \quad . \tag{II.6.2}$$

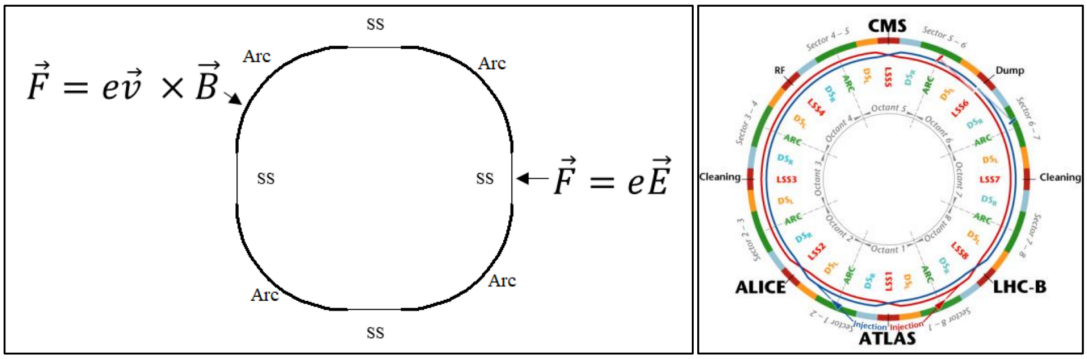

Fig. II.6.3: Schematic view of a synchrotron (left), and of the LHC accelerator (right).

The magnetic field in the arc is produced by magnets, while the electric field in the straight section is produced by so-called RF cavities.

The key feature of a synchrotron is the fact that the particles are driven in the same accelerating structure many times also during the acceleration. Turn after turn, the particles are accelerated when they cross the accelerating cavities (RF cavities) and the magnetic field increases simultaneously ("synchro") to keep the beam in a circular orbit. The maximum energy that particles can achieve is proportional to the magnetic field and to the size of the accelerator, specifically

$$p = e\,B\,\rho \quad , \tag{II.6.3}$$

where p is the momentum of the particle, and ρ is the curvature radius of the accelerator. For proton and electrons in the ultra-relativistic regime (with a speed very close to the speed of light), the energy of the particles in the synchrotron can be approximated as

$$E[\mathrm{GeV}] \;=\; 0.3\, B[\mathrm{T}]\, \rho[\mathrm{m}] \quad . \tag{II.6.4}$$

From this very simple but fundamental expression one can clearly understand why high energy collisions can be reached only by with very high magnetic field or very large accelerators (or possibly both). Therefore, the push for higher and higher fields is a common goal of any designer working on accelerator magnets to obtain more compact and possibly cheaper accelerators. Another interesting conclusion that we can draw from Eq. (II.6.4) is that magnet designers working on circular colliders have to deal with two parameters ($B[\mathrm{T}]$ and $\rho[\mathrm{m}]$) that contribute only linearly to the collision energy. From this point of view there is a clear disadvantage, if one compares accelerators to other applications of superconducting magnets. For example, in large accelerator detectors like CMS and ATLAS at the LHC, the momentum resolution, one of the key parameters of a detector, increases with $B[\mathrm{T}]\, L^2[\mathrm{m}]$, L being the size of the magnetic field. This explains why detectors magnets are among the biggest superconducting magnets ever built. For example on another parameter that will be discussed later, if one considers superconducting magnets for fusion applications, (i.e. in a Tokamak) the fusion magnetic power per unit volume is proportional to B^4. The image shown in Fig. II.6.3 represents a simplification of a very complex machine which is a particle accelerator. In reality, if we look at the LHC, which is 26.7 km long, we have

- the arcs (20.5 km in total), with dipoles for bending, quadrupoles for focusing, and corrector magnets,
- the long straight sections (LSS), 6.2 km in total. In the LSS one finds the interaction regions (IR) where experiments can be performed equipped with quadrupoles for strong focusing in the interaction points and dipoles when the beams of a two-ring machine merge in one vacuum pipe. Other uses of LSS are beam injection (dipole kickers), accelerating structures (RF cavities), beam dump (dipole kickers) and beam cleaning (collimators).

In the next two sections we will focus on the two most important magnets in a particle accelerator: the bending dipole magnets and the focusing quadrupole magnets.

II.6.2.1 Dipole magnets

The main function of the bending magnets is steer the particles on a circular orbit. When a particle beam enters the beam pipe of a dipole magnet (see Fig. II.6.4, top left), it encounters a vertical magnetic field generated by the coil.

These dipoles are referred to as electro-magnets, since the magnetic field is generated by the electric current that flows in the coils. The vertical field acting on the moving charged particle generates a Lorentz force that bends its trajectory. With a sequence of properly placed dipole magnets it is possible to keep the particle trajectory on a circular path (see Fig. II.6.4 bottom left). The cross section of the coil in a plane perpendicular to the particle trajectory (located in the centre of the coil coil straight section),

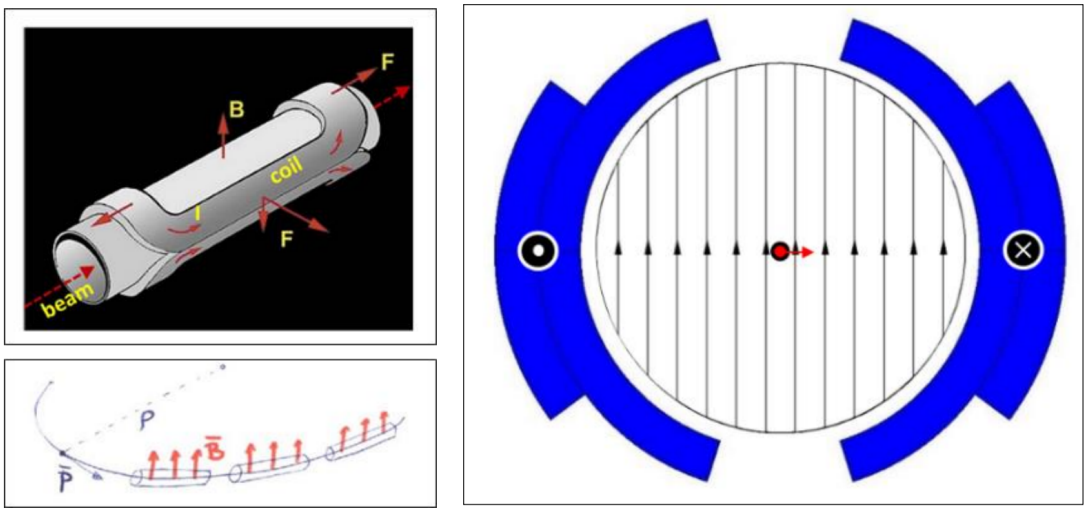

Fig. II.6.4: Dipole magnet coil (top left), series of magnets in a particle accelerator (bottom left), and dipole coil cross-section (right) with flux lines, and the direction of the Lorentz force on a proton entering the figure.

an LHC coil generally appears as in Fig. II.6.4 (right). The vertical lines are the magnetic flux lines and the red arrow represent the e.m. force on the proton (positive charge) moving inwards (entering the page). The magnetic field inside the coil aperture can be expressed as

$$B_y \propto j\, w \quad , \tag{II.6.5}$$

where j is the overall current density in the coil and w is the coil width. Therefore, one can conclude that in order to maximize the energy of the particle beam in a circular accelerator one needs to maximize B, and in order to maximize B, if we consider electro-magnets, one has to make very large coils, and/or increase as much as possible j.

II.6.2.2 Quadrupole magnets

The second type of magnets which play a fundamental role in a circular synchrotron accelerator are the quadrupole magnets. They are characterized by four coils (see Fig. II.6.5 top left). Their cross-section is also shown in the centre and right panel of the figure.

A quadrupole magnet produces a field whose value is zero in the centre and that increases linearly while moving out of the center towards the coil. The key parameter is therefore not the bore field like in the dipole magnets, but the field gradient G [T/m]. For the quadrupoles when a proton traverses them in the centre there is no force acting on it. But if the trajectory is not in the centre, a proton will feel a force that will either push it towards the centre or farther from it. In fact, depending on the directions of the current flowing in the coils, a quadrupole will focus vertically (i.e. move the trajectory closer to the axis) and de-focus horizontally (Fig. II.6.5, centre), or vice-versa (Fig. II.6.5, right). One can demonstrate that a succession of focusing and de-focusing quadrupoles in the arc (the arc quadrupoles, shown in Fig. II.6.5 bottom left) have the function of stabilizing the beam, by moving the resulting trajectory closer to the central axis (orbit). For example, if we consider again the LHC, at collision energy, two beams circulate,

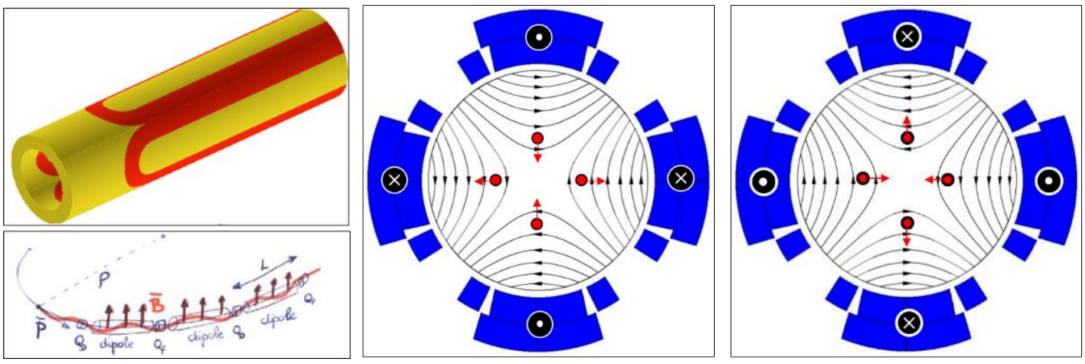

Fig. II.6.5: Rendition of a quadrupole magnet coil (panel at top left), sequence of dipoles and quadrupole magnets in a particle accelerator (panel at bottom left), and quadrupole coil cross-section with flux lines in vertical focusing (panel at centre) and in de-focusing mode (panel at right), proton particles and the direction of the Lorentz forces are indicated by the red dots and the arrows.

each with 2800 bunches. A bunch can be described as a cloud of about 120 billion protons, with a length of 40 cm and a diameter of 1–2 mm (see Fig. II.6.6). The bunches travel at a speed very close to the speed of light and are about 7.5 m, or 25 ns, apart. The function of the arc quadrupole is to prevent the proton in a bunch from spreading, and keep their size stable while turning in the accelerator.

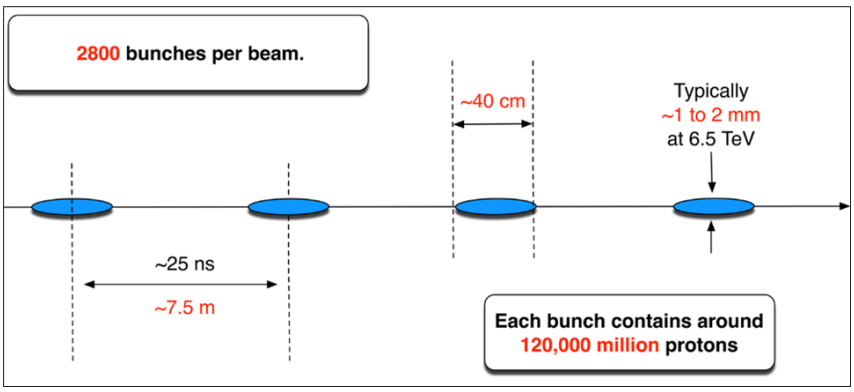

Fig. II.6.6: Bunch size and spacing in the LHC arc (image from M. Lamont). As already mentioned for the dipole magnets, also for the quadrupole magnets the gradient is proportional to the width of the coil and to the current density. Therefore, also in this case, in order to maximize the focusing strength of the quadrupole electro-magnet, one has to make very large coils, and/or increase as much as possible j.

A second family of quadrupole are the interactions regions (IR) quadrupoles. In the IR (see Fig. II.6.7, left), the two beams, which in the arc travel in two separate beam tubes, are bent by two dipoles magnets (the IR dipole magnets), placed on the same axis, and then focused by the IR quadrupole magnets (also called triplets or low-β quadrupoles). The goal of this final focus, is to "compress" the bunches in the transverse plane at the interaction points (IP) in order to maximize the rate of collisions between protons during bunch crossing (a key parameter of the accelerator called luminosity). In the LHC, the IR quadrupole magnets contribute to focus the bunches from a transverse dimension of 1–2 mm to about 20 µm (see the right panel in Fig. II.6.7).

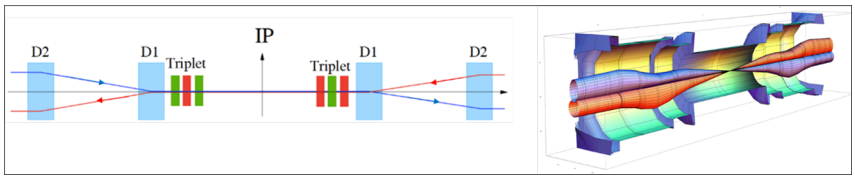

Fig. II.6.7: Left: schematic view of the Interaction Regions (IR), with the IR dipole magnets (D1 and D2), the IR quadrupole magnets (Triplets), and the Interaction Point (IP). Right: beam envelope in the IR.

Similarly to what we said about the dipole magnets, also for the quadrupole magnets the gradient is linked to the width of the coil and to the current density. Therefore, also in this case, in order to maximize the focusing strength of the quadrupole electro-magnet, one has to make very large coils, and/or increase j as much as possible.

It becomes therefore clear why superconducting materials, which allow to increase significantly j with respect to normal conducting materials like Cu (a factor of 100), are extremely attractive for high energy circular colliders.

II.6.3 Superconductivity and practical superconductors

Superconductivity was discovered in 1911 by Kamerlingh Onnes who observed that the resistance of a mercury wire disappeared (not just "little" resistance, but truly ZERO resistance) at 4.2 K (see Fig. II.6.8) . The temperature at which the transition from the normal (resistive) conducting state to the superconducting (non resistive state) takes place is the critical temperature T_c. Below T_c a superconducting material is superconductive, above T_c a superconducting material is normally conductive. This property is in reality observed in many materials (for example aluminium, cadmium, lead, tin, titanium...), but, strangely enough, not in the materials which are the best as normal conductors (copper, silver, gold ...). A second peculiar feature of superconducting materials is that at the temperature above T_c a superconductor is a very poor conductor. This second property has significant consequences on the protection of the superconducting material, as we will see in Section II.6.4.

Superconducting materials can be classified in two main groups, depending on their behaviour when an external magnetic field is applied: Type I and Type II [6].

II.6.3.1 Type I superconductors

After the observation of the disappearance of mercury resistivity in 1911, the second major discovery related to superconducting materials was in 1933 with the Meissner-Ochsenfeld effect. It is observed that at $T < T_c$, a superconducting material becomes perfectly diamagnetic. This means that the magnetic field is completely expelled, as shown in Fig. II.6.9.

The figure indicates that this phenomenon happens both when an external magnetic field is applied below T_c , and when a superconducting material is already in a field at $T > T_c$ (therefore still in the normal conducting state) and the temperature is lowered below T_c. In the first case, the expulsion of the magnetic field can be explained by the fact that when we ramp an external magnetic field, we

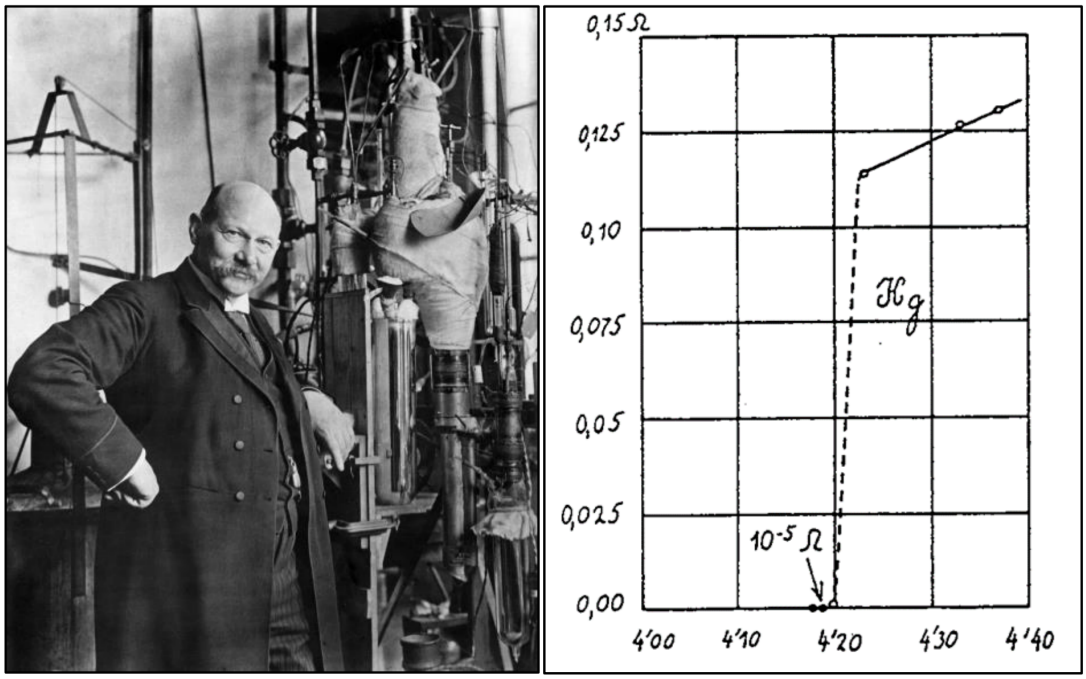

Fig. II.6.8: Kamerlingh Onnes in 1911, with the first device allowing He liquefaction (left) and resistance of mercury as a function of temperature (right). The device is at the museum Boerhaave in Leiden, The Netherlands.

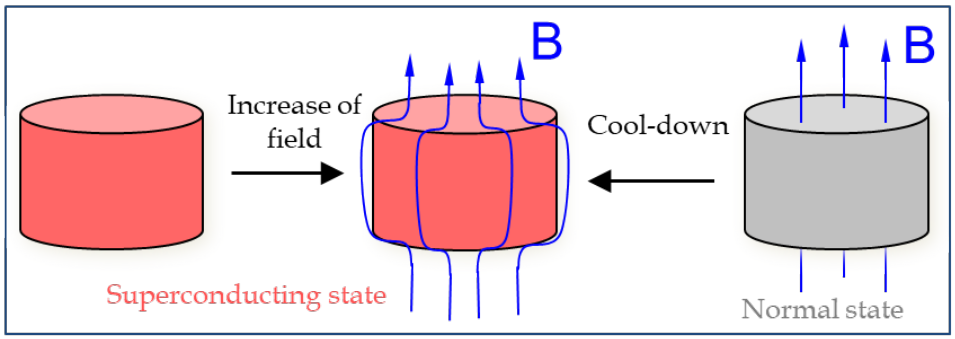

Fig. II.6.9: Representation of a Meissner-Ochsenfeld effect: the magnetic field is completely expelled from the superconducting material (courtesy of L. Bottura).

generate eddy currents in the superconductor. These eddy currents are permanent (they do not decay since the resistivity is null) and therefore they permanently shield the field. The second case, the behaviour cannot be explained with non-decaying eddy-currents, and it is a specific and unique property of the superconducting material.

A side effect of the Meissner-Ochsenfeld effect is that this behaviour and more in general the superconductivity itself takes place only if the external field B is lower than a critical field B_c. In other words, superconductivity is lost not only when the temperature is beyond a certain value, but also when the magnetic field passes a critical limit, which differs depending on the materials. Unfortunately, the first discovered superconductors (called Type I) had an extremely low $B_c(\leq\ 0.1\ T)$, which made them

unsuitable for magnet applications above what can be obtained by iron dominated magnets (2 T).

II.6.3.2 Type II superconductors

In the 1950's, a second generation of superconducting materials, called Type II, was discovered. Type II superconductors are characterized by a different behavior towards the magnetic field, and in particular by the presence of two different critical fields: B_{C1} and B_{C2}. Below B_{C1}, the field is totally expelled, as we explained before for the Type I superconductors. Between B_{C1} and B_{C2}, the Type II superconductors enter in a mixed phase, where the magnetic field penetrates the material as flux tubes called fluxoids. Each fluxoid has a flux of $\phi_0 = \frac{h}{2e} = 2 \times 10^{-15}$ Wb. This behavior is schematically depicted in Fig. II.6.10, and was observed in a photo by Essmann & Träuble in 1967 and more recently with magneto-optical imaging technique at the Oslo University (see Fig. II.6.11 right). Finally, with a field above B_{C2}, the superconductivity is lost.

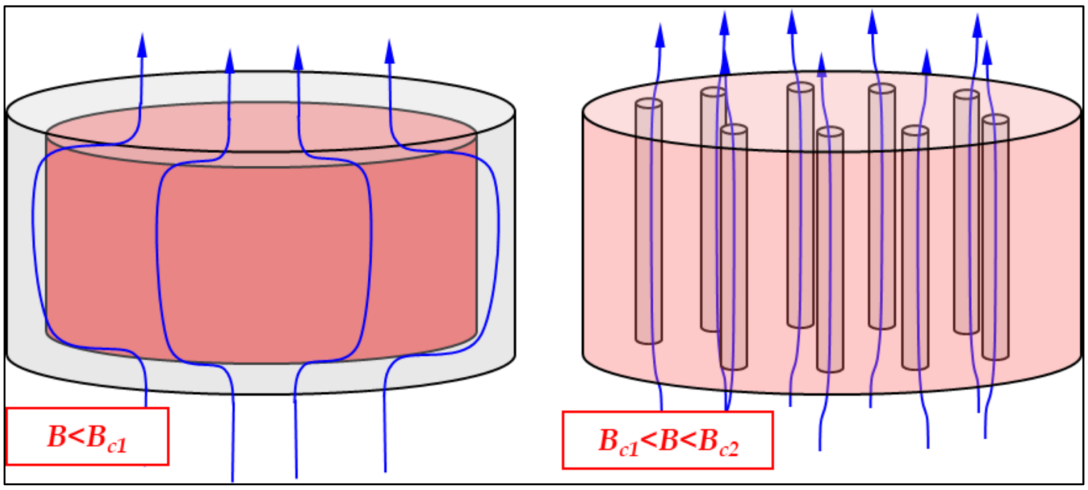

Fig. II.6.10: B flux penetration in a Type II superconductor (courtesy of L. Bottura).

It is important to point out that the critical field is linked to the temperature, i.e. B_{C2} and T_c values are connected. More specifically, the critical temperature is reduced when a magnetic field is applied, and similarly the maximum field that a Type II superconductor can withstand increases by lowering the temperature.

The key advantage of Type II superconductors is that the critical field B_{C2} becomes significantly higher than that for Type I superconductor (from mT to T). However, a second effect is observed, this time related to the circulating current. In fact, if a current density j passes through a Type II superconductor in a field comprised between B_{C1} and B_{C2}, a Lorentz force, given by $F = j \times B$, starts acting on the fluxoids. The force determines a motion of the tubes, which results in a change of the field inside the superconductor. The flux motion, i.e. a $\frac{dB}{dt}$ within the conductor, generates a voltage V, which, in the presence of a current I, causes a dissipation ($V\,I$). In other words, the effect of the flux motion in the superconductor produces flux motion resistance, and so, even if the current flows without dissipation, the superconducting is actually dissipating heat as if we were in the presence of ohmic heating. In order to avoid this motion, the fluxoids can be locked in pinning centres, which are defects or impurities pur-

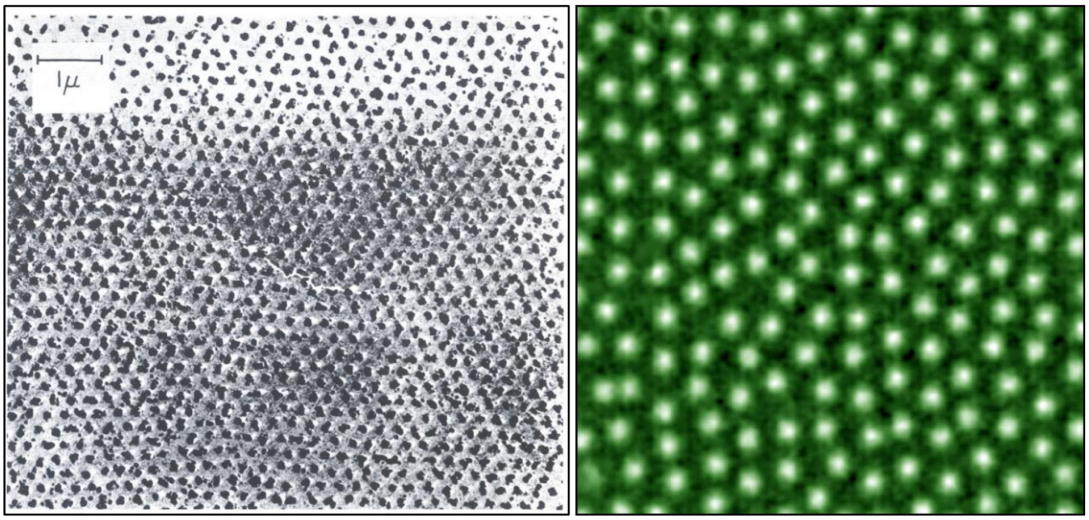

Fig. II.6.11: The pattern of fluxoids was observed in a famous photo by Essmann & Träuble in 1967 (left) and more recently with magneto-optical imaging technique at the Oslo University (right). In the left photo, the pattern "was revealed by particles of ferromagnetic materials which located themselves where the magnetic flux intersects the surface".

posely added during the fabrication of the superconductor. The pinning centres exert a pinning force F_p, which locks the fluxoids in place. As long as $F_p \geq j \times B$, no flux motions and no dissipation occur. We can therefore define a third parameter, the critical current density of the superconductor j_c, which is the current density at which, for a given B and at a given T the pinning force is overcome by the Lorentz force. When $j > j_c$, the superconductivity is lost.

In the same way as a link between B_c and T_c exist, also the critical current j_c depends on the other two parameters. In a three dimensional space one can create a surface linking together B_c, T_c, and j_c. This surface is shown in Fig. II.6.12 for Nb-Ti and Nb_3Sn, and is called critical surface. When operating below the critical surface, a superconducting material is in the superconducting state. When above the critical surface, a superconducting material is in the normal-conducting state.

II.6.3.3 Superconducting materials

Nb-Ti and Nb_3Sn, discovered respectively in 1954 and 1961, are the most commonly used Type II superconductors (80–90% of all devices). Since their critical temperature T_c is 9 K (for Nb-Ti) and 18 K (for Nb_3Sn), they are defined as low T superconductors. A more recent family of superconductors, called High Temperature Superconductors (HTS) have a higher T_c, up to 80–120 K and they are not covered here.

II.6.3.3.1 Nb-Ti

Nb and Ti combine in a ductile alloy (called β phase), which is therefore easy to process by extrusion and drawing techniques. T_c and B_{C2} depend on the Ti titanium content. the optimal is 46.5–47% in weight. The T_c is $\sim$ 9.2 K at 0 T, and B_{C2} is $\sim$ 14.5 T at 0 K. The critical current density j_c depends on the microstructure, and α_{T_i} phase is used for flux pinning and obtained by cold works and heat treatments.

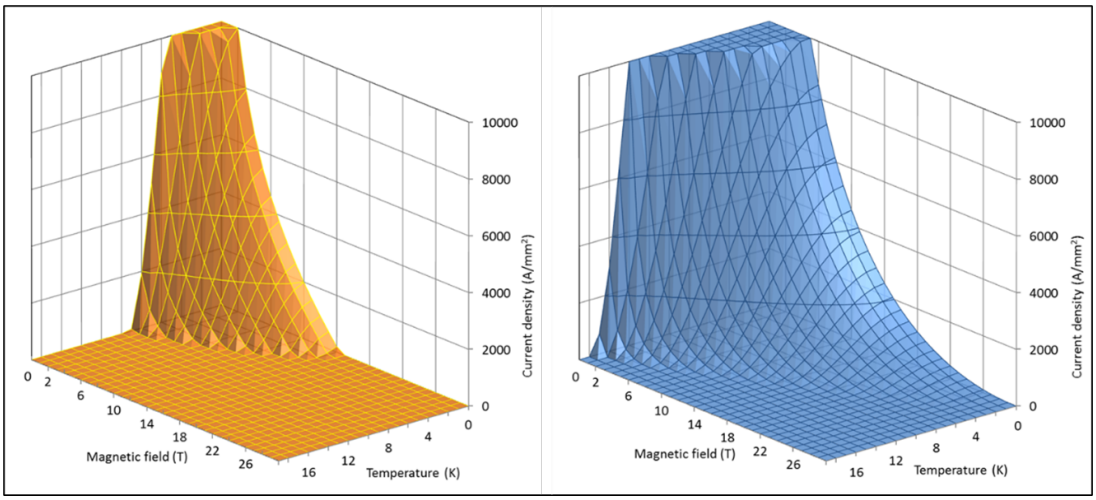

Fig. II.6.12: Critical surfaces for Nb-Ti and Nb_3Sn.

Nb-Ti is the most widely used superconductor, and it was used for the first time in particle accelerators in the insertion quadrupoles in the intersection storage ring (ISR) at CERN. The first application to dipoles, aiming at 1 TeV proton energy with a 4.4 T field in a 6.28 km ring was in the Tevatron accelerator, built at Fermilab in the early 80s. In High Energy Physics, it was used also for all the post-Tevatron superconducting accelerators (RHIC at BNL, HERA at DESY, and LHC at CERN). Other important applications are Magneting Resonance Imaging (MRI) or Nuclear Magnetica Resonance (NMR) magnets and fusion magnets (for example Tore Supra, France, that was marking the first application of superconductivity at 1.9 K). The cost of a high current density strand for accelerator magnets is 200 US $ per kg of wire (about 1 euro per m of strand).

II.6.3.3.2 Nb_3Sn

Nb and Sn can form an intermetallic compound from the A15 family (like Nb_3Al). T_c and B_{C2} depend on Sn content: the optimal is 20–25 % in weight. T_c is $\sim$ 18 K at 0 T and B_{C2} is $\sim$ 28 T at 0 K. The critical current density j_c depends on the micro-structure: high j_c is obtained with grains from 30 to 300 nm. One of the main differences with respect to Nb-Ti is that Nb_3Sn is brittle and therefore cannot be extruded. As a result, its formation must occur only at the end of the cable and/or coil fabrication process. In addition, it is strain sensitive, so its current carrying capability does not depend only on temperature and field, but also on the strain status.

Nb_3Sn is used for the magnets for medical Nuclear Magnetic Resonance Imaging (NMR or MRI), with field of about 20 T. In addition, it will be used in the coils for the International Thermonuclear Experimental Reactor (ITER) fusion project and in the interaction region quadrupole magnets for the High-Luminosity LHC. The cost of a high current density strand for accelerator magnets is approximately $\sim$1500 US $ per kg of wire (half of this for lower current density strand as used in ITER or NMR).

II.6.3.4 Practical superconductors

As explained in Section II.6.2, in particle colliders for high energy physics we want to maximize the collision energies, and this can be achieved by maximizing the field of the bending magnets. In the case of electro-magnets, in order to maximize the field it is needed to maximize the current in the winding. As a comparison, let's consider a round Cu wire with a diameter of 0.85 mm (see Fig. II.6.13, top left). In normal conducting magnets, which generally operate with fields up to 2 T, the typical value for the current density in a winding with active cooling is of about $5\ \mathrm{A}\ /\mathrm{mm}^2$, corresponding to a total of 3 A in a 0.85 mm strand. If we now look at a Nb-Ti or at a Nb_3Sn strand (see always Fig. II.6.13 top center and right), the current density can reach the 600–700 A/mm^2 level, with a total current of 300–400 A. This means a two order of magnitude increase with respect to the same dimension Cu strand, and at field that can reach a 8–9 T with Nb-Ti and 12–13 T for Nb_3Sn (HL-LHC case).

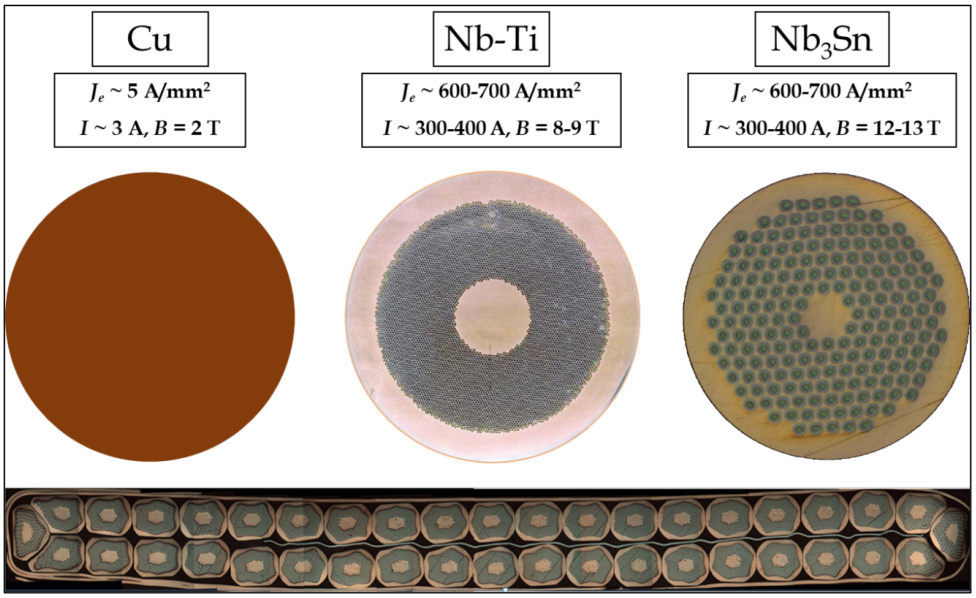

Fig. II.6.13: Example of a Cu wire (top left), Nb-Ti (top center) and Nb3Sn (top right), and of multifilamentary wires (or strands) Rutherford cable (bottom).

With these numbers one can appreciate why superconductivity is an enabling technology for a high energy physics particle collider. However, looking at the cross-sections in Fig. II.6.13, the level of complexity that characterizes superconducting wires can be appreciated.

In fact, rather than being composed by a solid bulk of superconducting material, like in the Cu case, practical superconductors used in accelerator magnets usually are characterized by *strands* with *filaments* of small diameters, *twisted* together, and embedded in a *copper matrix*. The strands are then combined in a *multi-wire* "Rutherford" *cable*, again *twisted* together, and surrounded by *electrical insulation* (see Fig. II.6.13, bottom).

In Section II.6.3.5 we will explain the reasons behind the dimensions and shape of the different elements constituting the building blocks of the practical superconductors for particle accelerators.

II.6.3.5 Multifilament wires or strands

II.6.3.5.1 Motivation of filament size: magnetization instabilities (flux jumps)

Let's consider the very simple geometry of an infinite slab of superconducting material of thickness 2d. Then, to simulate the behavior of a Type II superconductor, let's use the beam model or critical state model (CSM). Quoting C.P. Bean [12], "the basic premise of this model is that there exists a limiting macroscopic superconducting current density $j(H)$ that a hard superconductor can carry; and further, that any electromotive force, however small, will induce this full current to flow in an inhomogeneous mixed-state superconductor." In other words, the superconductor carries either a current density at j_c or no currents at all.

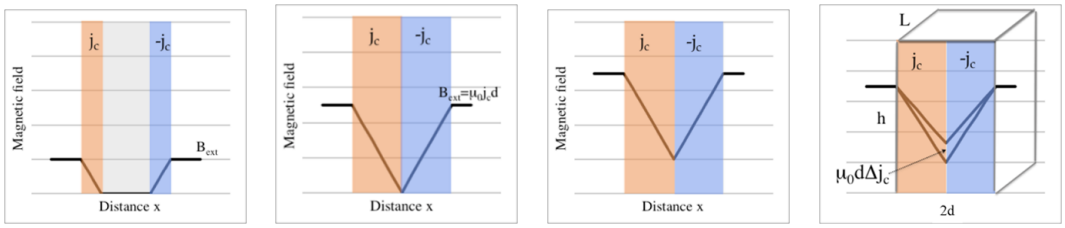

Fig. II.6.14: Critical state model and flux jump.

We now bring the external field to B_{ext} (see Fig. II.6.14 left). By raising the field to B_{ext}, we generate a j_c over a thickness Δx which will start flowing to shield the internal part of the slab, according to

$$B_{\text{ext}} = \mu_0 \, j_c \, \Delta x \quad . \tag{II.6.6}$$

Since the slab is superconducting, j_c is a persistent current density. If we now increase the field, the maximum field that can be shielded is the *penetration field* (see Fig. II.6.14, second panel from the left), given by

$$B_p = \mu_0 \, j_c \, d \quad . \tag{II.6.7}$$

A further increase of field beyond B_p, will not be shielded anymore by j_c hence an increase of field inside the superconductor (see Fig. II.6.14, third panel from the left). Now, let's imagine that from this status, we have a sudden thermal input which increases the temperature of the superconductor and therefore decreases its j_c. The field profile will change accordingly, due to the reduced capacity of the superconducting material of shielding the external magnetic field. According to the Maxwell equations, the change of the magnetic field induces a voltage, which, in the presence of a current I, generates a heat dissipation VI. Such dissipation, in turn, generates heat and a change of temperature ΔT_1. This induces a further reduction of critical current density $\ldots \Delta T_2 \ldots \Delta T_3$. If the sum $\sum T_k$ converges to a finite value we are stable, otherwise there is a mechanism providing a thermal runaway of the temperature. We can therefore define a stability criterion which establishes the minimum slab size that prevents the temperature from diverging. The criterion is

$$\frac{d}{2} < \frac{1}{j_c}\sqrt{\frac{3\,g\,C_p\,(T_c - T)}{\mu_0}} \quad , \tag{II.6.8}$$

where C_p is the specific heat, g is the density and $T_c - T$ is the difference between the operational temperature and the critical temperature.

One can conclude that the thinner isthe superconductor, the more stable is to magneto-thermal instability (also called flux-jumps). If larger than what established by the stability criterion, flux jumps can dissipate sufficient heat to cause an avalanche effect that transitions the superconductor to the normal conducting state (*quench*).

In addition, for a given size, one can see that also j_c plays a fundamental role: superconductors are less stable when j_c is larger. This is why superconducting magnets are more prone to this flux-jump instability in the early part of the current ramping (when currents and fields are lower, and thus j_c is higher) or when they use high-performance superconducting materials.

II.6.3.5.2 Motivation of filament size: superconductor magnetization and field errors

Let's keep using the critical state model, and let's now consider a superconducting filament immersed in a varying B_{ext}. Eddy currents develop in its periphery and will shield the inner part of the filament. In a round filament, these currents (again, according to the model, given by a current density equal to the j_c at that field and temperature), will have roughly an elliptical shape (like in Fig. II.6.15), they will not decay (since no resistance is present), and they are called persistent currents.

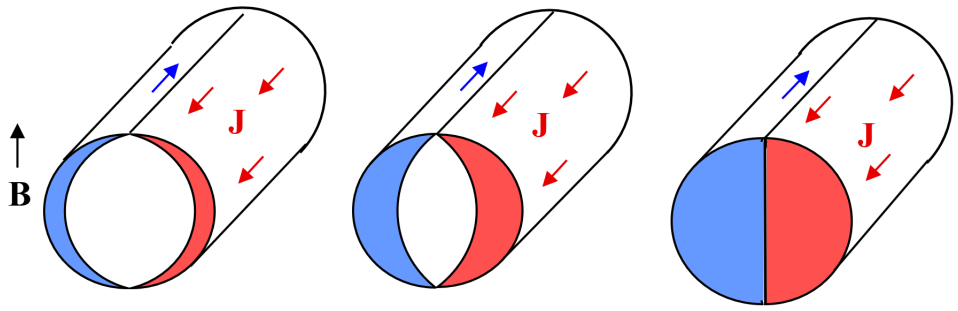

Fig. II.6.15: Persistent currents in a superconducting filament due to a varying external field (image from M. Wilson).

Because of these currents, the superconducting material exhibit a magnetisation, shown in Fig. II.6.16 (left), where the magnetic moment M_{f} of the superconducting filament is plotted as function of the external magnetic field. The magnetization of the superconductor causes perturbation of the magnetic field produced by the coil in the aperture, or field errors, plotted in Fig. II.6.16, right (these field errors, called harmonics, will be explained in Section II.6.4).

For a filament with diameter d_{f} , when fully penetrated by the magnetic field (see Fig. II.6.15, right), the magnetic moment per unit volume [J/T/m^3] is given by

$$M_{\text{f}} = \frac{2}{3\pi}\,j_c\,d_{\text{f}} \quad . \tag{II.6.9}$$

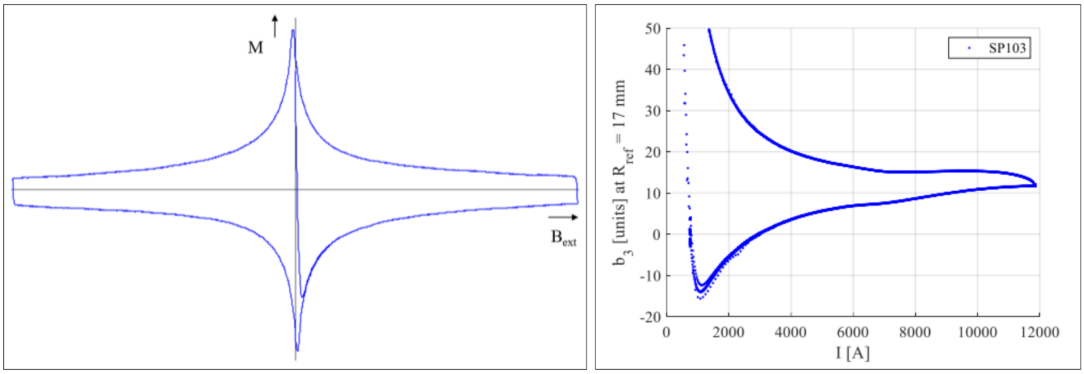

Fig. II.6.16: Left: magnetisation of a superconductor due to a varying external field (image from M. Wilson). Right: field error (allowed harmonic b_3) as a function of the current (image from S. Izquierdo Bermudez [8]).

Again, in a way similar to the flux jump instability, thinner filaments and smaller critical current densities produce less field errors (especially in the early part of the ramp).

II.6.3.5.3 Motivation of filament size: superconductor magnetization and AC losses within the filaments

In the presence of a magnetic moment per unit volume ([J/T/m^3]) and of a varying external magnetic field from B_1 to B_2, the superconducting material experiences a loss per unit volume (J/m^3) given by

$$Q = \int_{B_1}^{B_2} M \, dB \quad . \tag{II.6.10}$$

For example, as stated in Ref. [8], for the HL-LHC Nb_3Sn magnets charged to full field the loss is of the order of 1 MJ/m^3. The total energy loss by a superconductor ramped up and down, like in Fig. II.6.16 (left) is proportional to the area within the magnetization curve. The AC power loss per unit volume of filament (W/m^3) with a varying magnetic field for a fully magnetically penetrated filament, can be written as

$$P_\mathrm{f} = M_\mathrm{f} \dot{B} = \dot{B} \frac{2}{3\pi} j_c \, d_\mathrm{f} \quad . \tag{II.6.11}$$

If we want instead to write the magnetization and the AC power loss due to filament magnetization per unit volume (W/m^3) of winding, we have

$$\begin{cases} M_\mathrm{fw} &= \lambda_\mathrm{fw} \frac{2}{3\pi} j_c \, d_\mathrm{f} \\ P_\mathrm{fw} &= M_\mathrm{fw} \dot{B} = \lambda_\mathrm{fw} \dot{B} \frac{2}{3\pi} j_c \, d_\mathrm{f} \end{cases} , \tag{II.6.12}$$

where λ_fw is the fraction of superconductor over the entire coil cross-section.

In other words, a superconductor, due to its magnetization, not only produces field imperfections but also heat dissipation. Any source of heat has to be controlled and minimized, in order to reduce the possible increase of temperature beyond the critical temperature. Again, smaller filaments contribute to

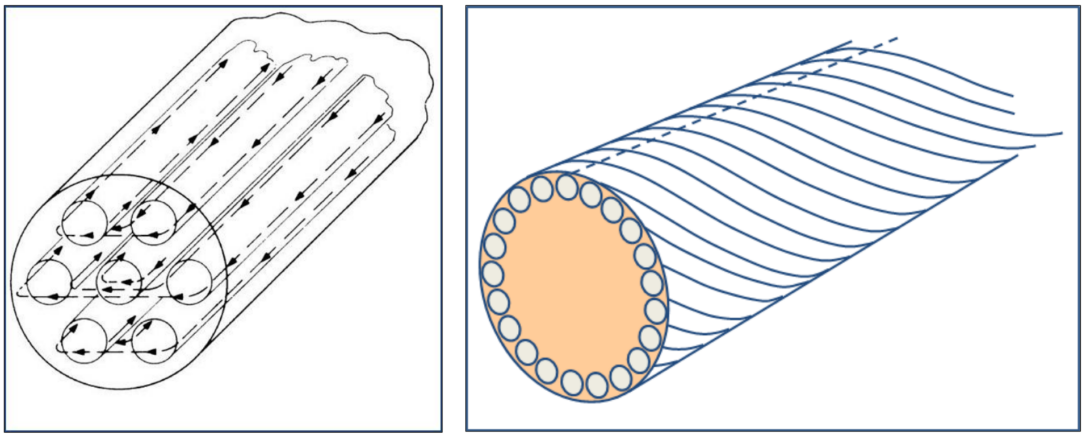

Fig. II.6.17: Left: Eddy currents in strands between straight filaments (courtesy of M. Wilson), and twisted filaments (courtesy of L. Bottura).

reduce such power dissipation. This dissipation depends on the difference between the magnetic field in the two states. To provide some general order of magnitude of filaments, considering accelerator magnets, and considering the push to minimal flux jump instabilities, persistent current effects, and AC losses (at the filament level), we can mention that the Nb-Ti filaments in the LHC main magnets have a diameter of 6–7 µm. For fast ramping Nb-Ti magnets like the ones used in the SIS-300 accelerator, filaments of 3 µm were used. The Nb_3Sn magnet for the HL-LHC project used superconductors with filament of about 50 µm.

II.6.3.5.4 Motivation of filament twist: AC losses between filaments

When a multi-filament wire is subjected to a time varying magnetic field, current loops are generated between filaments. The loops are superconductive for most of the perimeter, plus a resistance between the adjacent filaments. This is a purely classical effect (Maxwell equations), not related to superconductivity. If filaments were straight (see Fig. II.6.17, left), large loops would arise with large currents and consequently large AC losses. We can express the power loss per unit volume (W/m^3) of strands (P_s) and of winding (P_{sw}) due to strands AC losses between filaments as given by the magnetic moment associated to the inter-filament currents:

$$\begin{cases} P_s \;=\; M_s\,\dot{B} \;=\; \dot{B}^2 \frac{1}{\rho_m} \left[\frac{p_w}{2\pi}\right]^2 \\ P_{sw} \;=\; \lambda_{sw}\, M_s\,\dot{B} \;=\; \lambda_{sw}\,\dot{B}^2 \frac{1}{\rho_m} \left[\frac{p_w}{2\pi}\right]^2 \end{cases} , \tag{II.6.13}$$

where p_w is the strand twist pitch, ρ_m is the resistivity of the strand matrix and λ_{sw} is the fraction of strand over the entire coil cross-section. Therefore, filaments are twisted to reduce the AC loss power. Also, the twist prevents the bundle of filaments to behave as a large monofilament, thus reducing the risk of flux-jump instabilities. The twist pitch is usually of 20–30 times the wire diameter.

II.6.3.5.5 Motivation of strand diameter: magneto-thermal instabilities (self-field instability)

Let's now move from the filament level to the strand level, and let's imagine to ramp the transport current in a full strand. When the transport current is increased, it will tend to flow only in the outermost filaments (see Fig. II.6.18, left), with a current density which is the critical current density j_c (again, according to the CSM). In the same way as explained previously with the flux jump instabilities, a thermal input may increase the temperature of the strand and reduce the j_c . This will cause a redistribution of the current in the strand, with a consequent variation of the flux inside it. As a result, a voltage will appear which, in the presence of a current I, will produce a dissipation VI. And so on. This phenomenon is called self-field instability [13, 14].

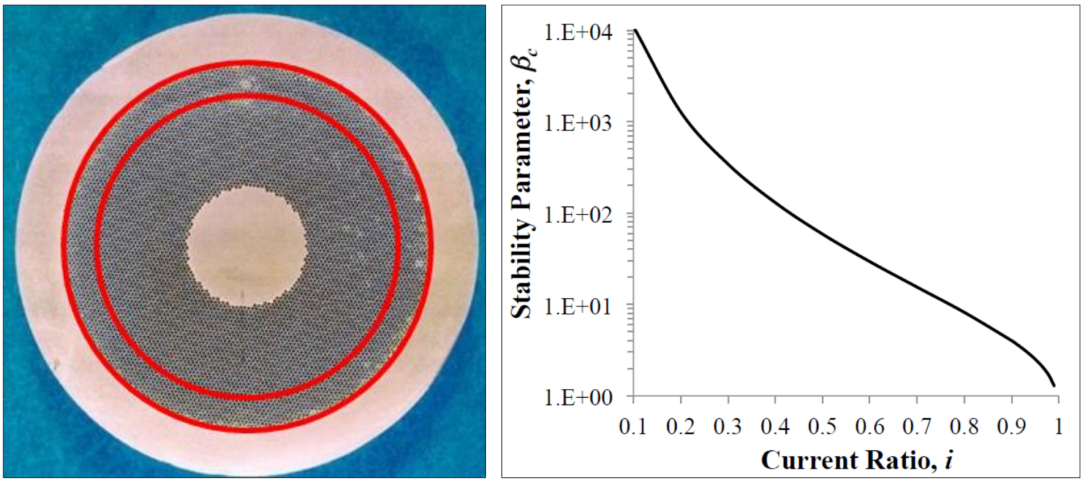

Fig. II.6.18: Left: when the transport current is ramped, it flows in the outermost filaments. Right: stability parameters for self field instability, where $i = \frac{I}{I_c} = 1 - \epsilon^2$.

A simplified stability criterion can be written as

$$\beta = \mu_0 \lambda^2 \left| \frac{dj_c}{dT} \right| \frac{r^2}{V} j_c \leq \beta_c = \left(-\frac{1}{2} \ln(\epsilon) - \frac{3}{8} + \frac{\epsilon^2}{2} - \frac{\epsilon^4}{8} \right)^{-1} \quad , \tag{II.6.14}$$

where λ is the superconductor fraction, V volumetric specific heat of the strand, r strand radius, and ϵ is given by $\frac{I}{I_c} = 1 - \epsilon^2$. The stability parameter is plotted in (see Fig. II.6.18, right). As can be seen by the previous equation, such an instability can occur in particular with large strands. Therefore, the strand size for accelerator magnets is usually chosen within 0.5 and 1.1 mm diameter. In particular 0.48 mm diameter Nb-Ti strands are used in LHC matching sections MQM and MQY magnets, and in HL-LHC nested correctors MCBXF (CIEMAT, Spain). The LHC Nb-Ti strands for the main dipoles have 0.825 and 1.065 mm diameter. Considering Nb_3Sn strands, we have 0.7 mm diameter for the LHC Accelerator Research Project (LARP) Technological Quadrupole (TQ) and the HL-LHC 11 T. Lawrence Berkeley National Laboratory (LBNL) HD2 and the LARP HQ have 0.8 mm diameter, the HL-LHC quadrupole magnet MQXF have 0.85 mm diameter and for the CERN Facility for REception of Superconducting CAbles 2 (FRESCA2) 1.0 mm.

The effect of the magneto-thermal instabilities is very effectively summarized in the plot of

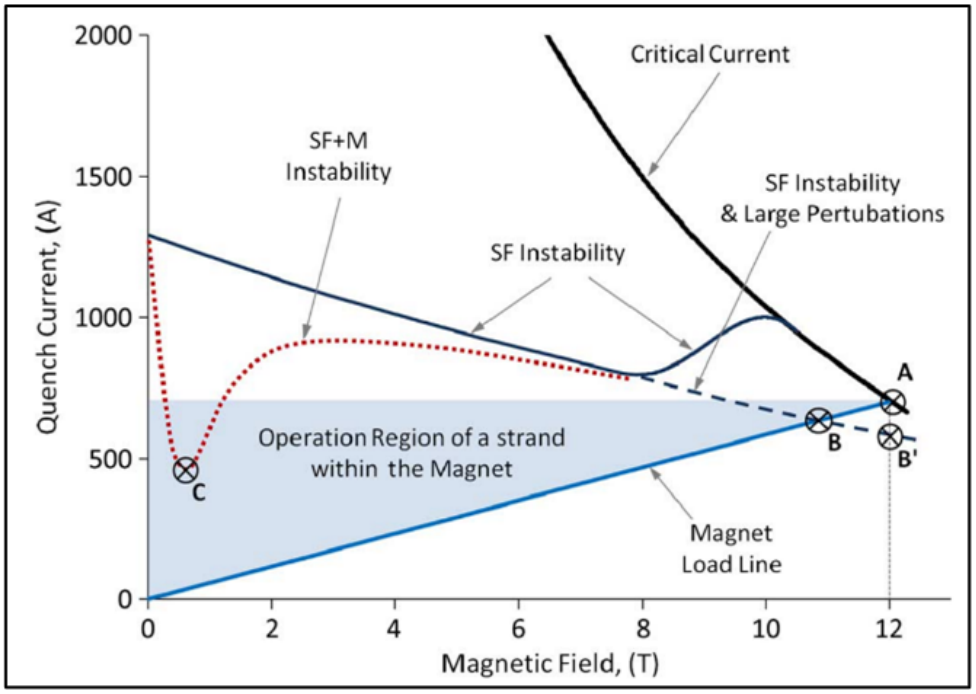

Fig. II.6.19: As reported in Ref. [13], "Sketch representing qualitatively the causes of premature quenches in superconducting magnets affected by magneto-thermal instabilities. In the plot it is reported the current in a strand of the magnet. The acronyms SF and M stand for Self-Field and Magnetization respectively".

Fig. II.6.19 from Bordini, *et al.* [13], where one can see the effect of both magnetization instabilities or flux-jumps (M) and of self-field instabilities (SF). The combined effect can in practice significantly depress the workable area below the critical current in superconducting magnets.

II.6.3.5.6 Motivation of Cu matrix

Superconductors have a very high resistivity in their normal state. It can be shown that a filament of Nb-Ti, if quenched in free space, can reach very high temperatures in few ms. If the filament is embedded in a copper matrix, when a superconducting-to-normal state transition occurs, the current can redistribute in the low-resistivity matrix and the peak temperature can be maintained below 300 K (see Fig. II.6.20).

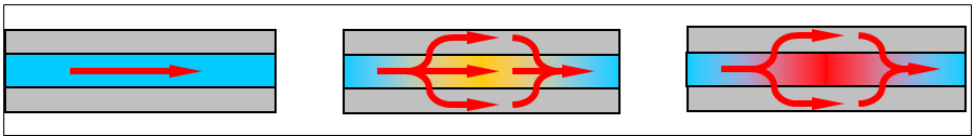

Fig. II.6.20: Role of the stabilizer (gray) on a quenching superconductor (in blue), (image by L. Bottura).

The copper matrix facilitates quench protection: it allows the quench to propagate and it provides time to act on the power circuit. In the case of a small volume of superconductor heated beyond the critical temperature (for instance because of a flux jump), the current can flow in the copper for a short moment, allowing the filament to cool-down and recover superconductivity. The matrix also helps stabi-

lizing the conductor against flux jumps (dynamic stability), since the increase of temperature for a given external thermal input is reduced.

To summarize, the Cu matrix is essential for the stability of the superconductor, i.e. the capability of handling heat input without transitioning to the normal state, and for the protection after a quench. Both these two important aspects of superconducting magnet technology will be discussed in Section II.6.6.

To define the quantity of Cu matrix in a strand one defines a Cu to non-Cu (Cu/non-Cu) ratio. A Cu/non-Cu ratio of x means that in the strand cross-section one has a quantity 1 of superconductor and a quantity x of Cu. For example a Cu/non-Cu = 2 means $\frac{1}{(1+2)} = 33\%$ of superconductor and $\frac{2}{(1+2)} = 67\%$ of Cu. In accelerator magnets, usually Cu/non-Cu ratio ranges between 1 and 2. For example, in corrector magnets, where usually the efficient use of the superconductor is not a priority, we can have very high ratios (above 2). For the main magnets in the arc, where the current in the strand has to be maximized in order to reach the highest field with the smallest coil, one needs to choose the minimum amount of Cu that is required to stabilize and protect the magnet: the LHC dipoles have 1.65 (inner layer) and 1.95 (outer layer) ratios. For the HL-LHC magnets we have 1.1 (11 T) and 1.2 (MQXF). Lower values were used in short magnets, like 0.89 for LARP TQ. An extremely low value of 0.4 was used (successfully) in D20, a short model magnet but seems not viable for long magnets. The quality of the Cu is then defined with the Cu Residual Resistivity Ratio (RRR), i.e. the ratio of Cu resistivity at 293 K to the resistivity at 4.2 K. The RRR of copper is an important parameter for stability, and is usually set to be larger than 150 in wires and larger than 100 in cables.

II.6.3.5.7 Fabrication of Nb-Ti multifilament wires

The process of fabricating a Nb-Ti strand involves several steps, shown in Fig. II.6.21. The starting elements are Nb-Ti ingots (top left) of about 200 mm diameter and about 750 mm length, which are inserted in Cu tubes and extruded and drawn. Then, several rods are stacked and extruded again, until filament of the micron level are achieved and single-piece strands are fabricated, at the km level in length.

It is important point out that prior to the fabrication described in the figure, all the key geometrical parameters of the wire have to be defined, in particular

- The *copper to superconductor ratio*, to ensure enough stability and quench protection without compromising the maximum current the wire can carry;
- The *filament diameter*, to minimize flux jumps, persistent currents, AC losses, and, at the same time, the overall fabrication costs;
- The *inter-filament spacing*, which has to be small so that the filaments, harder than Cu, support each other during drawing operation, but at the same time large enough to prevent filament couplings;
- the *Cu core and sheath*, to reduce cable degradation;
- The *piece length* which has to be long enough to wind continuously very long coils (LHC required piece length longer than 1 km).

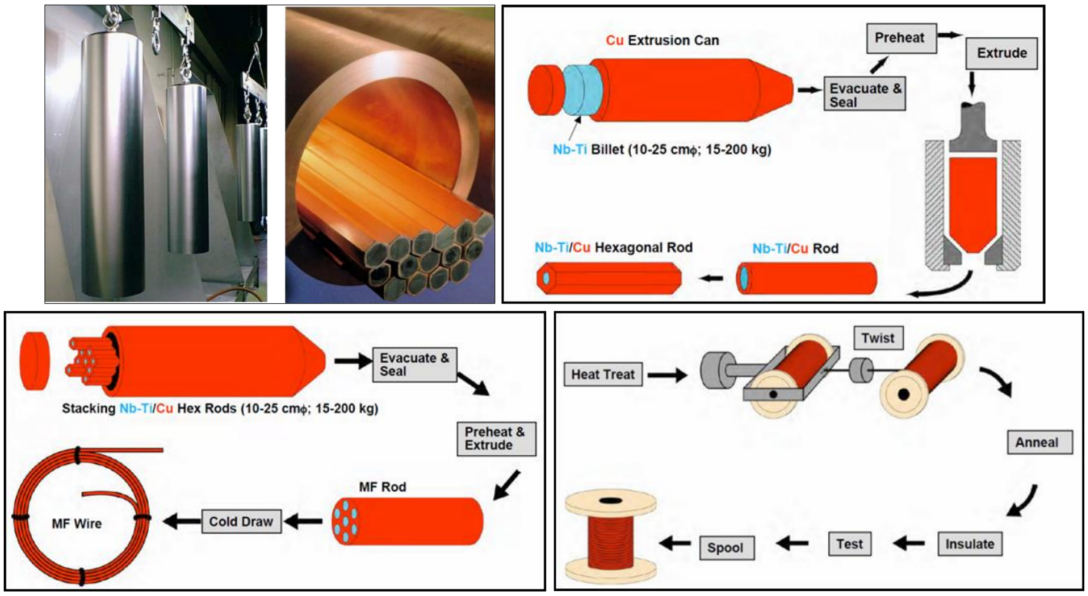

Fig. II.6.21: Fabrication process of multi-filament strands.

II.6.3.5.8 Fabrication of Nb_3Sn multifilament wires

The fabrication of Nb_3Sn is fundamentally identical to the one of Nb-Ti, except for an important difference: since Nb_3Sn, once formed, is brittle, and cannot be extruded, the process of extrusion has to be made with Sn and Nb still in a separate form. This can be seen in the internal-tin and the powder-in-tube designs shown in Fig. II.6.22 (top).

In the first case, sub-elements have a tin core surrounded by niobium rods embedded in Cu (Rod Restack Process, RRP). Each sub-element has a diffusion barrier. In the second case, a tin rich powder is inserted in a niobium tube. During heat treatment (see Fig. II.6.22 bottom), the tin diffuses in the niobium forming Nb_3Sn (light grey area in the picture). The un-reacted external part of the niobium tube (darker gray area) is the barrier, necessary to avoid that the tin reaches and contaminate the Cu (thus reducing the RRR). A detailed description of the fabrication of Nb_3Sn coils will be given in Section II.6.5.

II.6.3.6 Practical superconductors: multi-strand cables

Superconducting coils for particle accelerators are usually wound from multi-strand cables, i.e. cables composed by a certain number of strands (ranging from about 6 to about 50), twisted together. The most commonly used multi-strand cables is the Rutherford cable (see Fig. II.6.23).

II.6.3.6.1 Motivation of multi-wires

The key advantages of a multi-strand cable are:

- The use of cable contributes to reduce the strand piece length;
  - A long coil wound with a cable with N strands would require a strand piece length which would be 1/N time the piece length required to wind the same coil with a single strand,

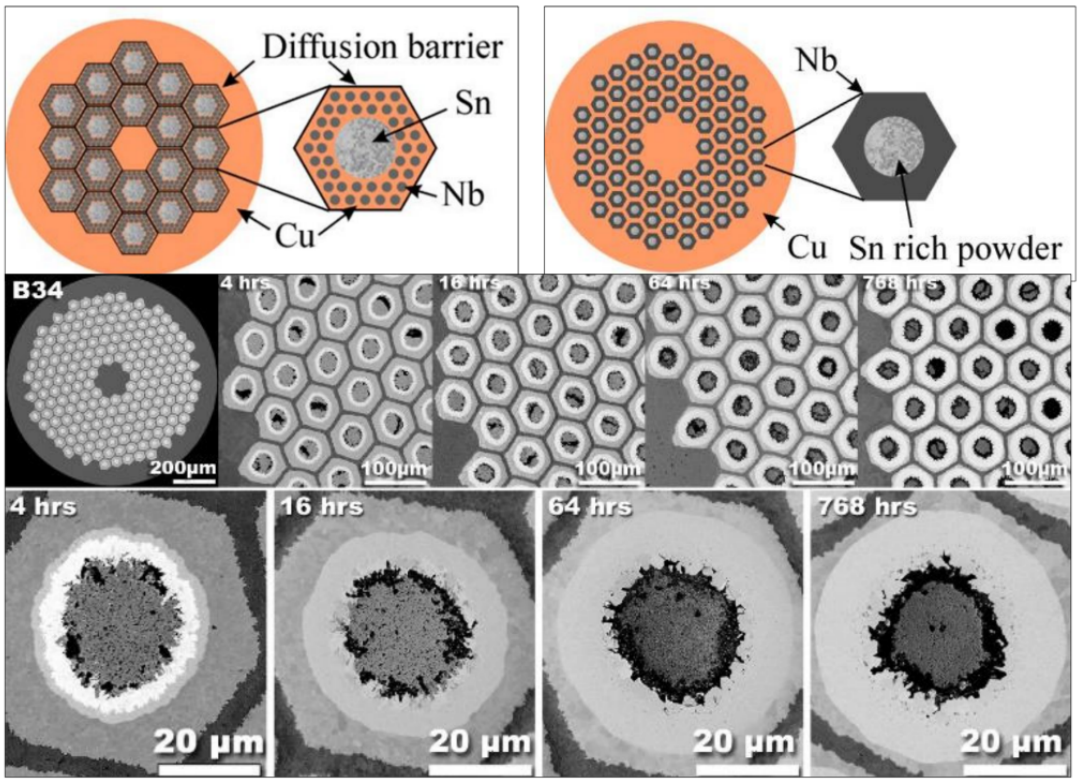

Fig. II.6.22: Top: (left) example of internal tin and *Powder In Tube* (PIT), (right) Nb_3Sn strands. Bottom: diffusion of tin in niobium during the heat treatment of a PIT wire.

- A coil wound with a large cable has less turns than a coil wound with a single strand. This has two main advantages:
  - The coil winding process is simplified,
  - The coil inductance is reduced, which results in less voltage required for power supply during ramp-up and after a quench, faster current discharge and less coil voltage.
- Finally, with a multi-strand cable it is possible to have current redistribution in case of a defect or a quench in one strand.

II.6.3.6.2 Motivation of twisted wires

Similarly to what was explained in the sub-sections about the filaments, if the strands were straight along a cable, large current loops would take place in the presence of a varying field, with both a large impact on the field quality and large AC losses.

We can treat the issue in the same way as we did for the filament, i.e. by defining a cable magnetization and computing then the AC losses. Fig. II.6.24 shows the geometry and parameters of a cable with N strands, with thickness 2b and width 2c. We define the resistance between cross-over strands as R_c and a resistance between adjacent strands as R_a. We then consider three different scenarios (see Fig. II.6.25).

Fig. II.6.23: Images of a multi-strand Rutherford cable.

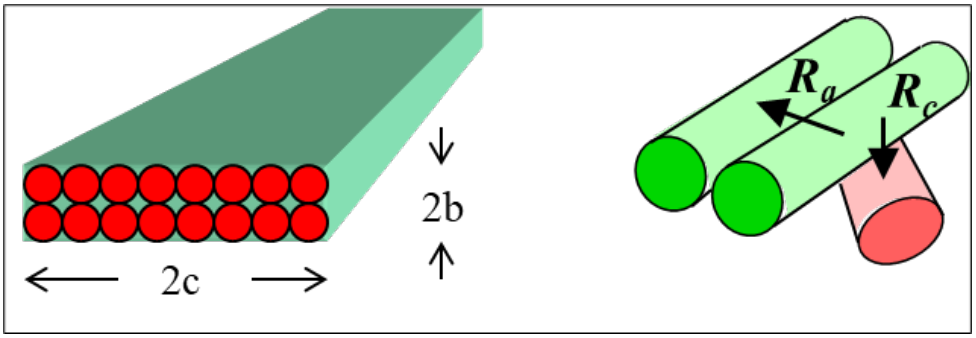

Fig. II.6.24: Left: cable geometry and parameters. Right: cross-over and adjacent resistance.

For each of these three scenarios we can define a magnetic moment per unit volume of cable [J/T/m^3] given by, respectively

$$\begin{cases} M_{tc} &= \frac{1}{120}\,\frac{\dot{B}_t}{R_c}\,\frac{c}{b}\,p\,N\,(N-1) \\ M_{ta} &= \frac{1}{6}\,\frac{\dot{B}_t}{R_a}\,\frac{c}{b}\,p \\ M_{pa} &= \frac{1}{8}\,\frac{\dot{B}_p}{R_a}\,\frac{b}{c}\,p \end{cases} , \tag{II.6.15}$$

where B_t and B_p are the perpendicular (transverse) and parallel field to the broad face of the cable, and p is the pitch length (Fig. II.6.25).

Again, we can express the power loss due to cable AC losses per unit volume (W/m^3) of the whole winding as

$$\begin{cases} P_{tcw} &= \lambda_{cw}\,M_{tc}\,\dot{B}_t \\ P_{taw} &= \lambda_{cw}\,M_{ta}\,\dot{B}_t \\ P_{paw} &= \lambda_{cw}\,M_{pa}\,\dot{B}_p \end{cases} , \tag{II.6.16}$$

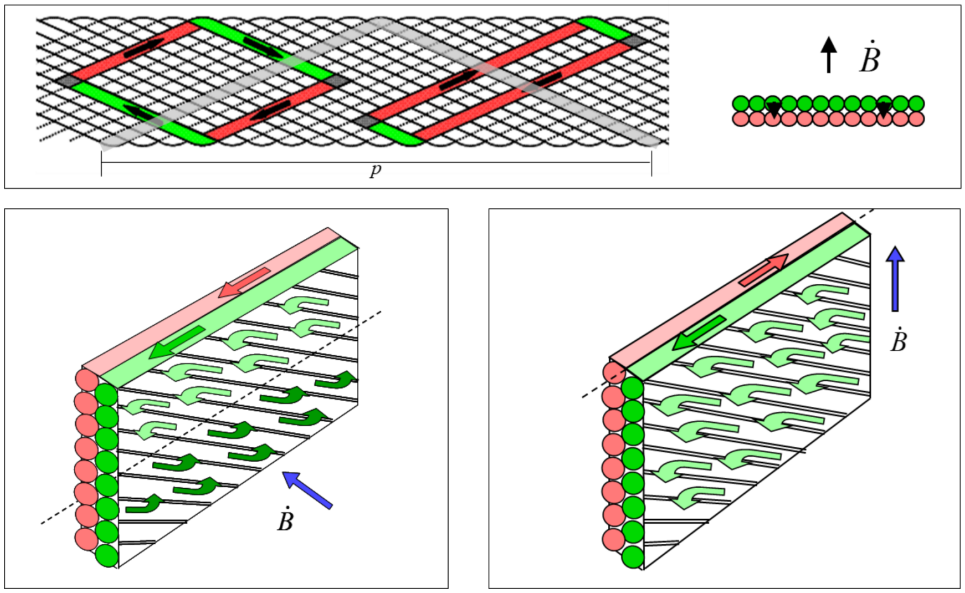

Fig. II.6.25: Top: eddy currents produced by a $\dot{B}$ perpendicular to the wide surface of the cable via crossover resistance R_c; the pitch p is also indicated. Bottom left: eddy currents produced by a $\dot{B}$ perpendicular to the wide surface of the cable via adjacent resistance R_a. Bottom right: eddy currents produced by a $\dot{B}$ parallel to the wide surface of the cable via adjacent resistance R_a.

where λ_{cw} is the fraction of cable over the entire coil cross-section. Therefore, one can conclude that the shorter is the pitch obtained by twisting the cable, the smaller is the magnetization and the AC losses due to the eddy currents developing between strands when the cable is immersed in a varying external field.

We can finally go again over the different three types of magnetization and AC losses in a superconducting cable, as shown in the Fig. II.6.26 (left) by M. Wilson (the size of the loop is arbitrary):

- the losses in the filaments, minimized by reducing the diameter of the filaments;
- the ones between the filaments, minimized by twisting the filaments;
- the one between the strands, minimized by twisting the strands.

All three need to be minimized so that during the ramps of current to bring the accelerator to the nominal collision energy (see typical current cycles in the LHC still in Fig. II.6.26 right) both the field errors and the power losses are minimal.

II.6.3.6.3 Fabrication of Rutherford cables

Rutherford cables are fabricated with a cabling machine (see Fig. II.6.27). Each strand is initially wound on individual spools, which are then mounted on a rotating drum. While the drum is rotating, strands are pulled into assembly rolls (called Turk's head, se Fig. II.6.28 left). The rolls compact the cable, by plastically deforming the strands, and provide the final cable shape. At the time of the submission of this chapter, the cabling machine available at CERN is limited to 40 strands, the one at FNAL can reach 42 strands, and the one at LBNL 60 strands.

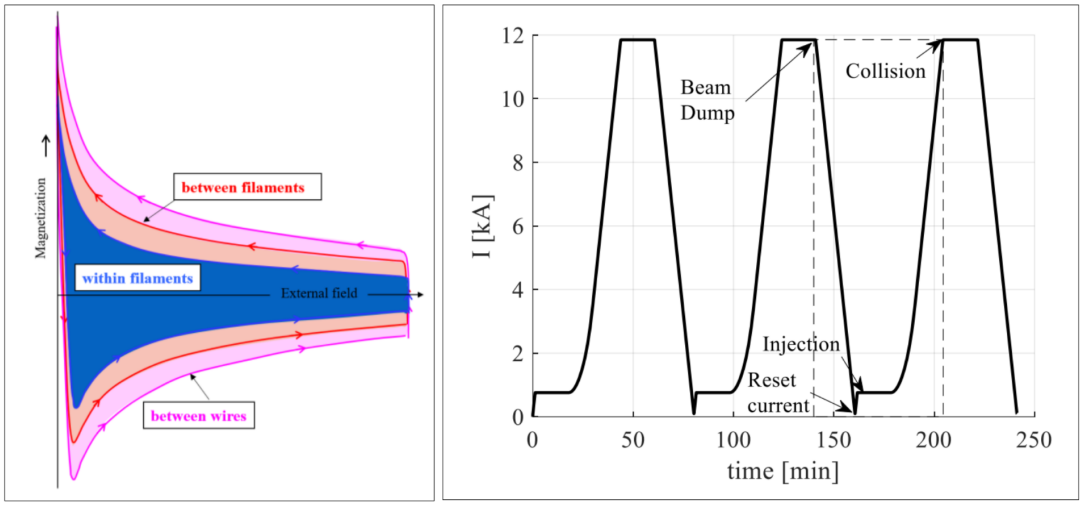

Fig. II.6.26: Left: schematic plot by M. Wilson of the different magnetization curves in a superconducting cable (the amplitude of the loop is arbitrary). Right: typical current vs time cycle for a main bending dipole in the LHC (image from S. Izquierdo Bermudez [8]).

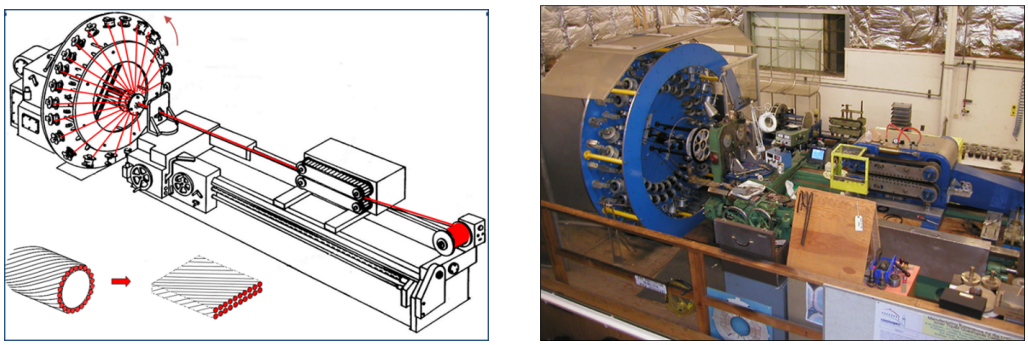

Fig. II.6.27: A Rutherford cabling machine.

The positions and orientation of the rolls determine the shape of the cable and the compaction. The shape can be rectangular or trapezoidal. The rectangular shape is usually used in block-type coils, which have a rectangular cross-section given by the stacking of rectangular Rutherford cable. Trapezoidal (or keystone) shape cables are instead used in so-called $\cos\theta$ coils, characterized by a roman-arc type of cross-section, which can be achieved by stacking keystone cables. When a cable has a trapezoidal shape, the defining parameter is the keystone angle φ_{cable} given by

$$\tan\varphi_{\text{cable}} = \frac{t_{\text{thick cable}} - t_{\text{thin cable}}}{w_{\text{cable}}} \quad , \tag{II.6.17}$$

where $t_{\text{thick cable}}$, $t_{\text{thin cable}}$, w_{cable}, are the thickness of the thick edge, the thickness of the thin edge and the width of the cable. Typical keystone angles range between 0.5° and 1.25°.

The cable compaction, also imposed by the Turk‘s heads, is defined by the ratio of the sum of the cross-sectional area of the strands (direction parallel to the cable axis) to the cross-sectional area of the cable, i.e. p_{cable}

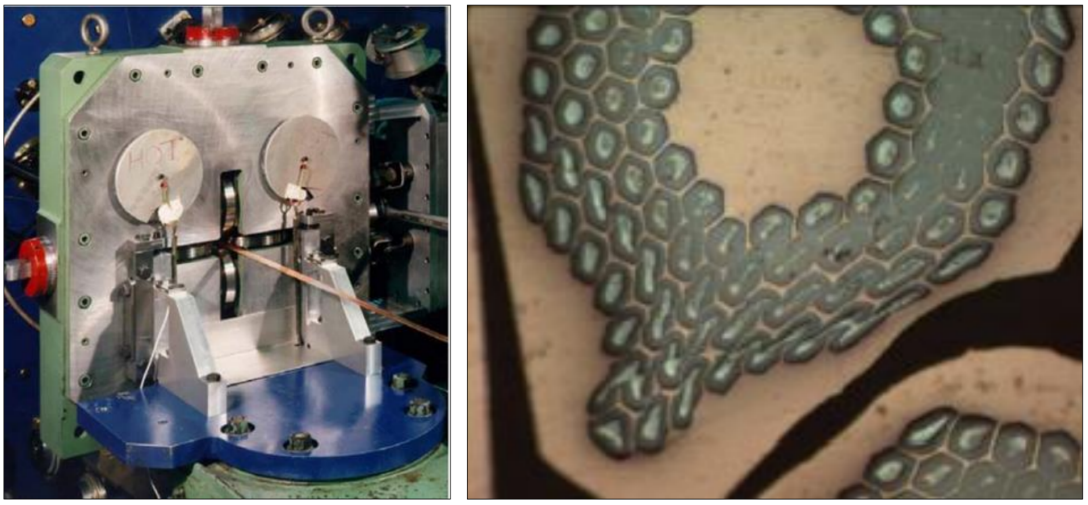

Fig. II.6.28: Turk's heads, left, and example of deformed Nb_3Sn filaments after cabling manufacturing.

$$k_{\text{cable}} = \frac{N_{\text{strand}}\,\pi\,d_{\text{strand}}^2}{4\,w_{\text{cable}}\,t_{\text{cable}}\cos\psi_{\text{cable}}} \quad , \tag{II.6.18}$$

where N_{strand} is the number of strands, d_{strand} is the strand diameter, t_{cable} is the cable mid-thickness, w_{cable} is the cable width, p_{cable} is the pitch length and ψ_{cable} is the pitch angle given by $\tan\psi_{\text{cable}} = \frac{2\,w_{\text{cable}}}{p_{\text{cable}}}$ (p_{cable} the pitch length). The cable compaction is chosen (or better, maximized) to provide good mechanical stability during winding, and to maximize the current vs cross-sectional area that the cable can carry. As a side effect, the risk of over compacting the cable is to cause cable degradation. Cable degradation is the reduction of critical current density of a strand after cabling with respect to the virgin strand (before cabling). In fact, an excessive edge deformation may cause a reduction of the filament cross-sectional area (Nb-Ti) or a breakage of the reaction barrier with incomplete tin reaction (Nb_3Sn), as shown in Fig. II.6.28, right. In both cases, the result is an underperforming strand compared to its status before cable manufacturing. In order to avoid degradation after manufacturing, strands are measured and their cross-sectional images analyzed. Typical cable compaction are around 90% for Nb-Ti (88% in a Tevatron dipole magnets and 92.3% for an HERA dipole magnet). A lower value is usually chosen for Nb_3Sn, to minimize the number of filaments with broken barriers and/or merged filaments.

II.6.3.7 Cable insulation

The general purpose of the cable electrical insulation is to prevent that during ramping of the magnet large eddy currents develop between the turns, with resulting AC losses and impact on the magnetic field quality. In other words, the cable insulation keeps the cables electrically separated during ramps (up and down). The electrical insulation has also to withstand the large voltages that usually develop after a quench, when rapid current discharge is required to protect the magnet (see Section II.6.6). Therefore, the properties of the electrical insulation must be

- Good electrical properties to withstand turn-to-turn voltage after a quench;
- Good mechanical properties to withstand high pressure conditions;

– Porosity to allow penetration of helium (or epoxy);
– Radiation hardness.

In Nb-Ti magnets, cables are usually surrounded by overlapping polyimide tapes (see Fig. II.6.29 left), whilst in Nb_3Sn magnets cables are insulated by fiber-glass (which can withstand the high temperature of the heat treatment), either or in the form of tapes or sleeves, or directly braided on the cable (see Fig. II.6.29 center and right). Typically, the insulation thickness ranges between 100 and 200 µm.

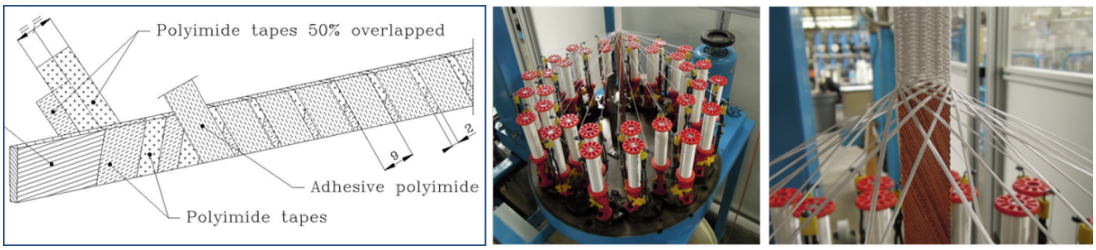

Fig. II.6.29: Nb-Ti cable insulation with polyimide layers (left) and Nb_3Sn cable insulation with braided fiberglass (center and right).

II.6.3.7.1 Filling factor and different current densities

We would like to conclude the section dedicated to the practical superconducting material showing a cross-section of a Nb_3Sn superconducting coil, where filaments, strands and cable can be seen in Fig. II.6.30. It is important to point out how only a small fraction of the total area is occupied by the current carrying elements (the superconductor filaments), whilst a significant fraction of the total cross-section is used by the stabilizer (copper in this case), voids between strands, and cable insulation.

Fig. II.6.30: Cross-section of a superconducting coil.

We can define the parameter k_{cable}, the *filling factor* , to indicate how much area in a coil is covered by current carrying material :

$$k_{\text{cable}} = \frac{N_{\text{strand}}\, A_{\text{superconductor strand}}}{A_{\text{insulated cable}}} \quad . \tag{II.6.19}$$

The filling factor value usually ranges between 0.25 to 0.35, which means that only about 30 % of the total coil cross-section is used by the superconductor material, where the current flows.

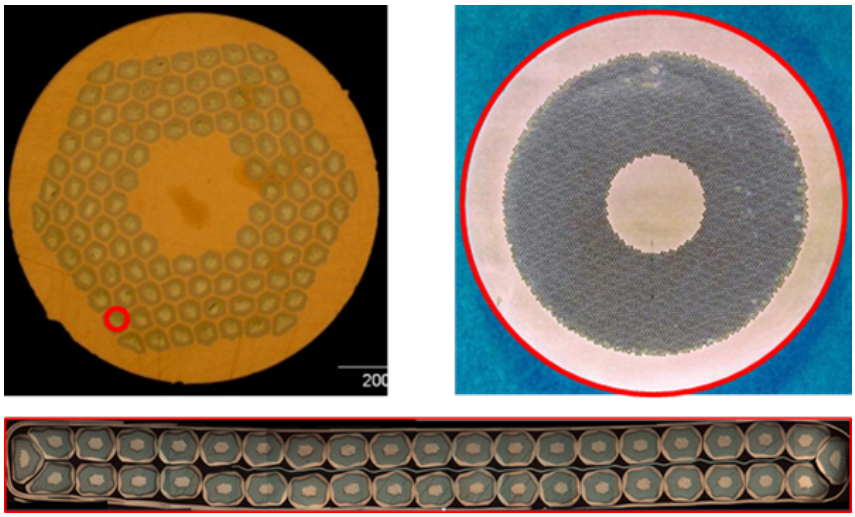

Fig. II.6.31: Different current densities: in the superconducting filament j_{sc}, in the strand j_{e}, and in the insulated cable j_{o}.

Another important parameter is related to the different current densities which may be considered. So far, we mentioned the most important one, the current density in the superconductor j_{sc}, given by

$$j_{\mathrm{sc}} = \frac{I_{\mathrm{strand}}}{A_{\mathrm{superconductor\,strand}}} \quad , \tag{II.6.20}$$

which is the current density of the filament, shown in Fig. II.6.31 top left.

To compare strand performance, it is useful to define also the current density over the overall strand area, named *engineering current density* j_{e} (see Fig. II.6.31 top right), given by:

$$j_{\mathrm{e}} = \frac{I_{\mathrm{strand}}}{A_{\mathrm{strand}}} \quad . \tag{II.6.21}$$

The j_{e} depends not only on how much current flows in the superconductor, but also on the amount of copper in the strand (Cu/non-Cu ratio). Finally, in order to include all the elements in the coil cross-section, we define the current density over the overall coil area, called *overall current density* j_{o} (see Fig. II.6.31), given by

$$j_{\mathrm{o}} = \frac{I_{\mathrm{cable}}}{A_{\mathrm{insulated\,cable}}} \quad , \tag{II.6.22}$$

the ratio between j_{sc} and j_{o} is the filling factor k_{cable}.

II.6.4 Magnetic design

The superconducting strands and cables described in the previous Section represents the first building block of the design of a superconducting magnet. In this section we will address the magnetic design

which deal with how the superconductor has to be placed around the aperture in order to produce the required magnetic field. The magnetic design of a superconducting magnet begins with the definition of the magnetic requirements, i.e. the set of the magnetic field parameters or characteristics, defined by the accelerator physicists, that the superconducting magnet needs to meet for a given accelerators, specifically

- The field shape: dipole, quadrupole, sextupole. . . ;
- The field magnitude: usually, for low T superconductors, from 2 to 16 T;
- The field quality or homogeneity: defined by the multipoles or harmonics;
- The field volume, given by the coil aperture and the length: typically, some centimeters for the first and some meters for the second at LHC.

In this section we will address the magnetic design by trying to answer the following questions:

- How do we create a perfect magnetic field and a field with a perfect configuration?
- Since the field that we can produce will not be perfect, how do we express the field and its "imperfections"?
- How do we design a coil to minimize these imperfections (field errors)?
- Which is the maximum field we can get?

We will then conclude with an overview of different magnet designs.

II.6.4.1 How do we create a perfect field?

Let's consider a circle carrying a current density $+j_o$ perpendicular to its surface (see Fig. II.6.32 left), where the positive current is directed towards the reader.

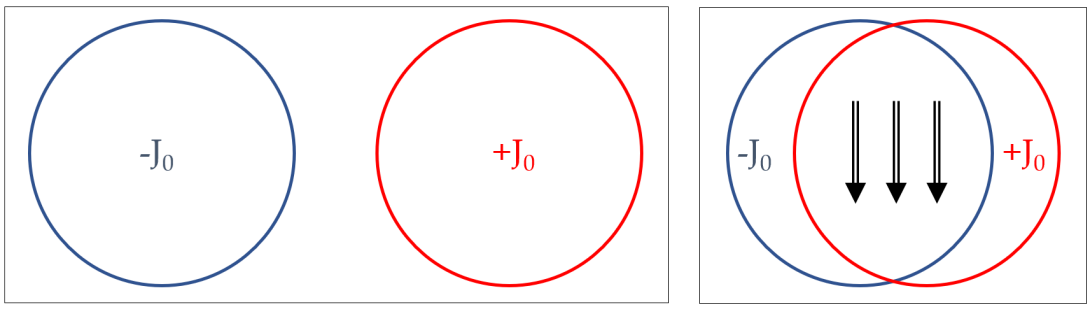

Fig. II.6.32: Intersecting circles.

The magnetic field inside the circle is perpendicular to its radius and proportional to the distance of the center (r)

$$B = -\frac{\mu_0 j_0 r}{2} \quad . \tag{II.6.23}$$

Let's now consider a second circle with a current density equal to $-j_o$, and allow the two circles to overlap partially , as shown in Fig. II.6.32 (right). As demonstrated by Wilson [3], the field inside the overlapping area (or inside the interception of the two circles) is

$$\begin{cases} B_x &= 0 \\ B_y &= -\frac{\mu_0 j_0}{2} s \end{cases} , \tag{II.6.24}$$

with s the distance on the x axis between the center of the two circles. Therefore, a uniform current density in two **intersecting circles** produces a pure dipole field in the overlap area. One can demonstrate that the same can be said about intercepting ellipses. Now, if we imagine a magnet coil cross-section given by two intercepting circles, we can notice that it would not be easy to fill the two areas with a Rutherford cable, in particular where the side areas become pointy, close to the vertical axis y of the aperture. Therefore, this "coil design", which can be in principle filled by strands, could only be roughly approximated if we use larger cables. Luckily, a second option can be studied: let's consider now a circular crown of width w carrying a current density j_o with a $\cos\theta$ distribution (see Fig. II.6.33 left), with a varying current density which is positive at the mid-plane and at 0° ($y = 0$, *right side*), then null at 90° ($x = 0$, *top*), then negative at the mid-plane and at 180° ($y = 0$, *left side*), then null again at 270° ($x = 0$, *bottom*). In this case, the magnetic field inside the aperture is perfectly vertical and given by

$$B_y = -\frac{\mu_0 j_0}{2} w \quad . \tag{II.6.25}$$

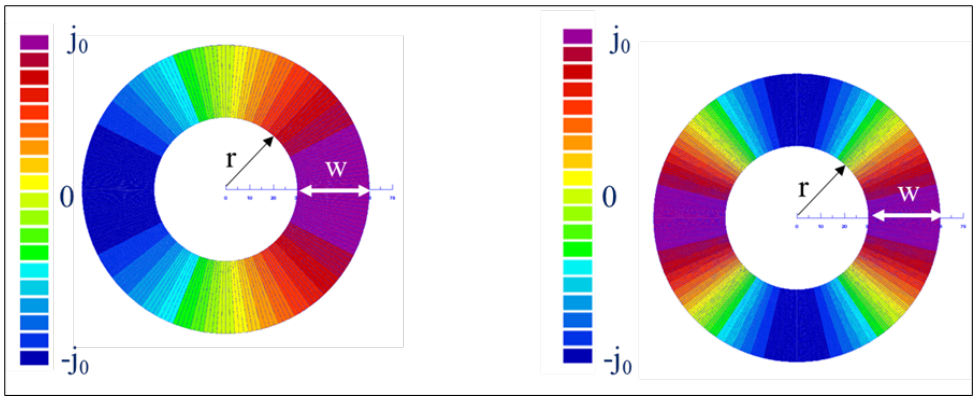

Fig. II.6.33: Thick shell with a $\cos\theta$ current density distribution on the left for a dipolar filed and a $\cos 2\theta$ current density distribution on the right for a quadrupolar field (image from S. Izquierdo Bermudez).

From this simple formula for a perfect $\cos\theta$ current distribution in a thick shell, we derive three important conclusions for the magnetic field at its interior:

1. depends linearly on the current density;
2. depends linearly on the coil width;
3. does not depend on the coil aperture (r being the inner (aperture) radius in Fig. II.6.33).

In a similar way, one can obtain a perfect quadrupole field from a current density distribution with a $\cos 2\theta$ (and so on, i.e. a perfect sextupole with a $\cos 3\theta$ current density distribution... a perfect *2n-pole* with $\cos n\theta$ current density distribution...) as shown in Fig. II.6.33 (right). For a quadrupole, the gradient G [T/m] is given by

$$G = -\frac{\mu_0 j_0}{2} \ln\left(1 + \frac{w}{r}\right) \quad . \tag{II.6.26}$$

Therefore, in a quadrupole, the gradient does not depend only on the coil width w, but also on the coil aperture r.

The thick shell configuration, unlike the intercepting circles/ellipses one, appears to be more manageable with Rutherford cables, in the sense that one could stack cables to fill the coil area. Theoretically a $\cos\theta$ distribution could be achieved only by having progressively lower currents moving from the cables close to the mid-plane to the ones close to 90°, which is practically impossible to achieve.

One can therefore attempt to approximate a perfect $\cos\theta$ distribution in a different way, still under the constraint that we want to use Rutherford cables, i.e. cables with rectangular of trapezoidal cross-sections, all carrying the same currents. Two examples are shown in Fig. II.6.34. The first is called a sector coil, which is probably the simplest and most rough approximation of a $\cos\theta$ distribution: the coil is characterized by a single area with a constant current density from the mid-plane up to a given angle (usually about 60°). This design is the simplest attempt to simulate a $\cos\theta$ condition where most of the current is placed towards the mid-plane and none at the pole. The second option is a more complex one, where blocks of conductors are separated by wedges which contribute to progressively reduce the coil current "density" while moving from the mid-plane to the pole. These coils are named $\cos\theta$ coils.

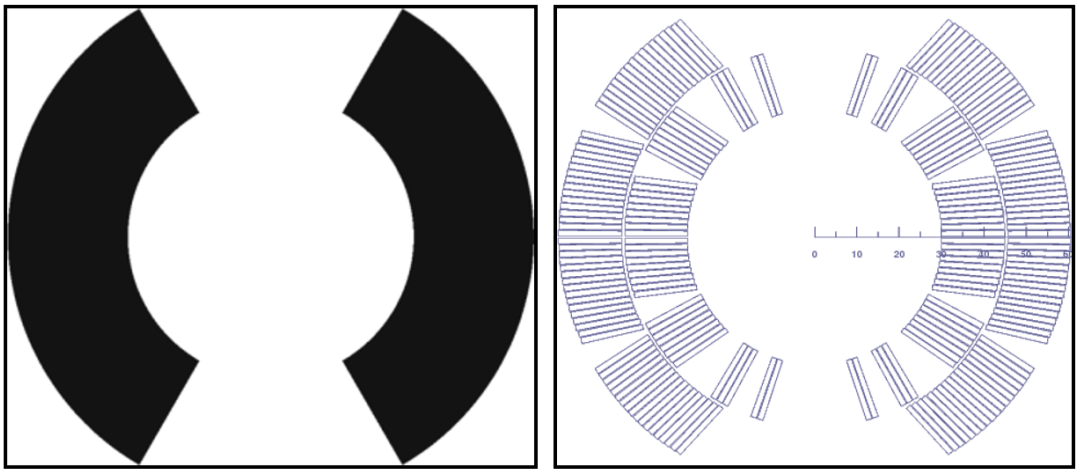

Fig. II.6.34: Cross section of a sector coil (left) and the positioning of Rutherford cables in the sector for a "real" $\cos\theta$ coil (right).

Both these options simulate only a perfect $\cos\theta$ current distribution, and produce a field in the aperture which is not a perfect dipole. In other words, the field in the aperture will contain field errors with respect to a perfect dipole (vertical) field. In the next sub-section we will discuss the way these field errors or imperfections are defined.

II.6.4.2 How do we express the field and its "imperfections"?

Let's start from the Maxwell equations for magnetic field, i.e.

$$\begin{cases} \nabla \cdot B &= \frac{\partial B_x}{\partial x} + \frac{\partial B_y}{\partial y} + \frac{\partial B_z}{\partial z} \\ \nabla \times B &= \mu_0 \, J \, + \, \mu_0 \, \epsilon_0 \, \frac{\partial E}{\partial t} \end{cases} \quad . \tag{II.6.27}$$

Let's now have again a look at the image of a superconducting coil of the Fig. II.6.4 (top left) in Section II.6.2, and let's imagine to put ourselves inside the bore tube and in the center (in the z direction) of the straight section of the coil. In that region, there are no charges nor magnetized material, so we can rewrite the second Eq. II.6.27 as

$$\nabla \times B \begin{cases} \frac{\partial B_y}{\partial z} - \frac{\partial B_z}{\partial y} &= 0 \\ \frac{\partial B_z}{\partial x} - \frac{\partial B_x}{\partial z} &= 0 \\ \frac{\partial B_x}{\partial y} - \frac{\partial B_y}{\partial x} &= 0 \end{cases} \quad , \tag{II.6.28}$$

and since we also have no variations along z of the magnetic field (we are in the straight section), then, from the first Eq. II.6.27 and Eq. II.6.28

$$\begin{cases} \frac{\partial B_x}{\partial y} - \frac{\partial B_y}{\partial x} &= 0 \\ \frac{\partial B_x}{\partial x} + \frac{\partial B_y}{\partial y} &= 0 \end{cases} \quad . \tag{II.6.29}$$

The first Eq. II.6.27 and Eq. II.6.28 are in fact the Cauchy-Riemann conditions

$$\begin{cases} \frac{\partial f_x}{\partial y} - \frac{\partial f_y}{\partial x} &= 0 \\ \frac{\partial f_x}{\partial x} + \frac{\partial f_y}{\partial y} &= 0 \end{cases} \quad , \tag{II.6.30}$$

applied to the magnetic field. This implies that the function $B_y + i\, B_x$ is analytic and can be written as

$$B_y(x,y) \, + \, i \, B_x(x,y) \, = \sum_{n=1}^{\infty} C_n (x + i\, y)^{n-1} \quad , \tag{II.6.31}$$

where C_n are complex coefficients

$$B_y(x,y) \, + \, i \, B_x(x,y) \, = \sum_{n=1}^{\infty} (B_n + i\, A_n)(x + i\, y)^{n-1} \quad . \tag{II.6.32}$$

To summarize, the fact that we are inside a volume without currents and with no magnetic field variations along the longitudinal axis of the coil allows us to describe the field inside the aperture as a sum of coefficients. Each coefficient represents a pure multipolar field, as shown in Fig. II.6.35. This expression constitutes a major advantage for the design of a superconducting coil, because we manage to express the field as a series of individual components. In a dipole magnet for example, we have B_1,

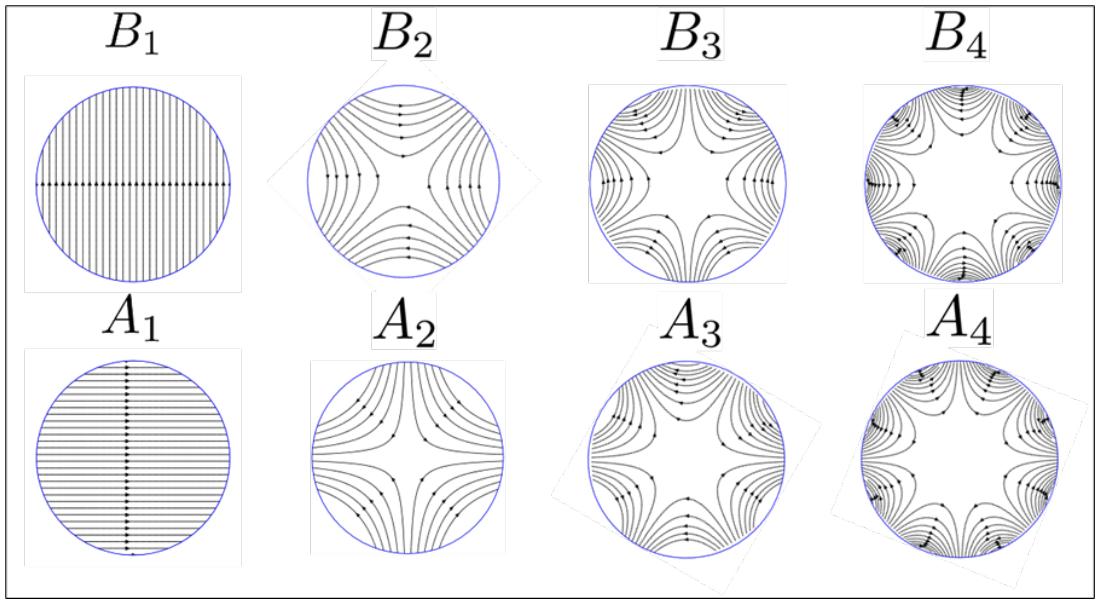

Fig. II.6.35: "Pure" multipolar fields (image by J.L. Ruideros Fernandez).

which is the multipole that we want, and all the others multiples $(A_1, B_2, A_2, B_3 \dots)$ which are the "errors" or "field imperfections" that we want to minimize. Eq. II.6.32 is usually rewritten for a dipole in the following way

$$B_y + i\,B_x = 10^{-4}\,B_1 \sum_{n=1}^{\infty} (b_n + i\,a) \left(\frac{x + i\,y}{R_{\text{ref}}} \right)^{n-1} \quad , \tag{II.6.33}$$

where we factorized the main component (B_1 for dipoles, B_2 for quadrupoles), we introduce a reference radius R_{ref} (usually chosen as 2/3 of the aperture radius) to have dimensionless coefficients, and we factorize 10^{-4} since the deviations from ideal field are of the order $\sim 0.01\%$. The coefficients b_n, a_n are called normalized multipoles or harmonics: b_n are the normal, a_n are the skew (non-dimensional), and they are expressed in "units" of 10^{-4} with respect to the main field.

II.6.4.3 How do we design a coil to minimize field errors?

II.6.4.3.1 Step 1: symmetric distribution of currents

Let's consider now a current distribution with a dipole symmetry, that is with an up-down symmetry (with same current sign) and left-right symmetry (with opposite current sign), as shown in Fig. II.6.36 (left). One can demonstrate that with line currents with such a distribution most of the multipoles cancel.

In particular, for a dipole, i.e. for $n = 1$, only the *odd normal multipoles* like $b_3, b_5, b_7, \dots$ are present, while all the *even normal multipoles* (like $b_2, b_4, b_6, \dots$) and all the *skew multipoles* (like $a_1, a_2, a_3, \dots$) are null. For this reason, the odd normal multipoles are called the allowed multipoles. In a quadrupole symmetric distribution, like the one shown in Fig. II.6.36 (right), the same happens, but this time the allowed multipoles are the $b_6, b_{10}, b_{14}, \dots$.

Therefore, when we design a superconducting dipole (or quadrupole) magnet, the simple fact of

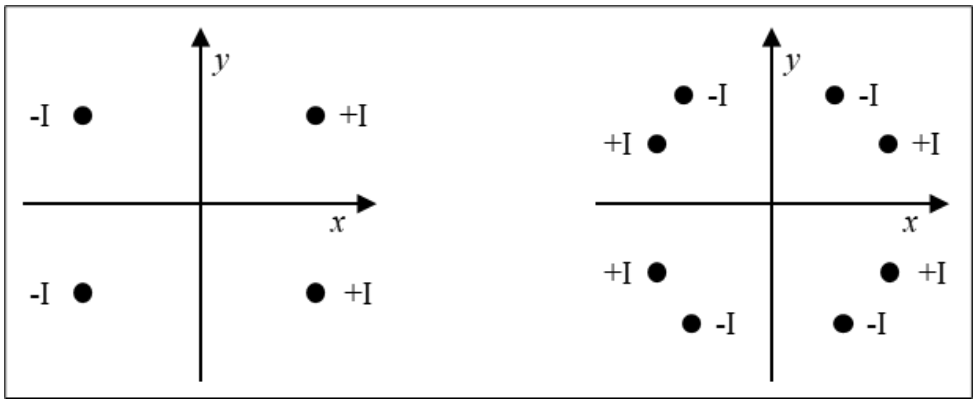

Fig. II.6.36: Current distribution with dipole (left) and quadrupole (right) symmetry.

having a dipole (or a quadrupole) symmetry allows us to focus only on few multipoles. This is true on paper, since in reality it is basically impossible to build a coil with the turns positioned in a perfectly symmetric way (due to tolerances of fabrication of the coil itself and of the components surrounding the coil). But at least in the design phase, we do not have to worry about most of the harmonics.

II.6.4.3.2 Step 2: sub-division of a coil in blocks

In order to further minimize the field errors, now we focus "only" on the allowed harmonics. Let's consider a sector coil of width w, aperture radius r, angle α (see Figure II.6.37) and with a dipole current distribution of uniform current density j. By using the Biot-Savart law and integrating over the coil cross-section,

$$I \rightarrow j\,\rho\,d\rho\,d\theta \quad , \tag{II.6.34}$$

one can compute the central field, which is given by

$$B_1 = -2\frac{j\,\mu_0}{2\pi}\int_{-\alpha}^{+\alpha}\int_{r}^{r+w}\frac{\cos\theta}{\rho}\rho\,d\rho\,d\theta = -\frac{2j\,\mu_0}{\pi}w\,\sin\alpha \quad . \tag{II.6.35}$$

From this formula one can notice that, in a similar way as with the shell with a $\cos\theta$ distribution (Eq. II.6.23), the dipole field depends on j, on the coil width w, but not of the coil aperture r. Using a similar approach, we can express not only the main dipole field, but also all the multipoles, i.e.

$$B_n = -\frac{j\,\mu_0\,R_{\text{ref}}^{n-1}}{\pi}\frac{2\sin(\alpha n)}{n}\frac{(r+w)^{2-n}-r^{2-n}}{2-n} \quad . \tag{II.6.36}$$

This formula shows that the multipoles of order n are proportional to $\sin\alpha n$ and therefore, by choosing the right α we can cancel each of them. For example, if we look at the previous formula and we consider the B_3

$$B_3 = -\frac{2j\mu_0\,R_{\text{ref}}^2}{\pi}\frac{\sin 3\alpha}{3}\left(\frac{1}{r}-\frac{1}{r+w}\right) \quad . \tag{II.6.37}$$

We see that we can bring to zero the first allowed harmonic with an angle of $\alpha = \frac{\pi}{3}$. This is why when we consider a simple sector coil, we usually choose a 60°angle. The second allowed multipole B_5

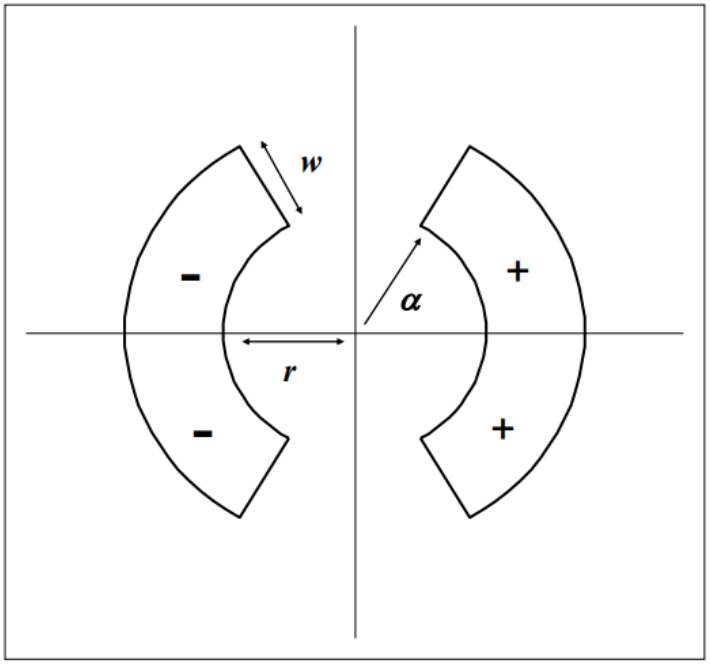

Fig. II.6.37: Schematics of a sector coil.

$$B_5 = -\frac{2j\,\mu_0\,R_{\text{ref}}^4}{\pi}\frac{\sin 5\alpha}{15}\left(\frac{1}{r^3}-\frac{1}{(r+w)^3}\right) \quad . \tag{II.6.38}$$

will be zero with an angle of $\frac{\pi}{5}$ (a 36°sector coil) or for $\frac{2\pi}{5}$ (a 72°sector coil).

In this way, we can easily cancel all the harmonics, one at the time. However, ideally one would like to bring to zero not simply one allowed harmonic at a time, but as many as possible simultaneously.

We can now start considering a sector coil with more than one block of windings (and one angle), that is two blocks (and three angles), like the one shown in Fig. II.6.38.

This coil can be seen as a sector coil with an angle of α_3, to which a sector with an angle of α_2 has been removed and replaced by a sector coil with an angle of α_1. The first three allowed multipoles generated by this two-blocks coil

$$\begin{cases} B_3 &= -\frac{2j\,\mu_0\,R_{\text{ref}}^2}{\pi}\,\frac{\sin(3\alpha_3)-\sin(3\alpha_2)+\sin(3\alpha_1)}{3}\left(\frac{1}{r}-\frac{1}{r+w}\right) \\ B_5 &= -\frac{2j\,\mu_0\,R_{\text{ref}}^4}{\pi}\,\frac{\sin(5\alpha_3)-\sin(5\alpha_2)+\sin(5\alpha_1)}{5}\left(\frac{1}{r^3}-\frac{1}{(r+w)^3}\right) \\ B_7 &= -\frac{2j\,\mu_0\,R_{\text{ref}}^6}{\pi}\,\frac{\sin(7\alpha_3)-\sin(7\alpha_2)+\sin(7\alpha_1)}{35}\left(\frac{1}{r^5}-\frac{1}{(r+w)^5}\right) \end{cases} \quad . \tag{II.6.39}$$

Therefore, solving the system given by

$$\begin{cases} \sin(3\alpha_3)-\sin(3\alpha_2)+\sin(3\alpha_1) &= 0 \\ \sin(5\alpha_3)-\sin(5\alpha_2)+\sin(5\alpha_1) &= 0 \\ \sin(7\alpha_3)-\sin(7\alpha_2)+\sin(7\alpha_1) &= 0 \end{cases} \quad , \tag{II.6.40}$$

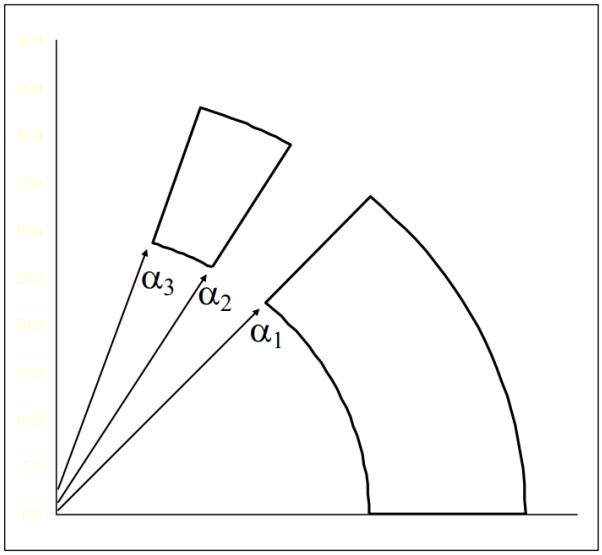

Fig. II.6.38: Schematics of a sector coil with two blocks.

we can find a solution that cancels the first three allowed multipoles at the same time. The solution is shown in Fig. II.6.39, left: a coil with two blocks, one wedge, and with angles 43.2°, 52.2°and 67.3°will have zero B_3, B_5 and B_7.

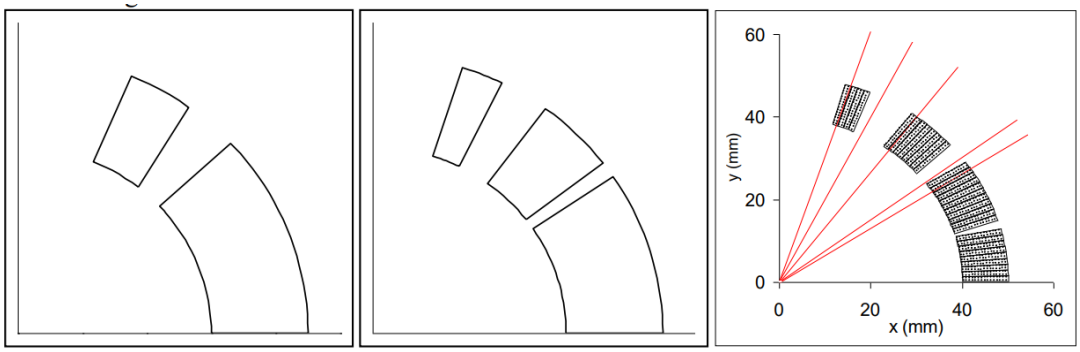

Fig. II.6.39: Left: two-blocks coil with two wedges, angles 43.2°, 52.2°and 67.3°and $B_3 = B_5 = B_7 = 0$. Center: three-blocks coil with two wedges, angles 33.3°, 37.1°, 53.1°, 63.4°, 71.8°and $B_3 = B_5 = B_7 = B_9 = B_{11} = 0$. Right: the RHIC main dipole coil cross-section and comparison with the analytical angles (red lines).

We can push further the optimization, and consider now a three blocks coil and two wedges.

By solving the system

$$\begin{cases} \sin(3\alpha_5) - \sin(3\alpha_4) + \sin(3\alpha_3) - \sin(3\alpha_2) + \sin(3\alpha_1) & = 0 \\ \sin(5\alpha_5) - \sin(5\alpha_4) + \sin(5\alpha_3) - \sin(5\alpha_2) + \sin(5\alpha_1) & = 0 \\ \sin(7\alpha_5) - \sin(7\alpha_4) + \sin(7\alpha_3) - \sin(7\alpha_2) + \sin(7\alpha_1) & = 0 \\ \sin(9\alpha_5) - \sin(9\alpha_4) + \sin(9\alpha_3) - \sin(9\alpha_2) + \sin(9\alpha_1) & = 0 \\ \sin(11\alpha_5) - \sin(11\alpha_4) + \sin(11\alpha_3) - \sin(11\alpha_2) + \sin(11\alpha_1) & = 0 \quad , \end{cases} \tag{II.6.41}$$

we find the angles (33.3°, 37.1°, 53.1°, 63.4°, 71.8°) that cancel $B_3, B_5, B_7, B_9, B_{11}$ (see Fig. II.6.39, center), and that match well the ones of the RHIC main dipole coil (see Fig. II.6.39, right).

One can apply the same principle for the design of a quadrupole coil, keeping in mind that, with respect to a dipole, angles have to be divided by two and multipole orders have to be multiplied by two. Therefore, the first allowed multipole for a quadrupole sector coil is given by

$$B_6 = -\frac{2j\,\mu_0\,R_{\text{ref}}^5}{\pi}\,\frac{\sin(6\,\alpha)}{24}\left(\frac{1}{r^4} - \frac{1}{(r+w)^4}\right) \quad , \tag{II.6.42}$$

and its effects can be cancelled with a one-block sector coil with an angle of 30°.

II.6.4.4 Which is the maximum field we can obtain?

After showing how to improve the field quality of a coil, we can address the magnitude of the field a coil can produce. The formula for the dipole sector coil is

$$B_1 = -\frac{2\,j_0\,\mu_0}{\pi}\,w\,\sin\alpha \quad , \tag{II.6.43}$$

the field depends on the coil width w. However, when estimating the maximum limit of the field that can be produced by the coil, one has to consider that, for a given overall current density j_o, the coil will experience a peak field slightly higher than the bore field. We call this field the conductor peak field. In a thick shell with a $\cos\theta$ current distribution, a configuration that produces a perfect dipole field, the bore field is identical to the maximum field in the coil. Instead in a sector coil, which by design does not produce a perfect dipole, the conductor peak field is higher than the bore field, typically by some %. One can see this ratio as the "price" we have to pay for not having a perfect $\cos\theta$ current distribution, but only an approximation of it. If we define as λ_{peak} the ratio between the conductor peak field and the bore field, and we plot it as a function of the coil width, one can see from Fig. II.6.40 top panel, that this ratio ranges between about 1.05 for thick coils to about 1.15 for thin coils.

Now, the conductor peak field B_{peak}, being the higher field in the superconducting coil, is a critical parameter since it determines, or better, limits the maximum field the coil can produce in the aperture (or bore), which we call B_1 (or B_{bore}). This is visualized in Fig. II.6.41 where the plot shows the critical curve of the superconductor (the dashed line) or the current density in the superconductor as a function of the field in the superconductor, for a given temperature (it is here 1.9 K for Nb_3Sn).

On this plot one sees a load-line (the black solid line) which is the curve that provides the peak field reached in the coil for a given current density flowing in the superconductor. The crossing point between

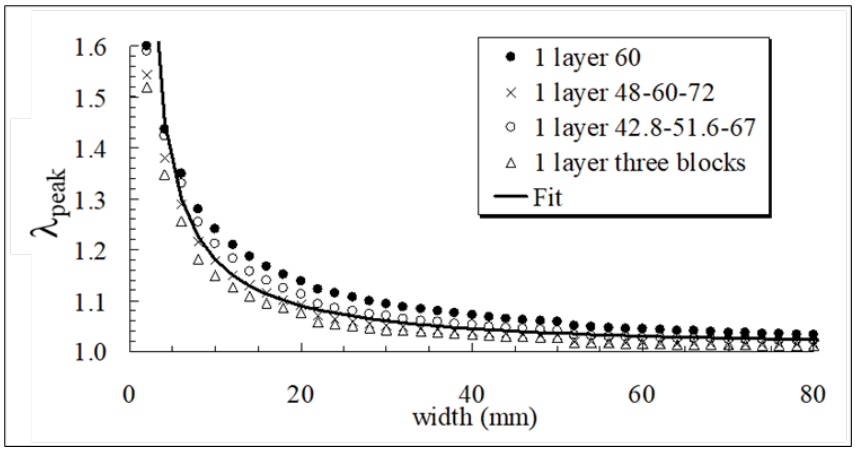

Fig. II.6.40: Ratio between the conductor peak field and the bore field λ_{peak} as a function of sector coil width, for different number of coil blocks and for an aperture radius of 25 mm.

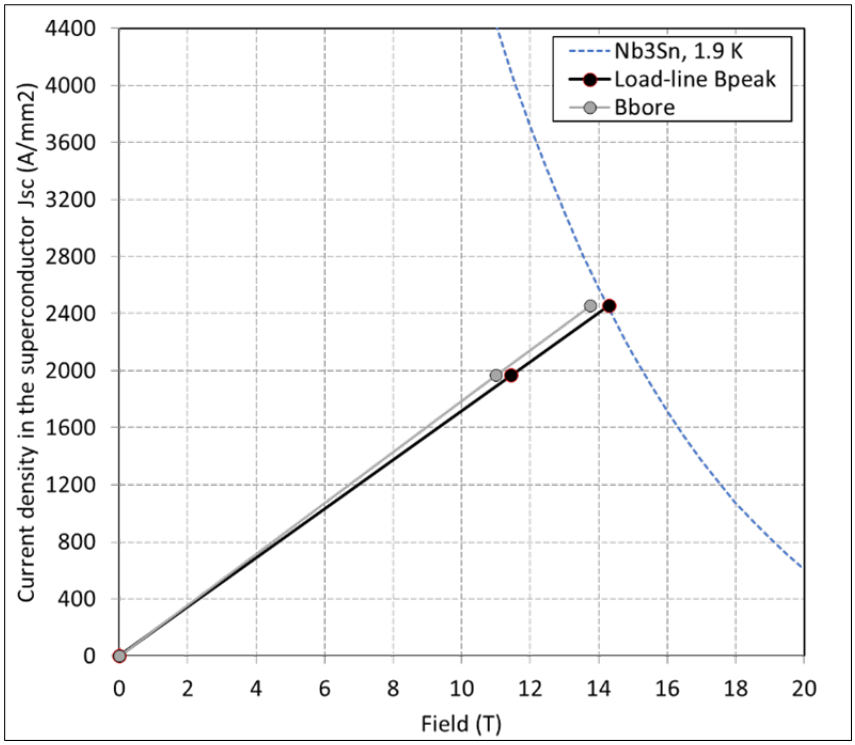

Fig. II.6.41: Critical curve for Nb_3Sn (dashed line), load-line (B_{peak}) and bore field (B_{bore}) at a temperature of 1.9 K.

the critical curve and the load-line represent the limit of the superconductor at the given operational temperature. There is however an important aspect to keep in mind: Eq. (II.6.43) for the sector coil links the overall current density j_{o} and B_{bore}, but in order to determine the limits, what we actually need is the current density in the superconductor j_{sc} and the peak field B_{peak}. Only with these two parameters we

can compare the critical curve and the load-line. So, we rewrite the formulas as

$$\begin{cases} B_1 &= -\frac{2\,\kappa\,j_{\rm sc}\,\mu_0}{\pi}\;w\;\sin\alpha \\ B_{\rm peak} &= -\lambda_{\rm peak}\frac{2\,\kappa\,j_{\rm sc}\,\mu_0}{\pi}\,w\;\sin\alpha \end{cases} \quad , \tag{II.6.44}$$

where κ is the filling factor defined at the end of Section II.6.3. This formula is indeed the correct expression of the magnet load-line, which is used to determine the maximum current density we can flow in a superconductor before crossing the critical curve (black marker on the critical curve), and the corresponding bore field (grey marker close to the critical curve). The maximum field and current determined in this way are called *short sample field and current* (since the critical curve is determined by measuring the properties of a "short-sample" of superconducting strands).

Superconducting magnets never operate at a current corresponding to the short sample limit (i.e. on the critical curve), since any perturbation could cause a quench. Therefore a safety margin is usually included, of the order of about 20% on the load-line (the ratio between the operational current and the short sample current is 0.8). Assuming an operational current density of 80% of the maximum current density, we can estimate the maximum operation field we can achieve in a superconducting dipole with a sector coil. Results are shown in Fig. II.6.42.

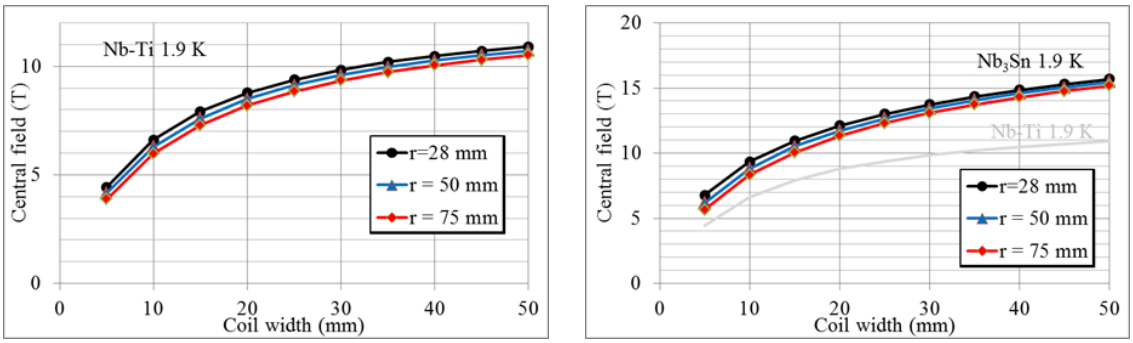

Fig. II.6.42: Maximum bore field, for Nb-Ti and Nb_3Sn dipole sector coil, assuming an operational margin of 20%.

As can be seen from the plots, beyond a 30-40 mm coil width, the increase of maximum achievable field reduces significantly, and the use of very large coils becomes inefficient, at least from the point of view of conductor use. Also, we may conclude that the maximum operation bore field for a Nb-Ti magnet is about 10 T, and for a Nb_3Sn, of about 15 T, assuming a 20% operational margin.

A similar analysis can be done for a quadrupole. The formula for the quadrupole gradient (T/m) for a sector coil is

$$G \;=\; -\frac{2\,j_0\,\mu_0}{\pi}\;\sin\alpha\;\ln\left(1+\frac{w}{r}\right) \quad , \tag{II.6.45}$$

with $\alpha = 30°$to cancel the first allowed multiple (B_6). In a quadrupole we cannot use the bore field and we define $\lambda_{\rm peak}$ as the ratio between the peak field in the conductor and the gradient multiplied by the aperture $G\,r$. The plot of $\lambda_{\rm peak}$ for a quadrupole has a more complex profile and is shown in Fig. II.6.43.

By combining Eq. (II.6.45) with $\lambda_{\rm peak}$ and the superconductor critical curves, we find the limit for

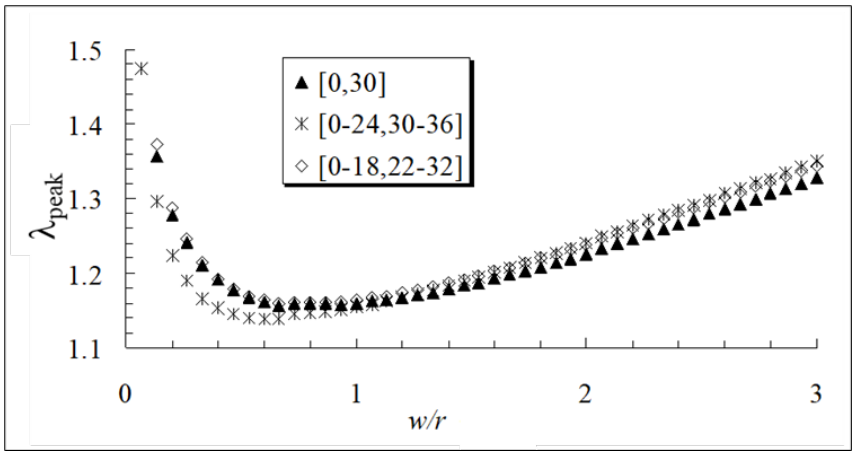

Fig. II.6.43: Ratio between the conductor peak field and $G\,r$ as a function of the ratio between sector coil width and aperture radius, and for different number of blocks.

the Nb-Ti and Nb_3Sn quadrupole magnets, which are shown in Fig. II.6.44.

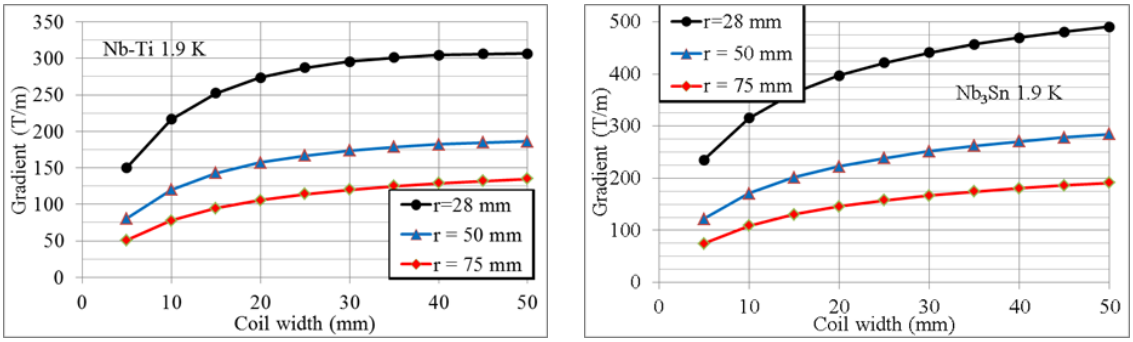

Fig. II.6.44: Maximum gradient for Nb-Ti and Nb_3Sn quadrupole sector coil, assuming an operational margin of 20%.

Quadrupole magnets exhibit a more pronounced saturation compared to dipole magnets, making extremely inefficient the use of very large coils.

II.6.4.5 Effect of iron yoke.

Any cross-section of superconducting magnet for particle accelerator has an iron yoke, i.e. a component of ferromagnetic material surrounding the coil. The iron yoke may have a mechanical function, which will be addressed in the next section. From the magnetic point of view, the iron yoke has the functions to:

1. Keep the return magnetic flux close to the coil, thus minimizing the fringe field (see Fig. II.6.45);
2. Enhance the bore field for a given current density.

The iron yoke can significantly increase the bore field for a given current density in the coil. The increase is particularly relevant with thin coils, and allows using a lower current density to achieve the

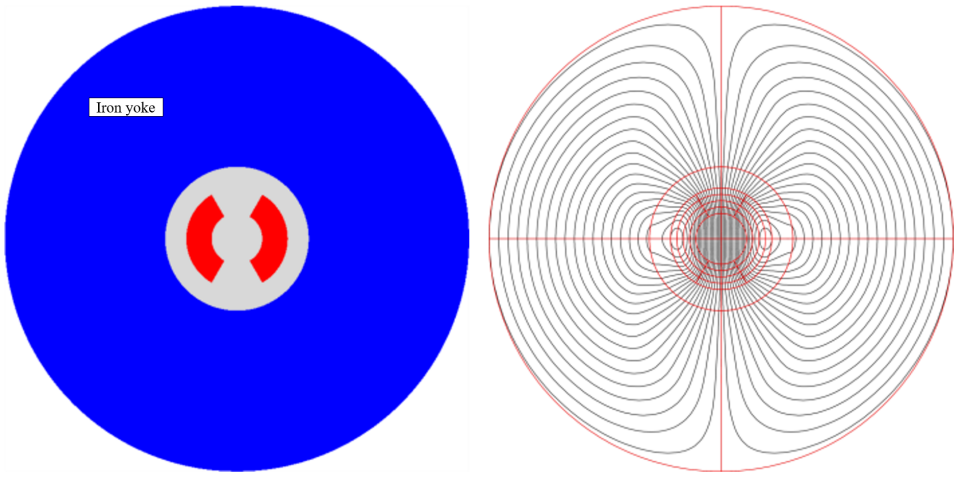

Fig. II.6.45: Schematic cross-section of a magnet (left) with one sector coil and an iron yoke and profile of the magnetic flux-lines (right).

same target field, with significant advantages both from the mechanical (see Section II.6.5) and quench protection (Section II.6.6) point of view.

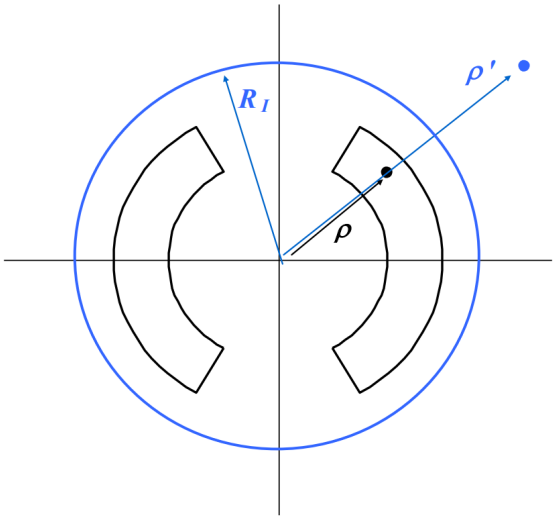

Fig. II.6.46: Representation of the current image method.

A rough estimate of the iron thickness necessary to avoid field lines outside the magnet can be written as

$$r\,B_{\rm bore} \sim t_{\rm iron}\,B_{\rm sat} \quad , \tag{II.6.46}$$

where r is the coil aperture radius, $t_{\rm iron}$ is the radial thickness of the iron yoke, and $B_{\rm sat}$ is the saturation field, which can be assumed as 2 T.

Basically the formula states that the iron thickness is such that all the field lines in the aperture go

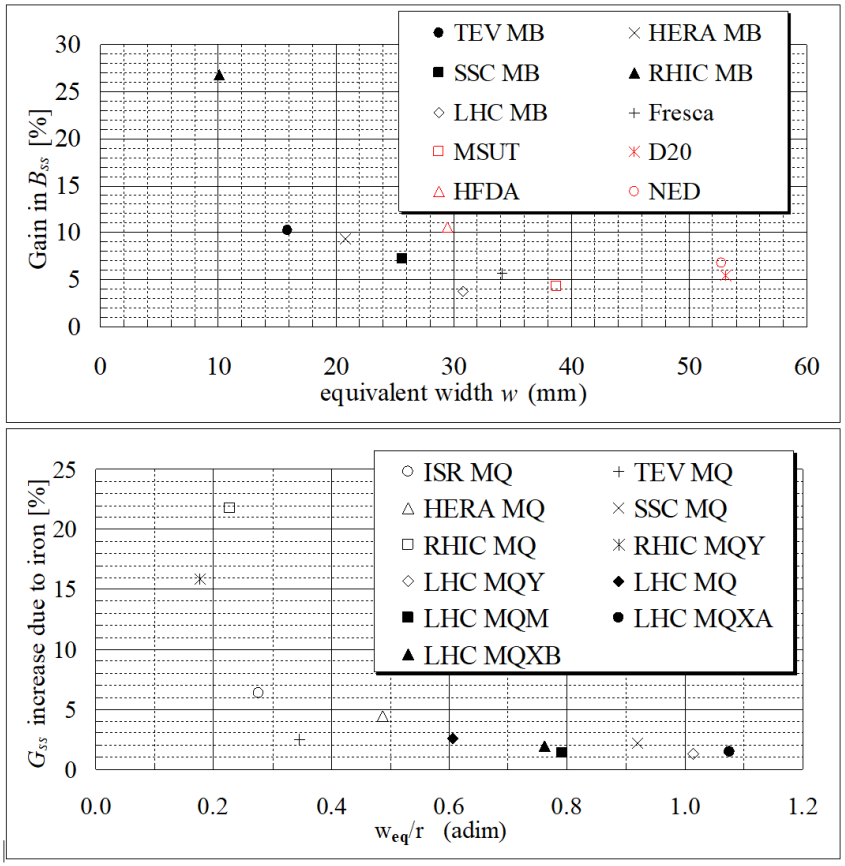

Fig. II.6.47: Increase in short sample bore field value due to iron yoke in dipoles (top) and quadrupoles (bottom) magnets.

through the iron, assumed to be at 2 T, that therefore is not saturated. If for example we consider the LHC main dipole (28 mm radius aperture and 9 T maximum bore field), and iron yoke of 150 mm thick the formula would give us a thickness of $\sim$ 130 mm.

The iron yoke contribution can be estimated analytically for simple geometries using the *image currents method* (see Fig. II.6.46): for a non-saturated circular iron yoke, the effect is equivalent to add to each current line I at a radius ρ a second one I' at a radius ρ' given by

$$\begin{cases} I' &= \frac{\mu-1}{\mu+1} I \\ \rho' &= \frac{R_I^2}{\rho} \end{cases} , \tag{II.6.47}$$

where R_I is the inner radius of the iron yoke with permeability μ.

In term of maximum short sample field ($B_{\rm ss}$) and gradient ($G_{\rm ss}$), the increase for different dipole and quadrupole magnets is shown in Fig. II.6.47. It can be noticed that we have a large effect (25%) with thin coils (see the RHIC dipole), but generally the increase is ranging within 5–10 % for dipoles and 1–5% for quadrupoles.

II.6.4.6 Overview of different dipole and quadrupole designs

We conclude the section on magnetic design with an overview of dipole and quadrupole coil cross-sections in Fig. II.6.48 and Fig. II.6.49, reminding that the coil thickness is the key parameter to reach progressively higher bore field, and the number of wedges and blocks the key to improve the field quality and approximate an ideal $\cos\theta$ current (or intersecting circles/ellipses) distribution.

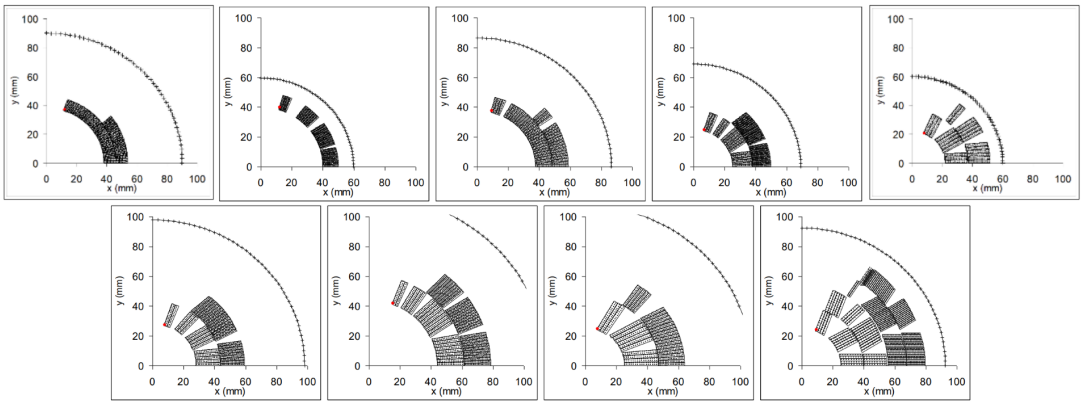

Fig. II.6.48: Overview of different dipole coil cross-sections. From left to right and from top to bottom: Tevatron MB, RHIC MB, HERA MB, SSC MB, HFDA dipole, LHC MB, FRESCA, MSUT, D20 [2].

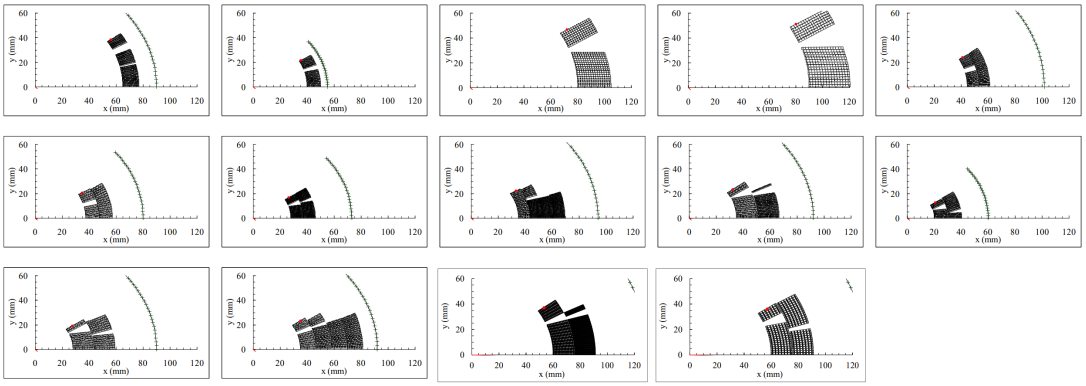

Fig. II.6.49: Overview of different quadrupole coil cross-sections. From left to right and from top to bottom: RHIC MQX, RHIC MQ, LEP II MQC, LEP I MQC, Tevatron MQ, HERA MQ, HC MQM, LHC MQY, LHC MQXB, SSC MQ, LHC MQ, LHC MQXA, LHC MQXC, LARP HQ [2].

II.6.5 Mechanics and magnet fabrication

In this Section we will discuss the mechanics of superconducting magnets.

We will start showing how a coil is fabricated. We will then discuss the electromagnetic forces that are generated in the coil when the magnet is powered. Finally, after introducing the concept of the pre-stress, we will describe the different types of support structures.

II.6.5.1 Coil fabrication

The coil is the most critical components of a superconducting magnet: it is the active element that has to produce the magnetic field, and when assembled in the structure has to meet the field quality requirements. High cross-sectional accuracy over up to 15 m length must be reached for field quality requirements. Coils are usually fabricated with laminated tooling: very accurate laminations can be fabricated at low cost and assembled in long lengths. The coil fabrication can be divided in the following steps:

1. Winding and curing, both for Nb-Ti and Nb_3Sn coils;
2. Reaction, and impregnation, only for Nb_3Sn coils.

II.6.5.1.1 Winding and curing

The cable is wound around a winding pole mounted on a steel mandrel (see Fig. II.6.50).

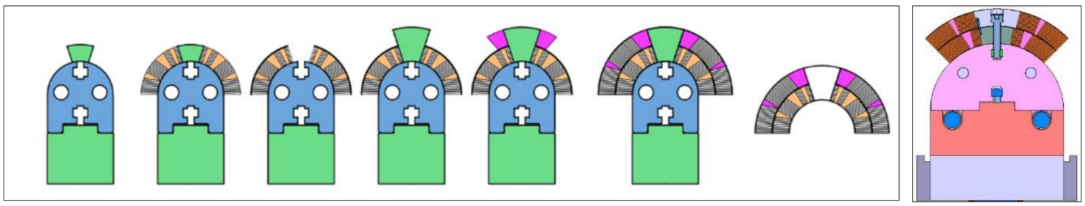

Fig. II.6.50: Left: Cross-section view of the steps of the winding process for the CERN 11 T coil. Right: Cross-section of an MQXF coil on the mandrel.

A continuous length of insulated cable sufficient for one coil is wound on a spool. Then, from the spool, the cable is wound around a pole mounted on a steel mandrel. The mandrel is composed of laminations mounted on a beam. Winding starts from the pole turn of the inner layer after preparing the coil ramp for the outer layer. The cable is maintained in tension (for the MQXF coils, about 25 kg). For short models, a rotating mandrel is used (see Fig. II.6.51 left). For large production of long coils, coil winding is done with automated winding machines, where the cable spool, mounted on a motor driven wagon, moves around the mandrel (as shown in Fig. II.6.51, center and right).

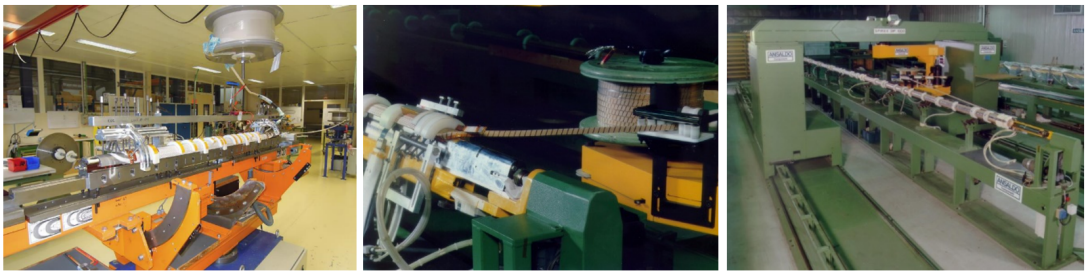

Fig. II.6.51: Left: winding machine for short coils with a rotating mandrel. Centre and right: winding machine for long coils.

During winding, particular attention is dedicated to the end regions where the cable is bent along both the narrow (hard-way bend) and the wide face (easy-way bend) of the ribbon cable, as shown in in

Fig. II.6.52 left. In order to keep the cable in position end spacers are designed to follow and support the cable while it moves from one side of the aperture to the other side. The path followed by the cable is chosen according to a "constant-perimeter" approach, where the two narrow edges of the cable follow curves of equal length, thus minimizing the strain. The shape of the spacer is therefore chosen to match the cable in the ends, their dimensions and positions are determined to optimize the field quality at the magnet end and to minimize the peak field.

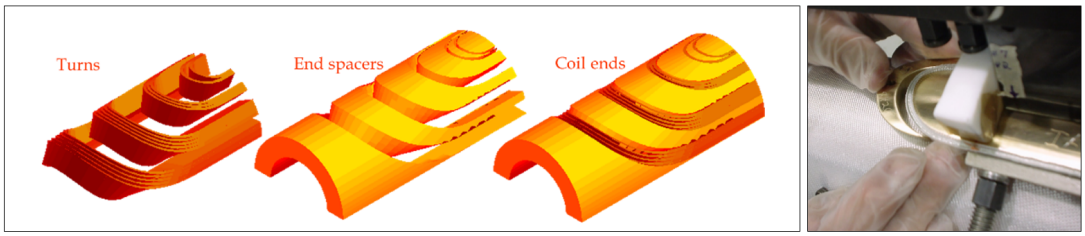

Fig. II.6.52: Left: separated view of the coils (Turns), end spacers and Coil ends. Right: inserting a metallic spacer around the pole turn.

The end-spacer for the Nb-Ti coils are usually fabricated with insulating materials, like fiberglass impregnated epoxy. For Nb_3Sn coils, given, as we will see later, that they have to be heat treated at the end of the process, materials that can withstand the high temperatures required are chosen, like stainless steel or Al-Br (see Fig. II.6.52 right).

The cable is continuously monitored during the winding to make sure that, in particular in the end region, the strands remain contained in their design cross section without "popped strands", i.e. strands which moved out with respect to their position after cabling (see Fig. II.6.53).

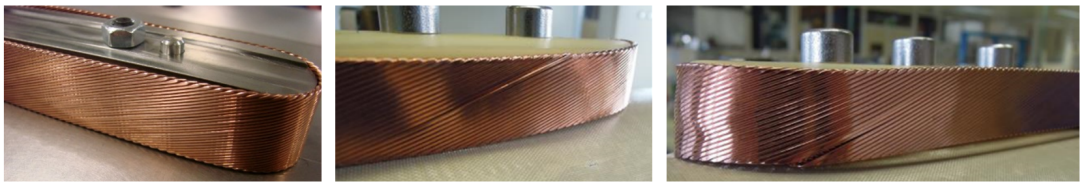

Fig. II.6.53: Pictures showing a cable wound without (left) and with "popped" strands (centre and right).

This phenomenon is usually associated to an excessive strain imposed to the cable at the ends and it can be linked to either a cable ribbon not sufficiently compacted or to a bending radius which is too tight. An iteration (or a series of iterations) aimed at optimizing the cable geometry and/or the coil and spacers geometry is not un-common after an initial winding test.

Once the winding is completed, the coils undergo the curing process. The curing is necessary to glue the turns of the coils, in order to:

1. Facilitate coil handling;
2. Define the coil dimensions;
3. In the case of double-layer coils, facilitate the winding of the second layer on top of the cured (and therefore more stable) inner layer.

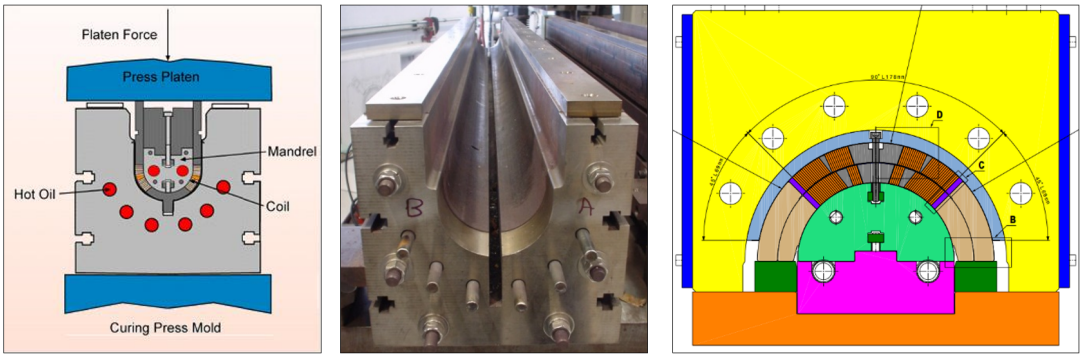

Fig. II.6.54: Cross section and a picture of curing moulds.

While still on the winding mandrel, the coils are placed in a curing mould (Fig. II.6.54) equipped with a heating system, and compressed inside a curing press. Both the pressure and the temperature vary significantly depending if one is dealing with Nb-Ti cables, insulated with polyimide, or Nb_3Sn cables, insulated with fiberglass. In both cases, the high temperature cures (or activates) the epoxy previously placed on the cable insulation, and glues the turns. With the end of the curing, the fabrication of the Nb-Ti coil is in general completed. Instead, for a Nb_3Sn coil, we have completed only the first step of a three-step process. In fact, at this point, niobium and tin are still in a separate form inside the cable strand (PIT), and no Nb_3Sn superconductor has been formed yet.

II.6.5.1.2 Reaction (or heat treatment)

The reaction or heat-treatment is the process through which the niobium-and-tin strands are brought to high temperature to promote the diffusion of the tin into the niobium. A typical heat treatment schedule for an RRP conductor is: 48 h at 210 °C (increase T by 25 °C/h), 48 h at 400 °C (increase T by 50 °C/h), 50 h at 665 °C (increase T by 50 °C/h).

Fig. II.6.55: Reaction fixture inserted in a reaction oven (CERN MQXFS coils).

The diffusion occurs in the last step, and it is shown for a PIT conductor in Fig. II.6.22, where the

tin from the core can be seen moving out to form Nb_3Sn (the light grey area around the core). The time and temperature of the last step are chosen carefully in order to maximize the area of Nb_3Sn, without breaking the external ring of niobium (the darker grey area), an event that would cause the contamination of the copper.

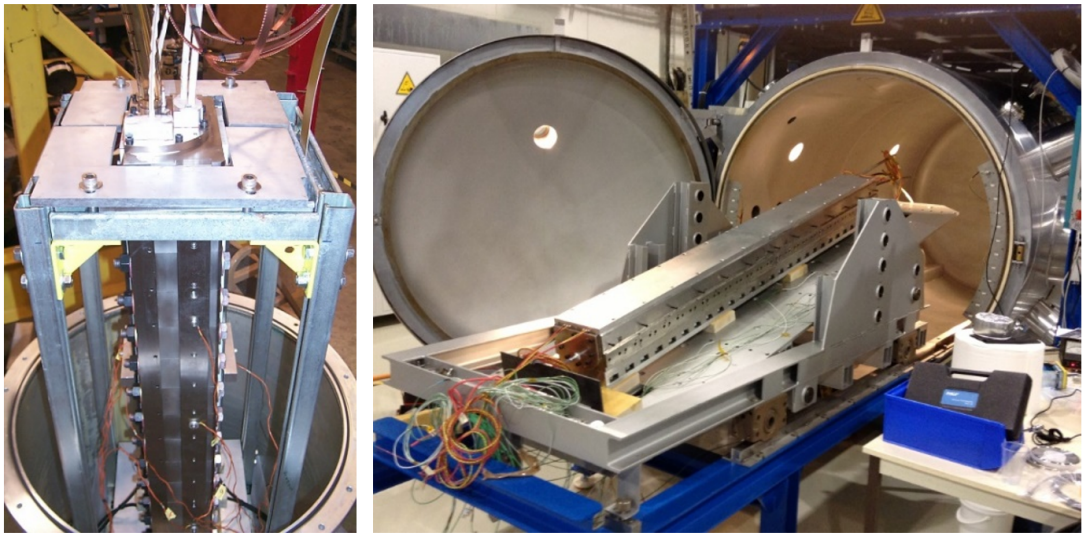

Fig. II.6.56: Impregnation of a LBNL TQ coil (left) and of a CERN MQXF coil (right).

Before the heat treatment the coil is transferred from the curing mould to the reaction fixture, made of stainless-steel blocks. The fixture is then inserted in the oven and the reaction takes place in an inert gas (argon) atmosphere. The presence of argon both inside the fixture (tubes injecting Argon are visible in Fig. II.6.55), and inside the oven (which is supposed to be leak tight) are aimed at minimizing the presence of oxygen, which could oxidize the copper in the strands, thus compromising their thermal and electric properties.

II.6.5.1.3 Impregnation

Once the reaction is completed, we have to remember that now the Nb_3Sn is formed, and therefore we are now dealing with a brittle conductor. The goal of the impregnation is indeed to surround the strands with a solid (and relatively rigid) material, to protect the coil during handling and assembly in the support structure. In other words, the resin transforms the coil in a sort of solid block, thus reducing the risk of damaging the conductor during the following assembly and loading operations.

The impregnation process consists of inserting the coil, placed inside a dedicated impregnation mould, inside a vacuum tank (see Fig. II.6.56). Then, once vacuum is obtained, epoxy is injected at atmospheric pressure or at 2 bar and at a temperature of 60 °C. In this condition, the epoxy has a very low viscosity, and fills the voids between the strands, air having been removed by the vacuum. The epoxy is cured at about 110-120°C for about 24 h. The final result can be seen in Fig. II.6.57 and Fig. II.6.58, where the aspect of Nb_3Sn coils after winding/curing, reaction, and impregnation is shown.

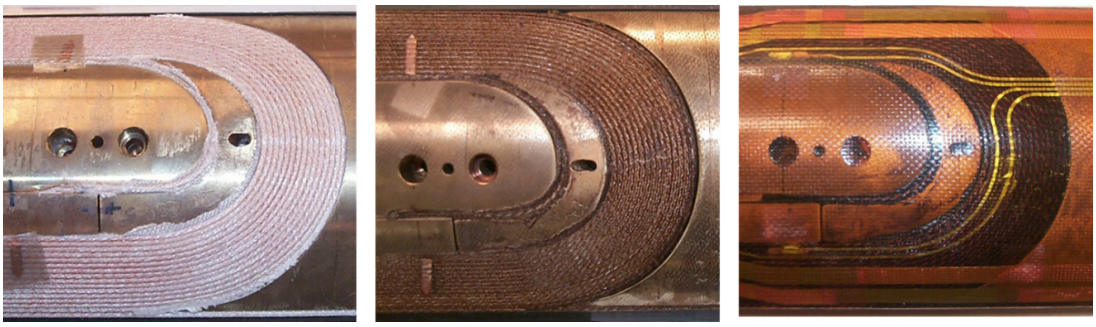

Fig. II.6.57: A LBNL TQ coil after winding/curing, reaction, and impregnation.

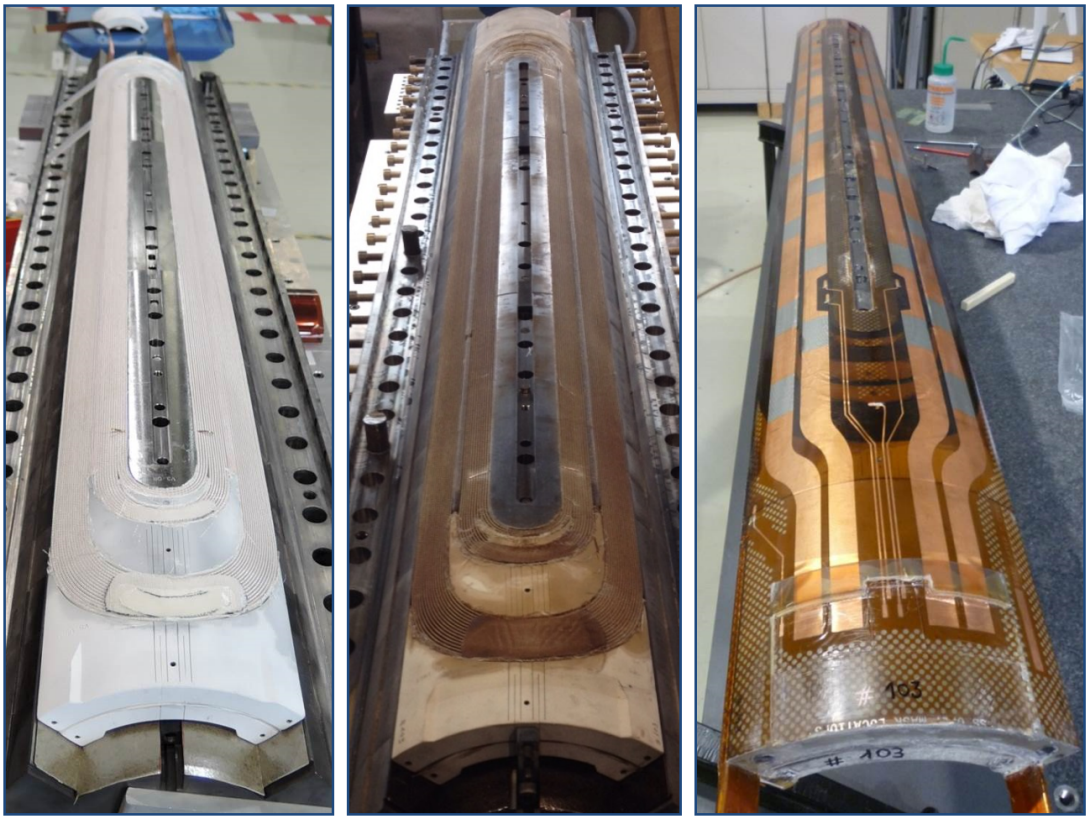

Fig. II.6.58: A CERN MQXFS coil after winding/curing, reaction, and impregnation.

II.6.5.2 Forces, stress, pre-stress

Superconducting magnets for particle accelerators are characterized by 4–15 T magnetic fields and overall current densities of the order of 500 A/mm^2. The combination of fields and currents generate inside the coil very large Lorentz forces, which may cause movements and deformations of the superconducting material. A good knowledge of the Lorentz forces, and of the induced stresses, is a fundamental element for the mechanical design of magnet support structure. In this section we will describe the Lorentz forces, the generated stresses and we will introduce the concept of *pre-stress*.

II.6.5.2.1 Electro-magnetic (or Lorentz) forces

In Section II.6.2, while explaining the main function of a superconducting magnet, we introduced the concept of Lorentz or electro-magnetic (e.m.) force applied to a charged particle moving inside the coil aperture: the force bends the particle trajectory. As we said (see Eq. II.6.3), in the presence of a magnetic field B [T], an electric charged particle q in motion with a velocity v is acted on by a force F_L [N], according to

$$\vec{F_L} = q\,\vec{v} \times \vec{B} \quad . \tag{II.6.48}$$

Magnet designers however must consider a specific Lorentz force. This force is due to the fact the coil itself is immersed in the magnetic field produced by the coil. An example can be seen in Fig. II.6.45: on the left we have a superconducting coil (in red) surrounded by the iron yoke (in blue), and on the right the flux lines produced by the coil when a current density j (A/mm^2) is applied, with the now well-known top-bottom symmetry and left-right asymmetry typical of a dipole configuration. The flux lines are concentrated in the coil aperture (where indeed we want the maximum field), and they bend inside the iron yoke, which has among his function to shield and contain them. Not only: the flux lines cross also the coil itself. This means that we have inside the coil the simultaneous presence of B and j, and as result of a Lorenz force density given by

$$\vec{f_L} = \vec{j} \times \vec{B} \quad . \tag{II.6.49}$$

The simplest way to analyze this magnetic force density is to start from a solenoid, schematically shown in Fig. II.6.59. In a solenoid, the current is running in the azimuthal direction θ, and the field inside the solenoid aperture is directed in the z direction.

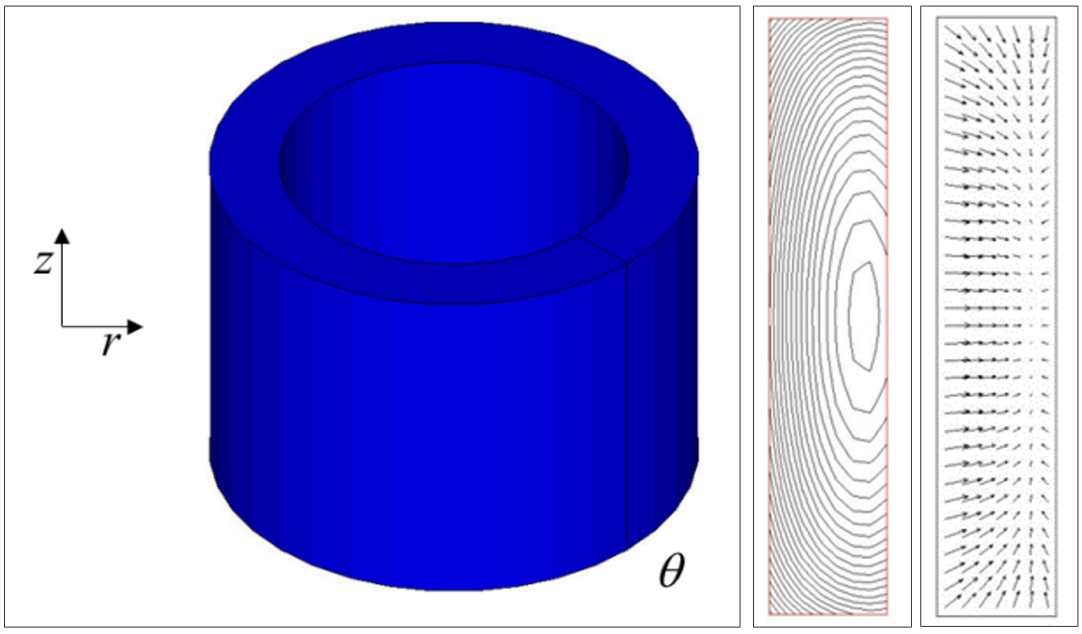

Fig. II.6.59: Schematic view of a solenoidal coil (left), flux lines on a cross-section of the solenoidal coil (centre), and direction of the Lorentz forces (right).

If we take a cross-section of the coil, we see that the flux lines inside the coils are mainly along the axis (vertical for the Figure), and as a result, if we apply the right-hand-rule, the Lorentz forces are mainly directed outwardly in the radial r direction. We can therefore conclude that the magnetic field is acting on the coil as a pressurized gas on its container. In fact, we like to use the term of magnetic pressure, which can be expressed as

$$p_m = \frac{B_0^2}{2\mu_0} \quad . \tag{II.6.50}$$

Then in a 10 T field, the magnetic pressure p_m is $\frac{10^2}{2\,4\pi\,10^{-7}} = 40\,MPa = 395\,atm.$

Let's now consider a superconducting dipole and a quadrupole magnet, shown in Fig. II.6.60 and Fig. II.6.61.

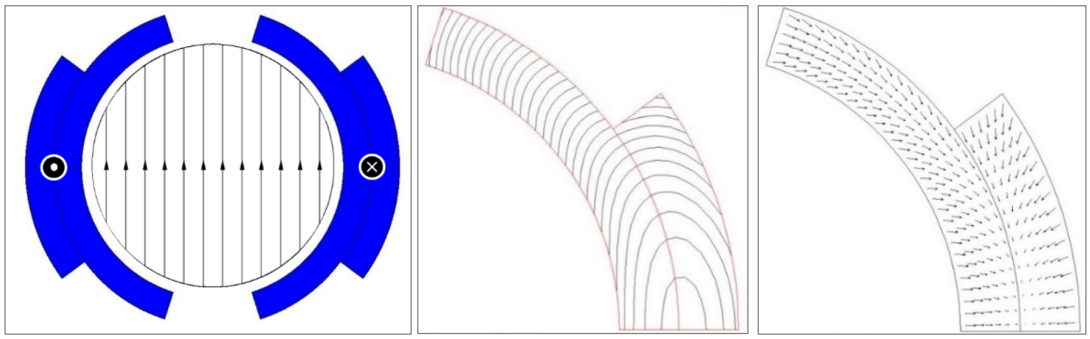

Fig. II.6.60: Schematic view of a dipole coil (left), flux lines on a cross-section of a coil quadrant (centre), and direction of the Lorentz forces (right).

The flux lines in the aperture (left) cross the coil (center) and produce a Lorentz force (right) which tends to push the turns:

- Towards the mid plane in the vertical or azimuthal direction ($F_y,\ F_\theta < 0$);
- Outwards in the horizontal or radial direction ($F_x,\ F_r > 0$).

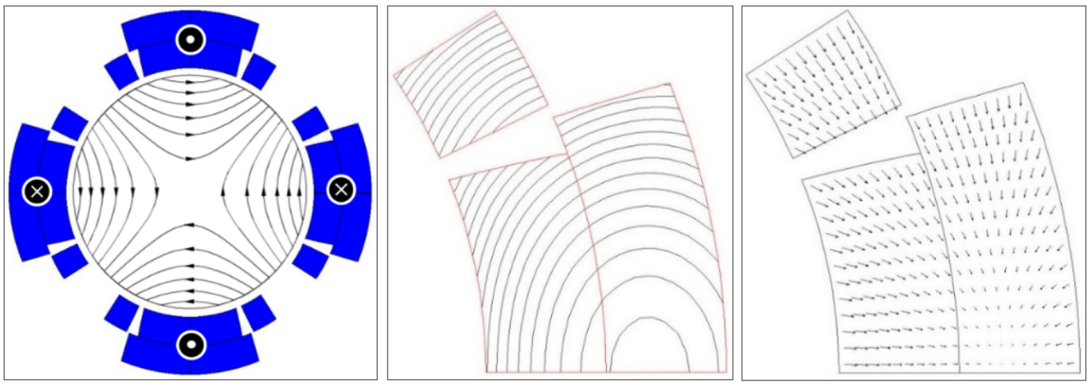

Fig. II.6.61: Schematic view of a quadrupole coil (left), flux lines on a cross-section of a coil octant (center), and direction of the Lorentz forces (right).

At the coil ends, as shown in Fig. II.6.62, the e.m. forces tend to push the coil

– Outwards in the longitudinal direction ($F_z < 0$).

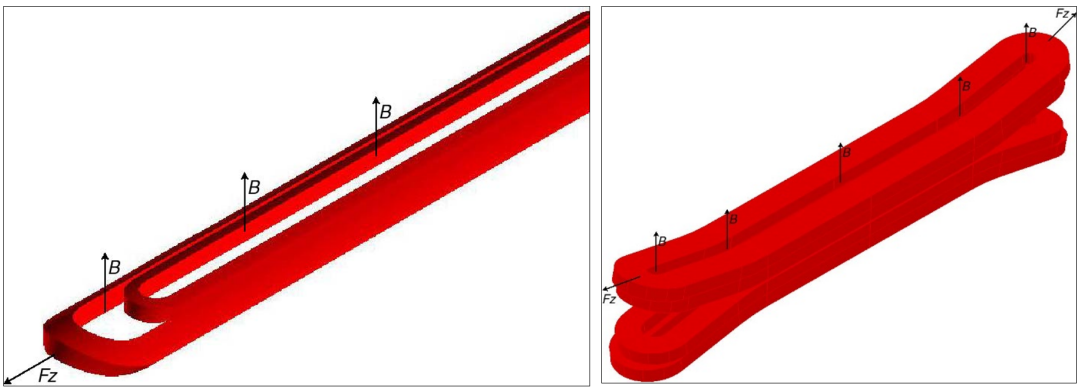

Fig. II.6.62: Direction of the Lorentz forces on the coil ends.

In order to evaluate the main dependencies of the Lorentz forces, let's consider a very simple case (described in [3]) of a coil infinitely thin with a perfect $\cos\theta$ distribution and with an aperture radius r_1. Unlike the case of a thick shell with $\cos\theta$ distribution considered in the previous sections, in the case of the thin shell the current density in express in J/m. For this very simplified coil geometry, the horizontal and vertical e.m. forces [N/m], per quadrant, are

$$\begin{cases} F_x &= \frac{B_0^2}{2\mu_0}\frac{4}{3}r_1 \\ F_y &= -\frac{B_0^2}{2\mu_0}\frac{4}{3}r_1 \end{cases} \quad . \tag{II.6.51}$$

The formulas show how the e.m. force on a dipole coil varies with the square of the bore field and linearly with the bore radius. The axial force, instead, is given by

$$F_z = \frac{B_0^2}{2\mu_0} 2\pi r_1^2 \quad , \tag{II.6.52}$$

and varies with the square of the bore field and with the square of the bore radius.

To give an example, in the Nb-Ti LHC dipole magnets, with a bore field of 8.3 T, in each aperture we have a $F_x = 340$t per meter (considering both coil halves). This means that we need to handle a force comparable to the weight of 300 cars on a meter of a superconducting coil, whose size and position inside the magnet needs to be controlled very accurately because of field quality. Besides still in the LHC dipole, the total force on the coil end (considering the full aperture) is $F_z = 27t$, which is comparable to the weight of the entire magnet cold mass. In the Nb_3Sn magnet HD2, with a bore field of 14 T dipole magnet, the forces are $F_x = 500$t per meter and $F_z = 85$ t. These forces are applied to a coil which is brittle and strain sensitive! These numbers demonstrate how the mechanics of a superconducting magnet is a fundamental aspect of the magnet design, and how a huge effort is dedicated to the design of a support structure that limits the displacement of the turns during excitation and, at the same time, minimizes the stress inside the windings themselves.

If now we consider a 60°sector coil, with inner radius r_1, outer radius r_2, and overall current

density j_o, the forces are given by

$$\begin{cases} F_x &= +\frac{2\mu_0 j_o^2}{\pi}\,\frac{\sqrt{3}}{2}\left[\frac{2\pi-\sqrt{3}}{36}\,r_2^3 \;+\; \frac{\sqrt{3}}{12}\ln(\frac{r_2}{r_1})\,r_1^3 \;+\; \frac{4\pi+\sqrt{3}}{36}\,r_1^3 \;-\; \frac{\pi}{6}\,r_2\,r_1^2\right] \\ F_y &= -\frac{2\mu_0 j_0^2}{\pi}\,\frac{\sqrt{3}}{2}\left[\frac{1}{12}\,r_2^3 \;+\; \frac{1}{4}\ln(\frac{r_1}{r_2})\,r_1^3 \;-\; \frac{1}{12}\,r_1^3\right] \\ F_z &= +\frac{2\mu_0 j_0^2}{\pi}\,\frac{3}{2}\left[\frac{r_2^4}{6} \;-\; \frac{2}{3}\,r_1^3\,r_2 \;+\; \frac{r_1^4}{2}\right] \end{cases} \quad . \tag{II.6.53}$$

In particular in the case of Nb_3Sn coils, extreme attention is devoted to the accumulated stress within the coil due to electromagnetic forces, which can degrade the performance of the superconductor. Most commonly, one of the key parameters carefully monitored, is the stress resulting from the accumulation of e.m. forces on the mid-plane, in the vertical (or azimuthal) direction. Again, in the case of a sector coil, the azimuthal stress on the mid-plane, as a function of the radial position r, can be expressed as

$$\sigma_{\theta_{\text{mid-plane}}} \;=\; -\frac{\mu_0 j_o^2}{\pi}\,\frac{r}{2}\left[(r_2 - r) \;+\; \frac{r^3 \;-\; r_1^3}{3\,r^2}\right] \quad . \tag{II.6.54}$$

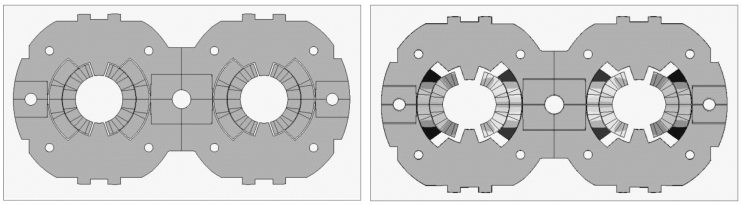

Fig. II.6.63: Difference between a non deformed coil (left) and a coil deformed by e.m. forces in an infinitely rigid structure (with displacements scaling of a factor 100). Darker grey indicates larger displacement.

We conclude this sub-section by pointing out that the e.m. forces given above have the effects of:

1. Deforming, and therefore changing, the coil shape, with a possible detrimental effect on the field quality (see Fig. II.6.63);
2. Displacing and moving the conductors, with a potential release of frictional energy and a consequent increase temperature of the superconductor;
3. Determining the very high stresses that may exist within the windings, which, if in the range of 150-200 MPa, may damage the polyimide insulation in the case of Nb-Ti coils, or cause possible conductor degradation, in the case of Nb_3Sn coils.

In the next sub-sections, we will describe how with the pre-stress, and more in general with the mechanical design of the components surrounding the coil (support structure) we can try to mitigate those risks.

II.6.5.2.2 The concept of pre-stresses

Let's consider the sequence of cross-sections shown in Fig. II.6.64, where the effect of the electromagnetic force on the superconducting coil for the Tevatron main dipole is simulated with a 2D finite element model coil. The coil is represented by two layers which can slide without friction inside an infinitely rigid support structure (collar).

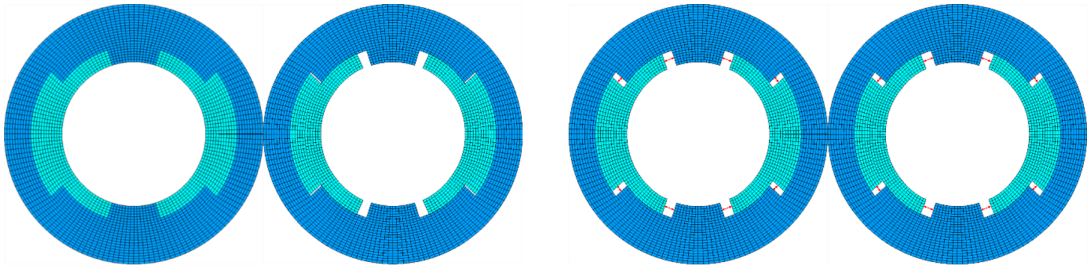

Fig. II.6.64: Deformation of a Tevatron coil in an infinitely rigid structure under the effect of the electromagnetic forces (displacement enhanced by a factor of 50): case without pre-stress (first two pictures from the left) and with pre-stress (third and fourth pictures from the left).

The first image on the left depicts the coil before powering at 0 T, and the second picture from the left the same coil when the Lorentz forces are applied. It can be noticed that, as mentioned earlier, the e.m. forces tend to push the coil towards the mid-plane, therefore opening a gap between the coil and the pole structure, in this the case the collar nose, of about 0.1 mm (for clarity, a displacement scaling of 50 has been applied in the figure). In the case simulated in the two images on the right a shim between the coil and the collar nose has been inserted. The shim pushes the coil towards the mid-plane even before the e.m. forces are applied (third picture form the left). As a result, it can be noticed that, when then the Lorentz forces are applied, the variation of shape is smaller. In other words, the concept of pre-stress consists in pre-loading the coil before the powering occurs, so that the coil is pre-deformed in a similar way as when the e.m. forces are applied, and the additional motion/deformation induced during powering is minimized.

This is presented in a clearer way in Figs. II.6.65 and II.6.66. Let's consider the inner layer of the Tevatron coil, and let's draw a circular path going from the pole to the mid-plane of the dipole (see inset in the figures). On the left figure we find the plot of the azimuthal stress (i.e. perpendicular to the broad face of the coil) along that path and on the right one the azimuthal displacement of the coil due to the nominal field.

We now re-consider the analysis of both cases represented in Fig. II.6.64, without and with pre-stress. If no pre-stress is applied (Fig. II.6.65, referred to the left cross-sections in Fig. II.6.64), the azimuthal stress (left plot) shows zero before powering (0 T), and with the increase of the current to nominal conditions, it reaches -45 MPa on the mid-plane as a result of the accumulation of the azimuthal Lorentz forces. The pole stress is instead basically zero, since no accumulation of azimuthal Lorentz forces takes place. When the displacements are plotted (right figure), no motion is observed before powering, whilst, when the e.m. forces are applied, the coil winding moves towards the mid-plane. The maximum displacement, of about -0.100 mm, is reached by the winding near the pole, again as a result

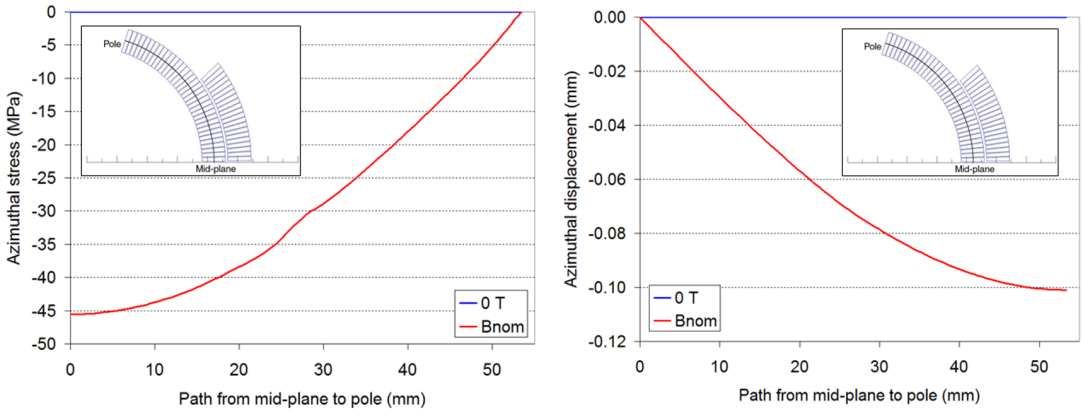

Fig. II.6.65: Azimuthal stress (MPa, left) and azimuthal displacement (mm, right) along a path inside the inner layer of the coil from its middle (on a point on the mid plane of the magnet) to its end for the Tevatron main dipole coil, at 0 T and at nominal field. No pre-stress is applied to the coils. The values are obtained by an ANSYS finite element model with an infinitely rigid collar surrounding the coil.

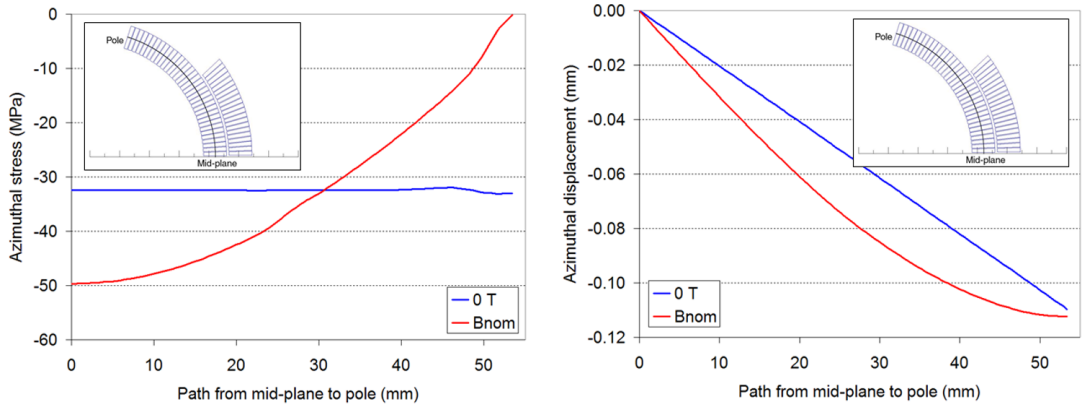

Fig. II.6.66: Azimuthal stress (MPa, left) and azimuthal displacement (mm, right) along a path inside the inner layer of the coil from its middle (on a point on the mid plane of the magnet) to its end for the Tevatron main dipole coil, at 0 T and at nominal field. A pre-stress of -32 MPa is applied to the coils. The values are obtained by an ANSYS finite element model with an infinitely rigid collar surrounding the coil.

of the accumulation of the displacement of all the turns. In other words, the accumulation of the e.m. forces causes a maximum stress on the mid-plane and a maximum displacement on the pole.

Now we repeat the analysis considering an initial pre-stress before powering of about -32 MPa on all the turns, shown by the horizontal "0 T" line in Fig. II.6.66 (left).

In Fig. II.6.66 (right) one can see a displacement which increases linearly from 0 mm on the mid-plane to -0.110 mm on the pole. When the coil is energized, ("B_{nom}" lines), the stress profile becomes similar to the one seen in the no-prestress case during powering (pole unloaded), and the mid-plane with about -50 MPa. A similar observation can be made for the displacement. The key difference lies on the delta between the "0 T" and the "B_{nom}" curves: in the "with pre-stress" case, the maximum motion during excitation is of about -0.020 mm, while in the "without pre-stress" we had -0.100 mm on the

pole.

This simple case shows clearly the key impact of the pre-stress, i.e. the significant reduction of the motion of the turns during powering, when the coil is pre-stressed to a level that maintains minimum azimuthal contact (or pressure) between the pole turn and the collar. It may be interesting to look now at what happens when a fraction of pre-stress is applied. Figure II.6.67 shows the coil azimuthal stress (left) and displacement (right) of the pole windings as a function of the e.m. forces (in percentage of the force at nominal field), with increasing pre-stress levels.

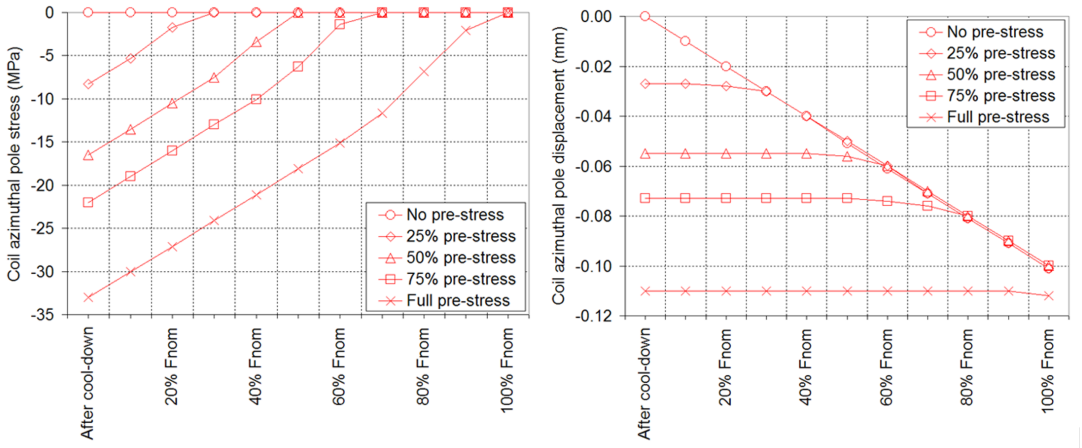

Fig. II.6.67: Azimuthal stress (MPa, left) and azimuthal displacement (mm, right) of the pole turn of the inner layer of the Tevatron main dipole coil, as a function of the e.m. forces (in percentage of the force at nominal field), with increasing pre-stress levels. The values are obtained by an ANSYS finite element model with an infinitely rigid collar surrounding the coil.

The "no pre-stress" case (round markers) and the "full pre-stress" case (cross markers) show the same values (see Fig. II.6.65 and Fig. II.6.66), so with full pre-stress the pole winding unloads but does not move, and without pre-stress the pole winding moves by about -0.100 mm. If instead we applied an intermediate level of pre-stress, we can see that until the winding unloads, no displacement is observed, and only when unload occurs, the pole winding starts moving. The winding unloading is therefore a potentially crucial event, since it defines the moment when significant motion starts showing up in the coil. For this reason, significant effort is devoted to instrumenting the pole area of the coil with strain gauges or fiber optics, with the goal of monitoring the loading conditions of the pole turn during powering.

Finally, we repeat the analysis for all superconducting dipole magnets installed in particle accelerators (considering also the SSC dipole magnet), and we assume again an infinitely rigid structure and a pre-stress level as found in the literature: one can see that, according to data published in literature, pre-stress was applied to all the magnets, at different levels (see Fig. II.6.68), ranging from conditions where the pole remains loaded with significant margin (HERA, SSC, and RHIC) to cases where the pole unloads at nominal (or before), like in LHC or Tevatron.

To conclude, pre-stressing the coil is a technique used to minimize the coil motion, and therefore reduce the frictional energy dissipation and possible field quality distortions during powering. What

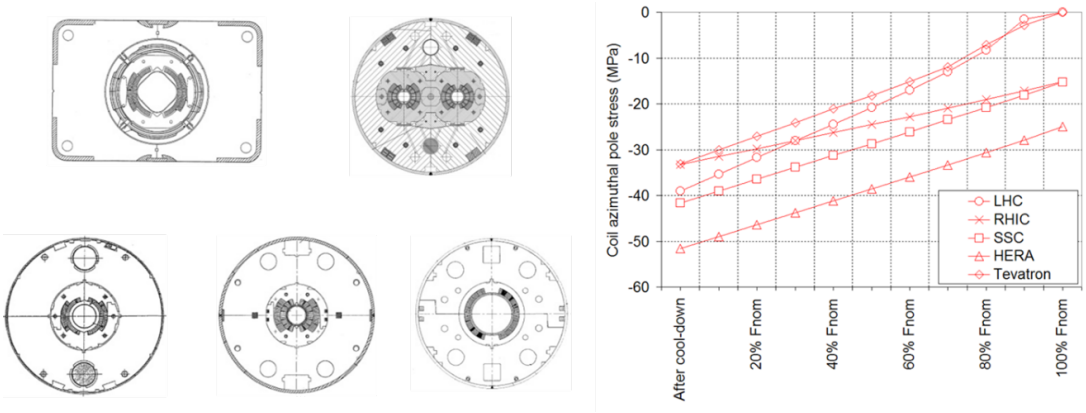

Fig. II.6.68: On the right, pre-stress level of the pole turn and unloading during excitation, for the Tevatron, LHC, RHIC, SSC, and HERA main dipole magnets. The pre-stress values are found in the literature, and the unloading obtained by an ANSYS finite element model with an infinitely rigid collar surrounding the coil. On the left (moving clockwise from the top left) the cross-section of the Tevatron, LHC, RHIC, SSC, and HERA main dipole magnets.

about the effect of pre-stress on quench performance? In principle less motion means less frictional energy dissipation or isolation resin fracture. Nevertheless, the impact of pre-stress on quench initiation remains controversial. Also, current levels corresponding to about 80-90% of I_{ss} were reached in magnets assembled with a wide range of pre-load levels. Therefore, a clear correlation between magnet performance and pre-stress level is extremely challenging to define. However, in a recent test, the MQXFS6 magnet, characterized by a shell-based structure and an impregnated winding pole, showed that also with a low coil pre-stress a current corresponding to about 85% of I_{ss} could be achieved. However, only with a higher pre-load the magnet reached the 95% of I_{ss} level.

II.6.5.3 Support structures

We define as support structure the set of mechanical components surrounding the coils with the specific function of:

1. Minimizing coil motion and deformation during powering;
2. Providing pre-stress;
3. Supporting the windings with a rigid boundary.

At the same time, the components of the support structure contribute to shield the magnetic field and to provide the containment for the liquid Helium necessary for cooling.

Traditionally, the support structure of a superconducting magnet for particle accelerators is characterized by three main components: the collar, the iron yoke and the external shrinking cylinder (or shell). Depending on the role and the importance of each of these three components in the mechanical support of the coil, the support structures are classified in three main groups:

1. Collar-based structures;
2. Yoke-based structures;

3. Shell-based structures.

An additional family of support structure designs is constituted by the so-called stress-management structures, where additional structural components are added to the coil design to reduce the peak stress in the winding due to e.m. forces.

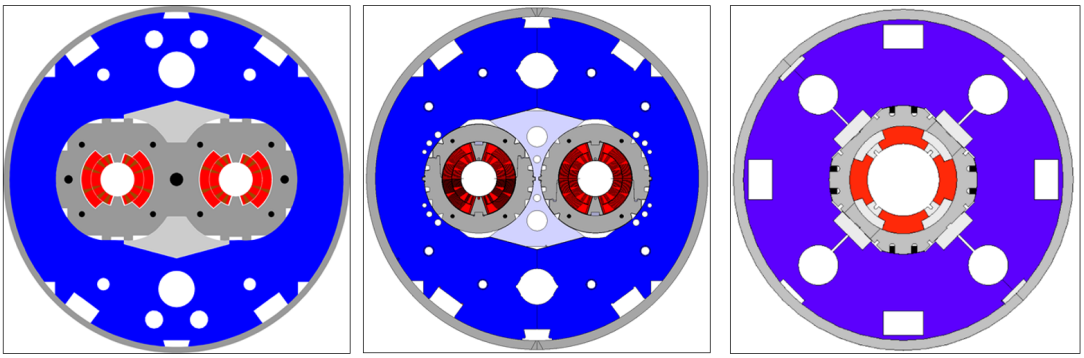

Fig. II.6.69: Example of collar-based structures (not in scale): from left, the CERN LHC main dipole magnet, the CERN 11T dipole magnet, the LARP TQ quadrupole magnet. The three main components are the collars (in grey, around the coil), the iron yoke (in blue around the collars) and the shrinking cylinder (in grey around the yoke).

II.6.5.3.1 Collar-based structures

In order to describe a typical collar structure, we take as a reference the cross-section of the CERN LHC main dipole magnet, the CERN 11T dipole magnet, and the LARP TQ quadrupole magnet, all shown in Fig. II.6.69. The collars, the first components surrounding the coils, were implemented for the first time for the Tevatron main dipole, and since then they have been used in most of the superconducting accelerator dipole and quadrupole magnets. They are composed by thin stainless-steel laminations which are clamped around the coils. The collars laminations (few mm thick) are usually fabricated by stamping, a process that allow keeping very tight tolerances. Therefore, the collars permit to confine the coil inside a very precise cavity, an important aspect for magnets with stringent field quality requirements. The collar cavity is azimuthally smaller than the coil at rest: therefore, when the collars are clamped around the coils and locked with keys, they provide pre-stress to the turns. This process is called collaring procedure (see Fig. II.6.70), and consist in inserting the coil with unlocked collars inside a press. The press then provides enough force to close the collars and allow the insertion of the keys.

In addition to the pre-stress, the collars provide a rigid boundary condition to the coil, i.e. they reduce the horizontal deformations due to the horizontal/radial e.m forces, and in certain designs, they are the only mechanical component of the magnet. In other words, they take care by themselves of the entire mechanical pre-stress and radial support of the coils. In this case we talk about self-supporting collars, a solution adopted in the Tevatron dipoles and in the HERA dipoles. Otherwise, the mechanical support is covered by two additional components: the yoke (in blue in Fig. II.6.69), and the shrinking cylinder or shell (the grey outer shell in Fig. II.6.69).

The yoke, made of iron and composed by thick laminations, has a magnetic function: it contributes

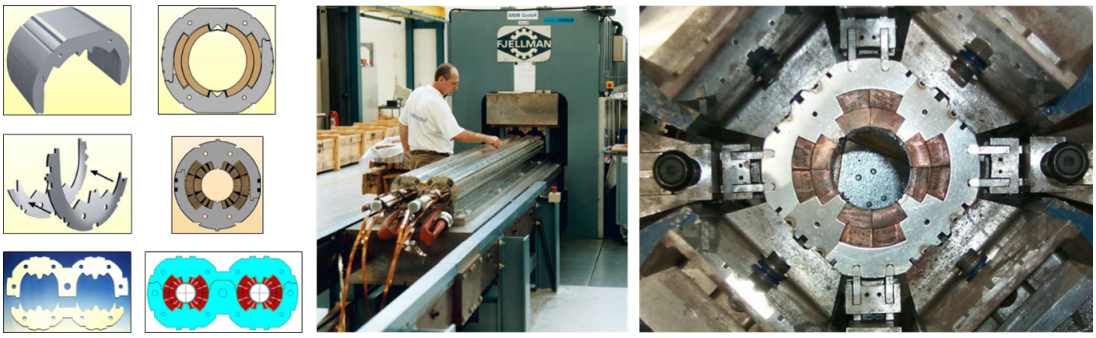

Fig. II.6.70: Left: collars of the Tevatron dipole (top), of the SSC dipole (center) and of the LHC dipole (bottom). Center: collaring process of the LHC main dipole. Right: collaring of the FNAL IR quadrupole magnet.

to both increasing and shielding the magnetic field. It can also play a role on the mechanics, since it can provide additional pre-stress and radial rigidity. The shape of the yoke, and in particular the various holes and slots visible in Fig. II.6.69, are included for magnetic reasons (holes to correct field quality and minimize saturation effects), assembly reasons (holes for tightening rods), cooling reasons (cooling holes), and electrical reasons (slots for bus-bars and current leads).

Similarly to the yoke, the shrinking cylinders, made of stainless steel, have two functions: a mechanical one, since they provide further rigidity and support, and a thermal one, since they constitute the Liquid He containment. When needed, the cylinder is the component that imposes the sagitta to the magnets. For example, for the LHC main dipole magnets, which are 15 m long, the shrinking cylinder set a sagitta of 8 mm: this means the magnet is bent by 8 mm along the length to follow the circular path of the beam.

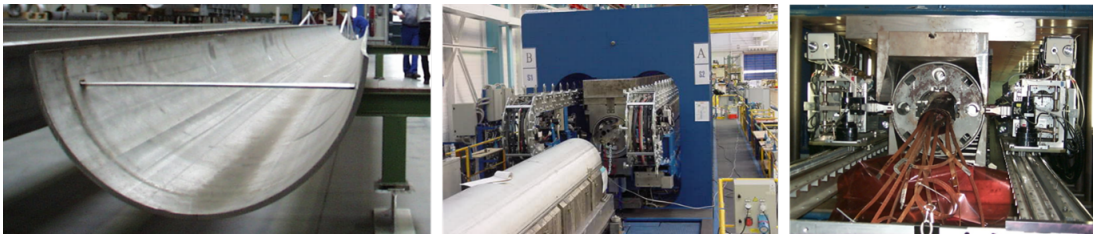

Fig. II.6.71: Left: half shrinking cylinder or shell. Center: shell welding for the LHC main dipole. Right: shell welding for the FNAL IR quadrupole magnet.

Both the yoke and the cylinder are composed by two halves, and they are assembled through the so-called yoking and shell welding procedure (shown in Fig. II.6.71). The procedure consists in assembling the magnet in a configuration rotated by 90°shown in Fig. II.6.69, and by placing in sequence the first half yoke inside the first half shell (see Fig. II.6.71 left), then the collared coil, then the second yoke half and finally the second half shell. This assembly is then placed inside a welding press (see Fig. II.6.71, center and right), which compresses the assembly while the welding is taking place. All the dimensions of the components and the gaps between them are chosen to make sure that after the operation the yoke it is tightly locked around the collars, the gaps between the yoke halves are closed, and the shell is welded

with azimuthal tension. Under this assumption, these kinds of structure provide an extremely rigid configuration. On the other hand, because of the high thermal contraction of the coil compared to all the other components, the collar-based structures with stainless steel collars are generally characterized by a significant loss of pre-load during cool-down.

II.6.5.3.2 Yoke-based structures

A second family of structures is called yoke-based and examples are shown in Fig. II.6.72.

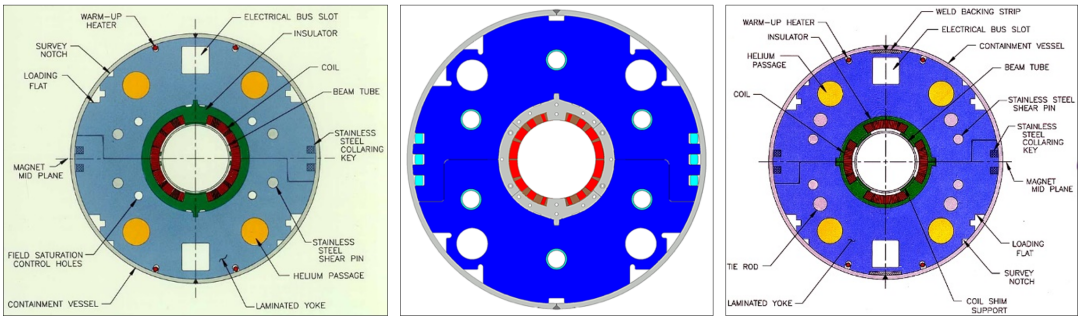

Fig. II.6.72: Example of yoke-based structures (not in scale): from left, the BNL RHIC main dipole magnet, the KEK HL-LHC D1 dipole magnet, and the BNL RHIC arc quadrupole magnet. The three main components are the insulator or collar (in green or grey, around the coil), the iron yoke (in blue around the insulator/collar) and the shrinking cylinder (in grey around the yoke).

With this design, the collars are used as mere spacers, and they are made either by electrical insulating material or by thin stainless-steel laminations. The main rigidity and pre-stress are provided by the yoke laminations, which are locked by keys inserted under a press, in a procedure very similar to the one applied to the collared coil in the collar-based structure. A stainless-steel shell is then welded around the yoke to provide additional rigidity, LHe containment and, if needed, a sagitta. Similarly to the collar-based, the yoke-based structures are extremely rigid, but characterized by a loss during cool-down of a significant part of the pre-load provided during the room temperature operations.

II.6.5.3.3 Shell-based structures

In the shell-based structures, shown in Fig. II.6.73, the external shell is entrusted with the coil pre-stressing and the containment of the Lorentz forces. Collars do not have a pre-load function and can be considered as simple spacers. The yokes are split (azimuthally) in halves for dipole magnets (quadrant for quadrupole magnets) separated by gaps that remain always open, in such a way that no force coming from the shell is intercepted by any components before getting to the coil. The yoke is also split (radially) in two parts: an internal one, usually called pad, and an external one, called yoke. This radial gap allows the insertion of water pressurized bladders, the tool used to pre-tension the shell and pre-load the coil at room temperature. Bladders are composed by two sheets of stainless steel, welded, and connected to a tube which carries the water. Once pressurized water is injected, the bladder expands and delivers the force to the yoke and pads.

The pre-load is obtained by the bladder-and-key operation, whose sequence is shown in

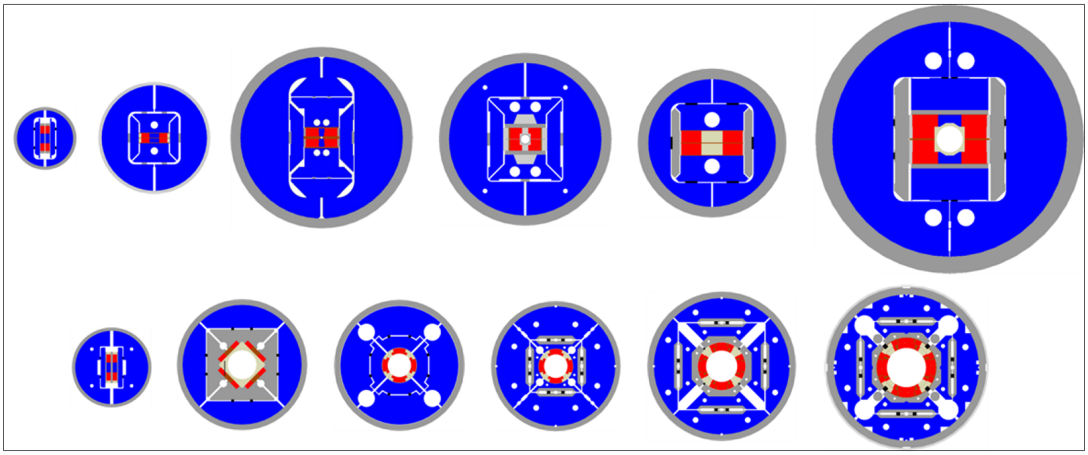

Fig. II.6.73: Examples of collar-based structures, in scale. From top left clock-wise: LABNL SM, CEA SD, LBNL HD1, LBNL HD2, CERN RMC, CERN FRESCA2, HL-LHC MQXF, LARP HQ, LARP LQS, LARP TQS, LARP SQ, LARP LRS.

Fig. II.6.74: the first step consists in the insertion and pressurization of the bladders, which spread apart the pad and yoke, thus pre-tensioning the shell and pre-compressing the coil. Keys are then inserted to lock the displacement, and then bladders are deflated and removed.

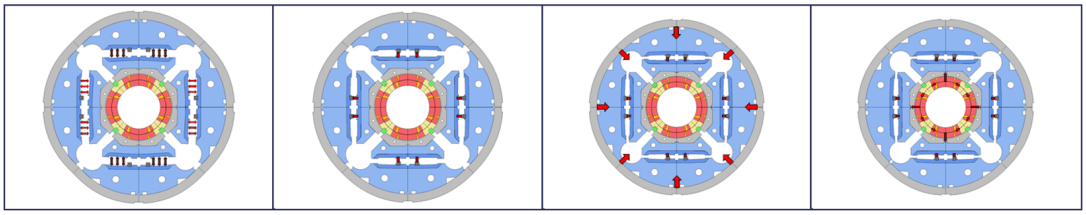

Fig. II.6.74: Pre-loading with bladders, cool-down and powering in MQXF. From left: bladders are inflated; keys are inserted and bladders deflated and removed; cool-down; excitation.

During cool-down, the use of an external shell made of aluminum, a material with high thermal contraction, determines an increase of the force compressing the coil. This force is not intercepted by the yoke or by the pad or by the collar (when present). Then, during powering the coil pole unloads azimuthally and the coil is pushed radially outwards. Compared to collar-based or yoke-based structures, the shell-based structures with open yoke gaps and aluminum shells are characterized by less rigidity, but by the capability of delivering significantly higher compressing force to the coil during cool-down. As long as pre-load is maintained, very little change on shell outer radius during powering, an indication of the structure rigidity, is observed.

II.6.5.3.4 Stress-management structures

In order to reduce the accumulation of Lorentz forces and the consequent excessive stress in the coil which in turn can result in a degradation of the current-carrying capability of the superconductor (for example in brittle and strain sensitive Nb_3Sn), we describe a fourth family of structures, called stress-

management structures, for structural components that are included in the coil design. Three examples are presented in Fig. II.6.75, Fig. II.6.76 and Fig. II.6.77.

In the Canted Cos-theta (CCT) design (see Fig. II.6.75), two superimposed solenoid coils, oppositely skewed (or canted), achieve a pure cosine-theta field conductor distribution and eliminate the axial field. In this design, each turn is contained in a groove and the turns are separated by ribs connected to a spar (or mandrel). The e.m. force on each of the turns is intercepted by the ribs and it is not transmitted to the adjacent one.

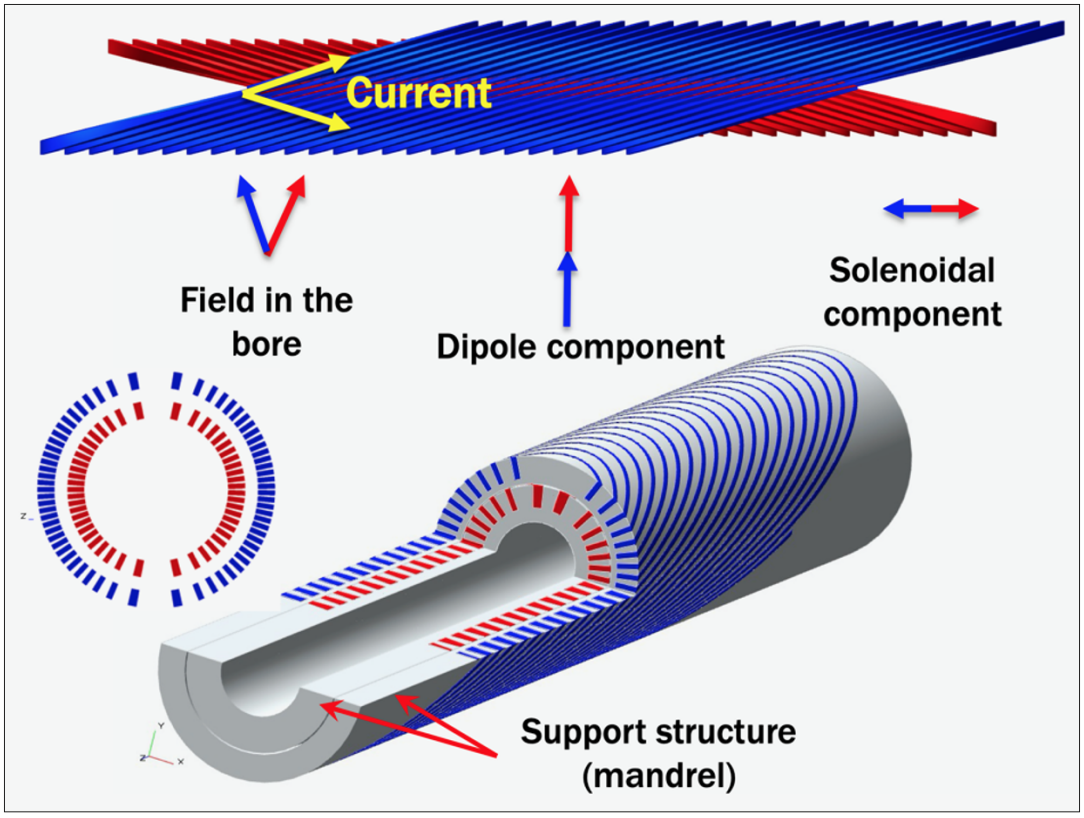

Fig. II.6.75: Canted Cos-theta (CCT) design from LBNL. Left: 2D view of overlapped tilted cables with a solenoid component. Right: cross-section with each turn contained in a grove. Turns are separated by ribs connected to a spar (or mandrel)

A similar approach is used in the Stress-Management Cos-theta (SMCT) design from FNAL (see Fig. II.6.76), but this time the coil design is fundamentally a typical cost-theta design where the blocks (not the turns) are contained in groves.

Therefore, the accumulation of e.m. forces occurs only within each block of conductors, and the blocks are then separated.

The same principle, but applied to a block design, can be seen in the Texas A&M design, shown in Fig. II.6.77.

II.6.5.3.5 Axial support systems

The goal of the axial support system is to minimize:

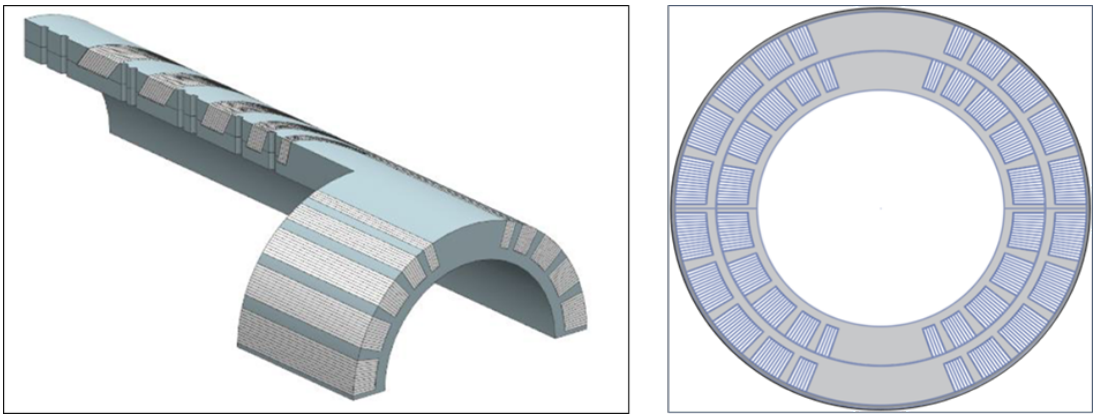

Fig. II.6.76: Stress-Management Cos-theta (SMCT) design from FNAL. Left: 3D view of the coil. Right: cross-section with each conductor block contained in a groove. Blocks are separated by ribs connected to a spar (or mandrel).

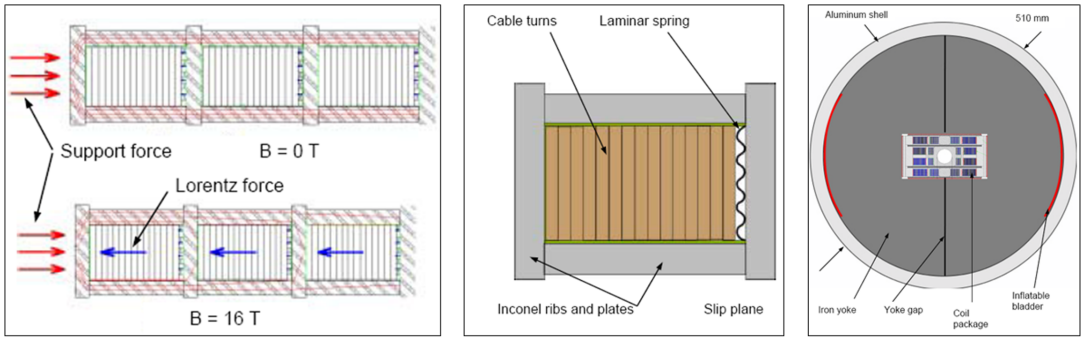

Fig. II.6.77: Stress-Management block design from Texas A&M. Left and centre: details of the conductor blocks separated by plates. Right: cross-section of the magnet.

1. The overall coil motion in the end region due to axial e.m. forces;
2. The pole turn displacement with respect the winding pole and end spacers.

When powering the magnet, the action of the axial e.m. forces is counter-balanced by three elements:

– The coil straight section, with its own axial rigidity,
– The support structure, holding the coil via friction,
– The axial support system.

Regarding this last element, two possible approaches have been adopted so far (see Fig. II.6.78).

In what we call the rigid axial systems, the end plate is bolted or welded to the yoke or to the stainless steel shell, so that its rigidity is provided by the whole support structure. The pre-stress force is delivered to the coil at room temperature via bullets, and after cool-down, (usually, but not always) some loss of pre-load is observed, due to the fact that the coil tends to contracts axially more than the structure. This system is therefore more focused on providing a rigid axial boundary to the coil, and less

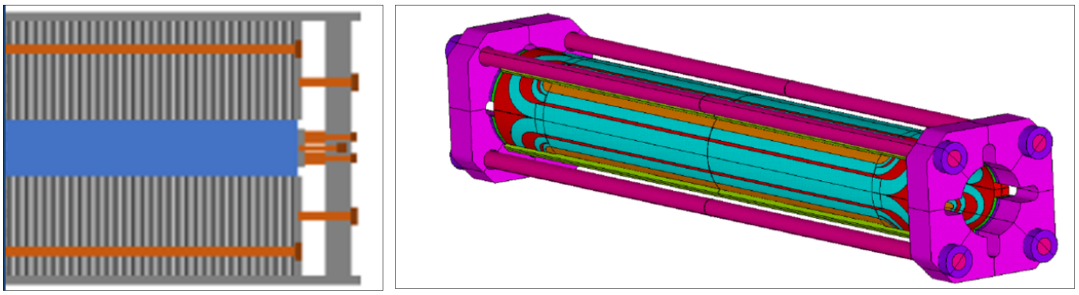

Fig. II.6.78: Example of axial support systems. Left: the coil ends (blue) are supported by an end-plate with bullets. The endplate is welded to the external shell. Right: two end-plates are connected by four aluminium rods.

on pre-loading the turns against the winding pole and end spacers.

In what we can define pre-loading axial systems, full length axial rods (not connected to the structure) are pretensioned to push the end plate against the coil end at room temperature. An increase of rod stress during cool-down is usually measured, and all the force from the rods is transferred to the coil (no interception from the structure). This system is therefore more focused on providing a high pre-load to the coil in order to minimize the relative motion between coil and pole/spacers, while for the rigidity the system relies on the friction coil-to-structure.

II.6.6 Quench, quench protection, and training

In this last section we will focus on the fourth main area related to superconducting magnets. After having dealt with the characteristics of the superconducting materials, the magnetic design, the mechanics and fabrication of superconducting magnets, we will now discuss the phenomena that take place once the magnet is powered, so during magnet excitation. In particular we will describe the *quench* event, and explain how to protect the magnet in case of a quench. Finally, we will describe how the quench behaviour varies with consecutive ramps, in the so-called training process.

II.6.6.1 Quench

A quench is an irreversible transition of a superconducting material from the superconducting state to the normal conducting state. In order to explain the quench phenomenon, let's consider two different scenarios, as described by A. Devred in Ref. [15].

The first scenario, represented schematically in Fig. II.6.79, assumes that the magnet is sitting at a given operating temperature T_{op}.

Considering that magnets are usually immersed in liquid He, T_{op} can be 4.2 K or 1.9 K. Setting the operational temperature is equivalent to cut the three dimensions critical surface of Fig. II.6.79 (left) with a plane at $T = T_{\mathrm{op}}$: the intersection between the plane T_{op} and the critical surface defines the j vs B critical curve (see Fig. II.6.79, right) at that temperature. With the magnet at T_{op}, we can now start injecting current in the coil. The coil will produce a field in the bore, and at the same time it will feel its own field. As explained in Section II.6.3, we can define a line, called load-line, given by the j in

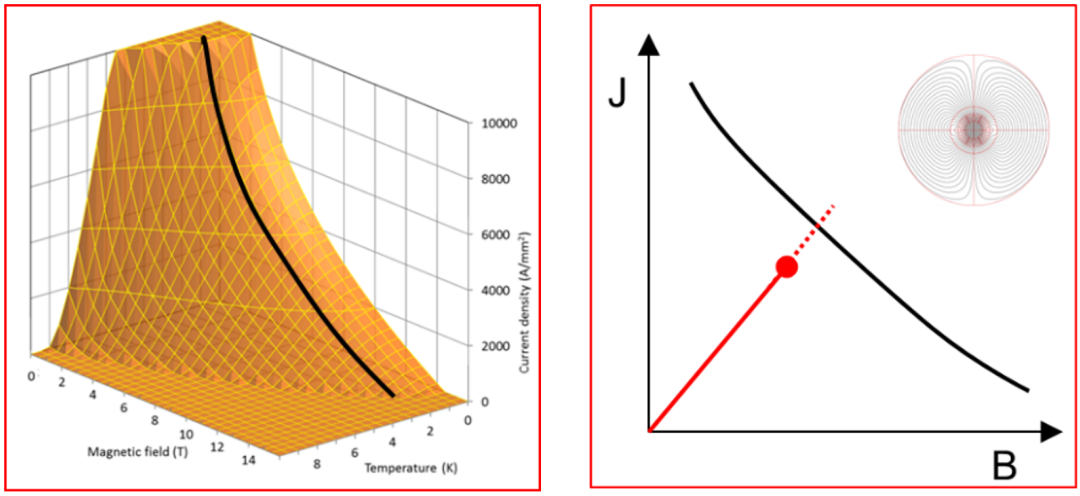

Fig. II.6.79: Left: the superconducting material critical surface, and intersection with the T_{op} plane. Right: resulting J vs B critical curve, and load line.

the superconductor vs. the maximum field B_{peak} in the superconducting coil (see Fig. II.6.79, right). If we stop the increase of the current in the coil to a value below the critical curve (see the red dot on the right Fig. II.6.79), the magnet will still be superconducting. Now let's imagine that, from that point, we continue increasing the current (dashed line) until this crosses the critical curve. At that point, having passed the limit of the superconducting material, we can imagine that a small volume of the coil dV (where the region of the peak field) transitions to the normal state and starts dissipating heat because of the joule effect. The ohmic heat increases the temperature of the volume dV. At the same time, because of diffusion, also the volume surrounding dV (let's call it dV') will see its temperature increasing. If the cooling system is not capable to handle this heat, the volume $dV\prime$ will also transition and starts dissipating heat. The heat will then increase the temperature of dV' and it will diffuse to the surrounding volume . . . and so on. This phenomenon, characterized by the irreversible creation and propagation of a normal conducting zone in a superconductor, is called quench. In the conditions described above and represented in Fig. II.6.79, the quench is caused by the increase of the circulating current beyond the limits of the superconducting material, and it is therefore defined as a *conductor-limited quench*.

A second scenario is shown in Fig. II.6.80. Again, the coil is sitting on a j vs B at the point of the load-line below the critical curve. But now, instead of an increase in current, we have an external disturbance that causes a release of heat reaching the volume dV. Because of the resulting increase of temperature ΔT, the critical curve for the volume dV has now moved (see blue line in Fig. II.6.80, right), and the operational point (red dot) is now located beyond the new critical curve. At this moment the same chain of events, described in the previous scenario, starts, with the volume dV producing ohmic heating and warming up the surrounding volume.

Again, a quench takes place and propagates. This second scenario differs from the previous one since the quench develops because of an increase of local temperature due to a release of energy. Such quenches are therefore called *energy-deposited* or *premature quenches*: the first definition reminds the source of the quench, the second point indicates the early occurrence with respect to the limit of the

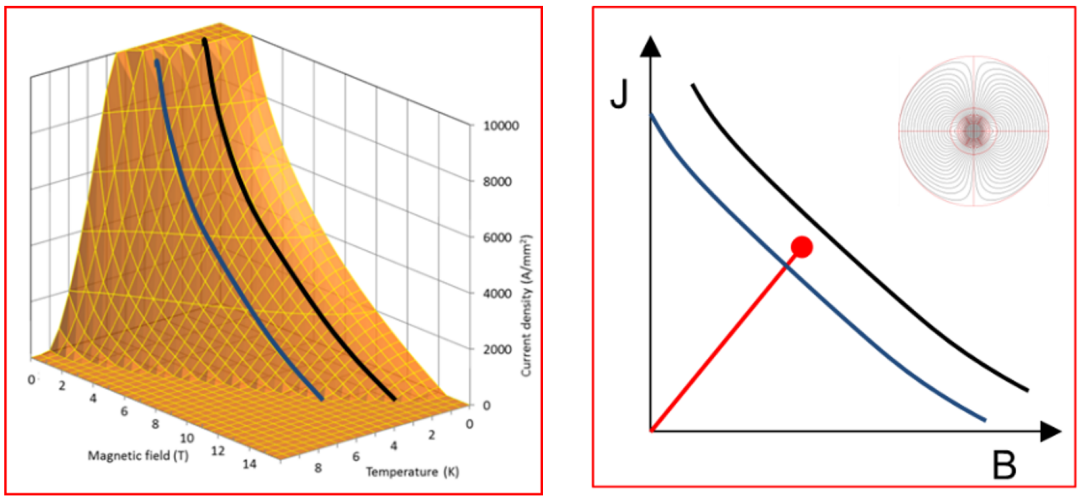

Fig. II.6.80: Left: superconducting material critical surface, and intersection with the T_{op} and $T_{\mathrm{op}} + \Delta T$ planes. On the right the resulting J vs B critical curves, and load-line.

superconductor at the initial T_{op}.

To summarize, one can say that in conductor-limited quenches, critical surface is crossed because of an increase of j (and consequently B, as shown in Fig. II.6.81, left), whilst in energy-deposited or premature quenches the critical surface is crossed because of an increase of T (see Fig. II.6.81, center), being the j (and consequently B) fixed.

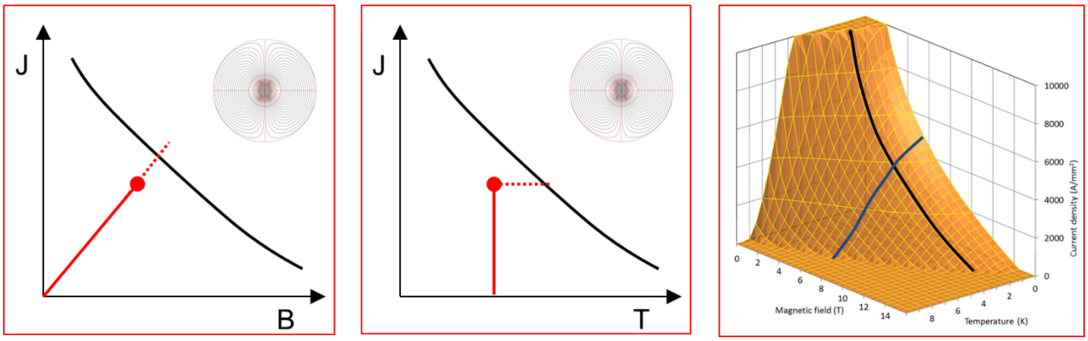

Fig. II.6.81: Left: J vs B critical curves, and load-line. Center: J vs T critical curves, and load-line. Right: previous curves represented on the critical surface.

Clearly, the first type of quenches constitutes an ideal situation for magnet builders, since the quench occurs because of the limit of the conductor is reached. The second type instead is trickier, because it is characterized by the fact that some event occurred and prevented to reach that limit. It is therefore important that we spend more time on the energy-deposited or premature quenches, by identifying the possible causes, or disturbances, that determine those quenches.

As proposed by Wilson [3], we can define a spectrum of disturbances along two dimensions: time and space (see Table II.6.1). Continuous disturbances are due to a steady power dissipation, and can be subdivided in point and distributed disturbances. An example of a point continuous disturbance is for

Table II.6.1: Disturbance spectrum.

		Space	
		Point	Distributed
Time	Transient	J	J/m^3
	Continuous	W	W/ m^3

example a defective splice between two superconducting cables, which, due to high resistance, releases locally and continuously ohmic heating when the magnet is powered. An example of a distributed continuous disturbance could instead be AC losses in a cable due to a not sufficiently short twist pitch: this disturbance would manifest itself as a distributed heating over the entire coil.

II.6.6.2 Stability

Continuous disturbance are generally well understood, avoidable and they normally do not constitute a major issue in superconducting magnet technology (I underline, normally...). Transient disturbances are instead due to a sudden release of energy, again either locally over a small volume (J) or distributed over a large volume (J/m^3). An example of a transient point disturbance is a flux jump, introduced in Section II.6.3, which can be defined as a dissipative redistribution of magnetic field within the superconductor. A way to reduce significantly flux jumps and the energy released is by reducing the filament size.

Another example of transient disturbance is a mechanical event, like a wire/cable/coil frictional motion under the action of the electro-magnetic forces, or a crack in the epoxy. A possible remedy towards wire motion was mentioned in the previous section, where we explained how a pre-stress of a coil can reduce the overall displacement during powering, and therefore minimize the frictional energy release. Regarding epoxy cracking, a solution adopted during magnet fabrication is to fill the epoxy with fiberglass, thus significantly improving its mechanical strength. However, in general transient disturbances are much less predictable and difficult to avoid, since they are linked to the overall mechanical design of the magnets, and they are related to both the mechanical design of the magnet and to the quality of the magnet fabrication.

In order to reduce the occurrence of a quench, acting on the source of disturbance (motion, cracks, etc.) is only one of the possible strategies. In reality, one has to act on multiple fronts. These fronts are the different terms of a heat equation along a superconducting wire, that is

$$C\,\frac{dT}{dt} \;=\; \frac{I^2 R}{A} \;+\; Q_{\mathrm{ini}} \;+\; \frac{d}{dx}\left(k\,\frac{dT}{dx}\right) \;-\; H\,\frac{P}{A} \quad , \tag{II.6.55}$$

where x is distance along the wire, k is the thermal conductivity along the wire, T is temperature, I the current, R is the effective resistance, A the cross section area, Q_{ini} is the initiating energy pulse (W/m^3), H the heat transfer rate to the liquid helium (W/m^2), P the wetted perimeter, and C is specific heat per unit volume.

The equation describes how the increase of temperature of a superconductor is linked to the heat coming from the disturbance, the ohmic heat generated once the transition to normal conductivity occurs,

the heat removed by conduction along the wire and by the cooling liquid.

More in general, the equation describes the concept of *stability* of a superconductor, i.e. the capability of a superconductor, and of the cooling system, to withstand a thermal input. In the previous subsection we introduce the disturbances (Q_{ini}) which produce ohmic heating ($\frac{I^2 R}{A}$). It is important to spend now some time on the conduction part, and in particular on the importance of the stabilizer.

Let's imagine that, in a coil operating in the superconducting state, a certain amount of energy E is released. This energy will bring a volume V of the superconductor to a temperature $T \geq T_c$. One can imagine that if E or V are not large enough, the temperature of the superconductor will decrease to below the critical temperature, because of cooling and or thermal conductivity. If, on the contrary, E or V are large enough, the normal zone will increase and a quench propagates. We therefore can define:

- A *minimum quench energy* MQE, the minimum energy necessary to initiate a quench;
- A *minimum propagation zone* MPZ, the minimum volume of superconductor that must be brought beyond the critical temperature in order to initiate a quench.

The two parameters are connected: MQE is the energy necessary to created an MPZ.

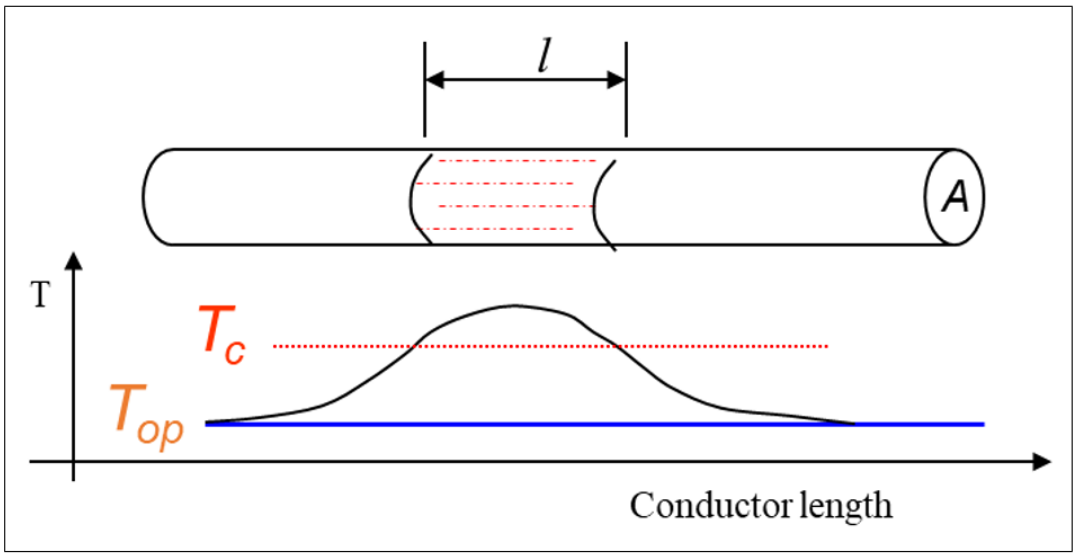

Fig. II.6.82: Top: superconducting wire with a zone of length l above the critical temperature T_c. Below: temperature profile, where T_{op} is the operational temperature.

To show the importance of the stabilizer let's compute the MPZ and MQE for a pure superconducting wire, as shown in Fig. II.6.82, and as described in Ref. [3]. Let's assume that a certain amount of energy E increased the temperature of the superconductor beyond T_c over a length l. The segment l of superconductor is dissipating power given by $j_c^2\, \rho\, A\, l$ [W]. Let's assume that heat is removed only by conduction, so no cooling is provided by LHe, and that we have a stable condition where all the heat is conducted out of the segment because of the thermal gradient, which can be approximated as $(T_c - T_{op})/l$. Therefore, being k the conductivity [W m_1 K_1], when the power dissipated equals the

power conducted away we have

$$\frac{2\,k\,A\,(T_c\,-T_{\rm op})}{l}\;=\;J_c^2\,\rho\,A\,l\quad\;, \tag{II.6.56}$$

which results in

$$l\;=\;\sqrt{\frac{2k\,(T_c\,-\,T_{\rm op})}{J_c^2\,\rho}}\quad. \tag{II.6.57}$$

Under these simplified assumptions, the length l defines the MPZ (and MQE), so a normal zone longer than l will keep growing (quench). A normal zone shorter than l will collapse. For a typical Nb-Ti 6 T magnet, the following quantities can be used

$$\begin{cases} j_c & = 2\,10^9\,Am^{-2} \\ \rho & = 6.5\,10^7\,\Omega m \\ k & = 0.1\,Wm^{-1}K^{-1} \\ T_c & = 6.5\,K \\ T_{\rm op} & = 4.2\,K \end{cases}\quad. \tag{II.6.58}$$

In this case, $l = 0.5$ µm and, assuming a 0.3 mm diameter, the required energy to bring to T_c is 10^{-9} J. A wire made purely of superconductor, without any stabilizer (like copper) around, would quench with nJ of energy!

Since we clearly do not want to reduce j_c, the most effective way to increase l, is to increase $\frac{k}{\rho}$. We now consider the situation where the superconductor is surrounded by material with low resistivity and high conductivity. Copper can have at 4.2 K a resistivity $\rho = 3\,10^{-10}$ Ωm (instead of $6.5\,10^{-7}\Omega$m for Nb-Ti), $k = 350\,W\mathrm{m}^{-1}\mathrm{K}^{-1}$ (instead of $0.1\,W\mathrm{m}^{-1}\mathrm{K}^{-1}$ for Nb-Ti). We can therefore increase k/ρ by a factor of almost 10^7. The use of a stabilizer surrounding the superconducting filament can bring the MQE from the nJ level to the 10-100 µJ level, and the MPZ from the µm to the mm level, see Ref. [16].

II.6.6.3 Quench protection

Eliminating quenches is one of the goals that guide a magnet designer during the full development of a magnet. However, one has to accept the idea that magnets quench, or at least that magnets may quench. Therefore, after discussing about the definition of quench, and the causes of quench, and the mitigation of a risk of quenches, we describe here the system that we put in place to protect a magnet after the occurrence of a quench. The topic of *quench protection* is among the most important within superconducting magnet technology, since it deals with the following mandatory requirement: a magnet has to survive a quench without any damage.

As explained in the previous section, during a quench, ohmic heating increases the temperature of the superconducting material and propagates within the coil, as shown in Fig. II.6.83.

The location where the quench originates is the one that during the process sees the highest temperature increase, since it is the region where the heat is released since the beginning. In particular the protection system is designed to avoid that the region, which is called the *hot spot*, the temperature does

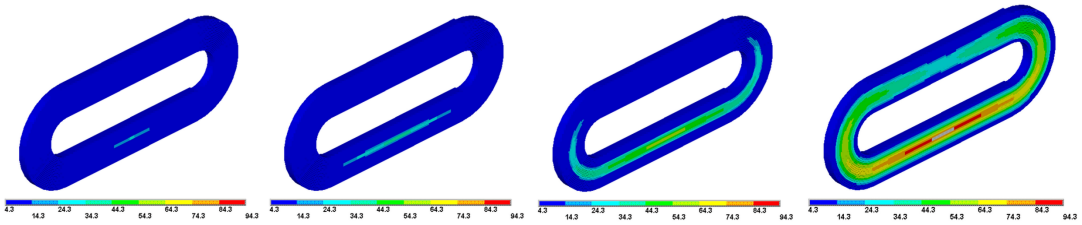

Fig. II.6.83: Propagation of a quench, with a final hot spot temperature of 95 K.

not reach excessive levels and cause damages to the coil.

The analysis of the actions required to define the quench protection scheme starts from the heat equation II.6.55 that describes the evolution of the temperature as a function of the different heating and cooling elements. Let's make the adiabatic assumption that all the heating coming from the I_R^2 term (and neglecting the heat coming from the disturbance) contributes to the increase of temperatures, without any conduction or heat transfer to the LHe. This approach is conservative, but it is often made in preliminary quench protection analysis, considering the risks of causing a permanent damage to the coil because of high temperatures. Therefore

$$C\frac{dT}{dt} = \rho\, j^2 \quad , \tag{II.6.59}$$

which can be rewritten and integrated as

$$\int_{T_{\rm op}}^{T_{\rm max}} \frac{C}{\rho}\, dT = \int_0^{t_{\rm max}} j^2\, dt \quad , \tag{II.6.60}$$

or as

$$\int_0^{t_{\rm max}} [I(t)]^2\, dt = \nu\, A^2 \int_{T_0}^{T_{\rm max}} \frac{C_p^{\rm ave}(T)}{\rho_{\rm Cu}(T)}\, dT \quad , \tag{II.6.61}$$

where I is the magnet current, ν the copper fraction in the cable, A the cable cross-sectional area, $C_p^{\rm ave}$ the volumetric specific heat of the insulated cable and $\rho_{\rm Cu}$ the copper resistivity and where t = 0 corresponds to time of the quench start. From this equation one can see that in order to limit the maximum temperature $T_{\rm max}$ as for example at 300 K one has to act on the current, and minimize the integral over time of the current (square) that runs in the coil after a quench starts (at t = 0). This integral expresses the current, voltage and temperature during quench in MIIT (or better, plural MIITs), where the name comes from 10^6 ("M" like Mega), $[A]^2$ ("II" like Amperes square), [s] ("T" like Time). The maximum number of MIITs can be calculated in order to keep $T < T_{\rm max}$ for each magnet.

In order to reduce the MIITs, the current needs to drop as fast as possible once the quench is detected. The decrease of the current can be estimated by considering the magnet, characterized by its inductance L, as an L/R circuit (see Fig. II.6.84).

During normal operation, the magnet resistance R is zero, and the current flows from the power supply to the coils. Once a quench is detected, a switch separates the power supply from the circuit, and thanks to a diode D the current flows inside the magnet while the resistance, given by the normal conducting portion of the quenched coil, is increasing.

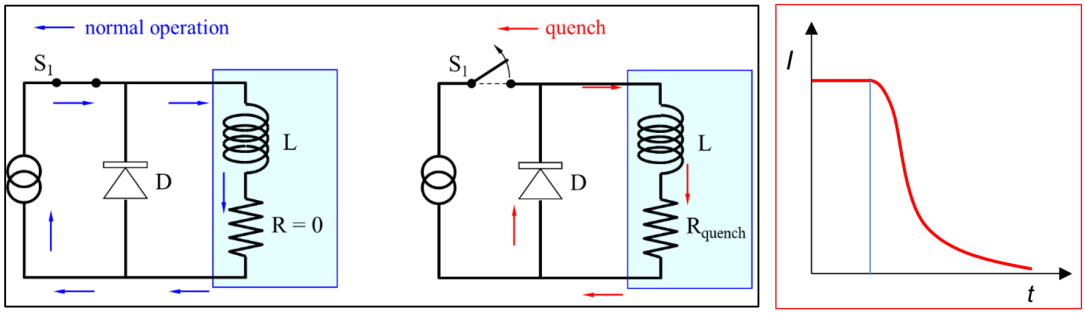

Fig. II.6.84: Representation of a magnet circuit as L/R circuit during normal operation (left) and after a quench (center), from S. Izquierdo Bermudez. The right plot shows an example of current decay after a quench.

The decay of the current in a L/R circuit, can be expressed as

$$I = I_0 \, e^{\left(-t \frac{R(t)}{L}\right)} \quad . \tag{II.6.62}$$

Therefore, it is clear that one has to maximize R to quickly bring to zero the current in the magnet. And, rather than waiting for the quench to propagate in the entire coil, this can be achieved by making resistive the entire coil as fast as possible via the use of *quench heaters*.

Quench heaters (see Fig. II.6.85) are composed by stainless steel strips glued on a polyimide foil. The foil is positioned on top of the coils. Once the quench is detected, the quench heaters are fired, i.e. current is injected in the stainless-steel strips. As a result, the ohmic heating produced by the quench heater is transferred to the coil. In this way, the entire coil quenches, and the coil resistance maximized.

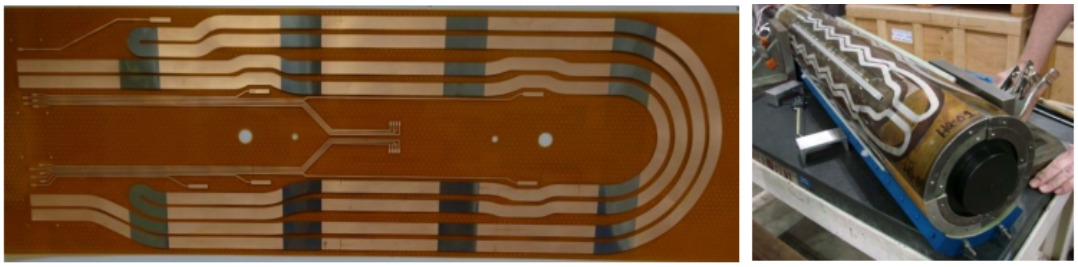

Fig. II.6.85: Quench heaters (left) and a coil with a quench heater after impregnation (right).

Ironically, one can notice that magnet builders devote tremendous effort to avoid a quench, but when a quench occurs, it seems counter-intuitive, one has to put the same effort to quench the entire coil.

A typical profile of the current decay is shown in Fig. II.6.84 (right). If we assume that the quench occurs at t=0, we notice that before the current starts decaying one has to detect the quench, activate the switch, fire the heaters, wait for the heat to propagate to the coils and finally quench them. Only at that point the resistance becomes significant and the current drops. All these must be achieved while keeping the MIITs to a level such that the hot spot remains below 300 K. For the Nb-Ti magnets of the LHC, the quench of the whole coil must happen within 100 ms of the quench onset, for the HL-LHC Nb_3Sn

magnet 30 ms [11].

II.6.6.4 Training

After defining the quench, describing its causes and presenting the system put in place to protect a magnet, we can ask ourselves: what happen when, after a quench, we power again the magnet? The most common answer to this is: the magnet will start training. A nice definition of training can be found in the abstract of a 1978 paper from Brechna *et al.* [17], which states:

"In the early 70's interest was centered upon a new phenomenon observed at CERN in two racetrack shaped epoxy impregnated coils. While energized for the first time, they quenched at about 30% of the measured short sample current value. After numerous runs finally the design values were reached. Interesting enough many laboratories reported shortly afterwards a similar trend in racetrack coils and even in solenoids. The phenomenon, that after each successive quench the transport current could be raised by some fraction yielding an improved performance of the conductor until design, or short sample value is reached, was termed training."

Training is therefore characterized by two separate phenomena:

1. The occurrence of premature quenches;
2. The progressive increase of quench current, ramp after ramp.

These two combined phenomena are extremely interesting and fascinating. One could say that they are related to something not reversible happening inside the magnet, or, in other words, to an irreversible change in the coil's mechanical status occurring after a quench, with the result that the magnet is somehow "improving" or "getting better" quench after quench. Mechanically induced premature quenches are generally considered the main causes of training in superconducting magnets. In particular two are the main events associated to training:

- Frictional motion of a superconductor;
- Epoxy failure (or cracking), in the case of epoxy impregnated coils.

II.6.6.4.1 Frictional motion

As mentioned in the previous section, among the different disturbances that may trigger a quench, one of the most relevant is the conductor movement induced by electromagnetic forces: during excitation, in a frictional environment any motion produces heat. And heat, if larger than the MQE, can trigger a quench.

For what concerns the progressive increase of quench current after successive ramps, intuitively one could imagine that, after each quench, the coil remains partially locked by friction in a new and more secure state which allows the conductors to withstand higher levels of Lorentz forces. To explain training with frictional motion, we refer to the Coulomb friction model (or static friction model). Consider a body on a rigid surface, being N the normal force (in this case vertical) exerted between the body and the rigid surface (see Fig. II.6.86, left).

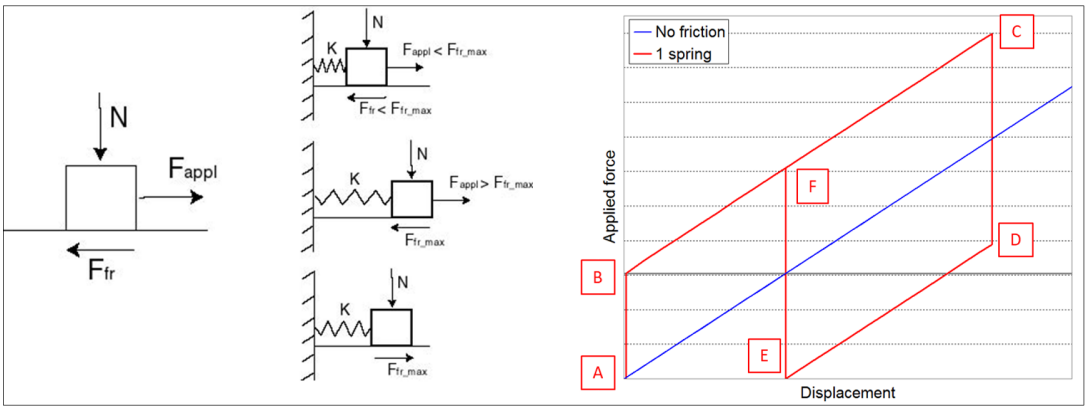

Fig. II.6.86: (Left) Coulomb friction model: body with vertical force under the action of frictional force and applied force. (Center and left) body connected to a spring and pulled by an horizontal force. Schematic view of the model and plot with applied force vs displacement. The applied force is increased from A to C, decreased from C to E, and increased again from E to C.

We then apply to the body a force F_{appl} parallel to the contact surface. The friction force is given by $F_{\mathrm{fr}} \leq \mu \mathrm{N}$ where μ is the friction factor. This means that the friction force depends on F_{appl}. If $F_{\mathrm{fr}} \leq \mu \mathrm{N}$, no sliding occurs, i.e. the friction force is what is needed to prevent motion. If $F_{\mathrm{appl}} > \mu \mathrm{N}$, sliding occurs, and the friction force is constant and equal to $\mu \mathrm{N}$.

Alternatively, we can use a contact pressure P instead of a force N, and a frictional stress or shear stress σ_{fr} instead of F_{fr}. The Coulomb model can be reformulated as follows: two surfaces can carry shear stresses σ_{fr} up to a magnitude μP across their interface before they start sliding relative to each other. Whenever two surfaces slide with respect to each other in a frictional environment, frictional energy is dissipated. The frictional energy dissipated per unit area E (J/m^2) can be estimated as $E = \delta\, C$, where δ (m) is the relative sliding of the two surfaces, and C (N/m^2) is the frictional stress between the two surfaces (in the direction parallel to the surface). Now, some orders of magnitude: let's consider a contact pressure between coil and support structure (or between adjacent cables) P of about 30 MPa. With a friction factor $\mu = 0.3$, the maximum frictional stress will be

$$\sigma_{\mathrm{fr}} \;=\; \mu P = 9\ \mathrm{MPa} \quad .$$

A relative sliding δ of about 1 µm will dissipate

$$E \;=\; \sigma_{\mathrm{fr}}\, \delta \sim\; 10\ \mu\mathrm{J/mm}^2 \quad .$$

Note that 10 µJ was the computed MQE for the SSC dipole: so, a very small motion under friction can initiate a quench.

This analysis aimed to demonstrate that frictional motion can create enough energy to cause a quench, but how can we explain the progressive increase of quench current? An interesting model was proposed by Iwasa [18], and it is presented in a schematic way in Fig. II.6.86, center.

Let's consider again a body pushed by a force N against a rigid surface, but also connected by a

spring to a second perpendicular rigid surface. When a force F_{appl} perpendicular to the N force is applied, the displacement can be plotted as in Fig. II.6.86, right. The body does not move until the applied force is larger than the friction force (A to B). Once the applied force becomes larger than the frictional force, the body moves to C with an increasing applied force. If the applied force is now reduced, the body does not move (C to D) until the force from the spring becomes higher than the applied force and the frictional force (which at that point changes sign). The body will stop in E, where the spring force matches the frictional force. If the process is repeated, the body will follow now a different path (E to F to C). This simple model demonstrates that:

1. At the end of the first cycle, an irreversible displacement is present, i.e. the body finds itself in a new position;
2. During the second cycle, for the same increase of applied force, the total displacement (C-F) is smaller than in the first cycle (C-B).

In other words, friction lock the system in a new state and during the second ramp, the overall displacement (and so the total frictional energy dissipation) reduces.

This irreversible behaviour can be actually measured with strain gauges. An example was the LARP racetrack quadrupole magnet SQ (see Fig. II.6.87).

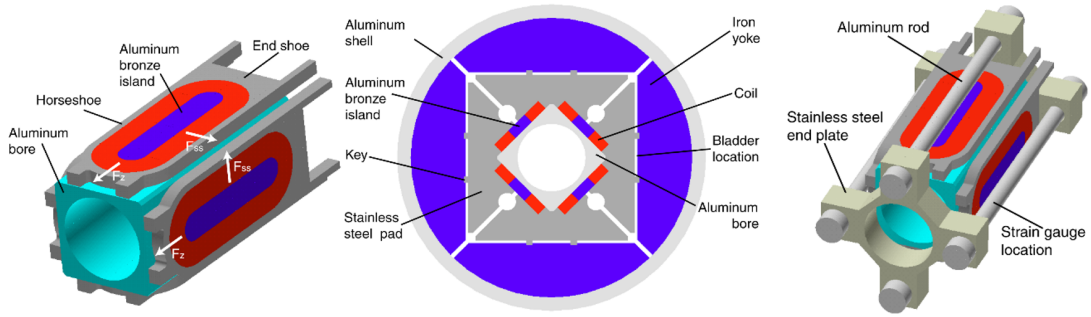

Fig. II.6.87: Left: SQ02 coil configuration and Lorentz force directions. Centre: magnet cross-section. Left: axial support.

The axial aluminum rods were instrumented with strain gauges. Since the rods were in direct contact with the coil ends (via end plates), any coil axial displacement induced by the z component of the electromagnetic forces resulted in a change in rod strain. During the first 13 quenches, when most of the magnet training occurred, the rod strain showed a progressive and continuous change of coil length. In Fig. II.6.88, the incremental increase in rod strain (and coil length) is plotted as a function of the fraction of Lorentz force with respect to the 4.3 K short sample value $(\frac{I}{I_{\text{ss}}})^2$.

The strain referred to in the plot is the difference between the final length l_{final} and the initial length l_{initial} , divided by the initial length, i.e. $(l_{\text{final}} - l_{\text{initial}}) \,/\, l_{\text{initial}}$. The strain value is then multiplied by 10^6 and expressed in "µstrains".

As explained in the previous sections, the axial component of the Lorentz force tends to pull the coil-end outwardly. As a result, the coils, as well as the rods, are elongated along the z direction. During the first current ramp, prior to the first quench, the rod stretched to a strain of $15 \cdot 10^6$, or 15 µstrain (see

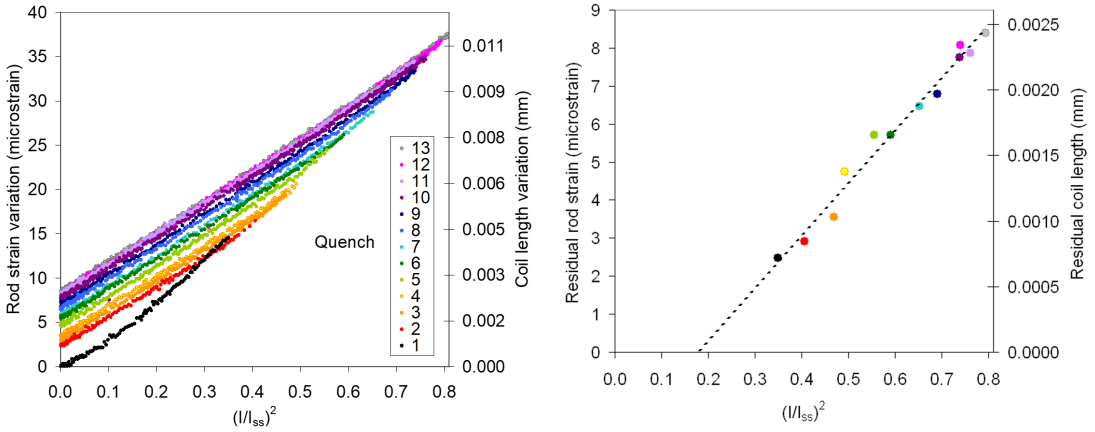

Fig. II.6.88: Left: measured variation of rod strain (left axis) and coil length (right axis) as a function of the fraction of Lorentz force with respect to the 4.3 K short sample value. The first 13 ramps of training are shown. Right: rod strain measured residual (left axis) and coil elongation (right axis) as a function of the fraction of Lorentz force with respect to the 4.3 K short sample value reached during an excitation cycle. The strain referred to in the plot is the difference between the final rod length l_{final} and the initial rod length l_{initial} , divided by the initial length, i.e. $(l_{\text{final}} - l_{\text{initial}}) / l_{\text{initial}}$. The strain value is then multiplied by 10^6 and expressed in "µstrain".

left plot of Fig. II.6.88), indicating that the coil underwent a total elongation of about 4 µm. After the quench, when the current decreased to zero and the Lorentz force vanished, the rods maintained a residual strain (about 3 µstrain), showing that the coil remained partially elongated. During subsequent training ramps, as the quench current reached higher levels, the total residual strain increased as well, indicating that the larger the force, the greater the coil lengthening (Fig. II.6.88, right). This phenomenon, called ratcheting, had been observed in previous magnets, and can be related to the friction between the coil and its surrounding components. After each excitation ramp, friction partially locks the coil in a new deformed state, preventing the conductor from returning to its original state.

II.6.6.4.2 Epoxy failure

Epoxy failure is a second possible phenomenon that can explain magnet training. Epoxy resin, which is typically used in Nb_3Sn magnets to protect the brittle strands after the heat treatments, becomes itself brittle at very low temperatures. In addition, epoxy has a higher thermal contraction than the composite superconductor (to which it is glued). This means that, after cool-down, the epoxy, which is bonded to the copper of the strands and to the coil parts (winding pole, end spacers), is in tension. When a brittle material is in tension, micro-cracking or micro-fractures may occur. A material under stress/strain stores a strain energy density [J/m^3] given by (uniaxial case)

$$Q = \frac{1}{2}\frac{\sigma^2}{E} = \frac{E\,\epsilon^2}{2} \quad . \tag{II.6.63}$$

When a crack propagates, the strain energy previously stored in the volume surrounding the crack is converted in heat. And this heat can trigger a quench. Again, but what about the progressive increase of current? We refer here again to the work from Iwasa and to his analysis of acoustic emission (AE) in

Ref. [18]. In fact, any crack of epoxy may generate "noise" which can be detected and recorded. During successive ramps of a training magnet, AE showed a very peculiar effect, which is known as "Kaiser effect".

As Iwasa states [18]: *"the Kaiser effect describes mechanical behavior observed during a sequence of cyclic loading in which mechanical disturbances such as conductor motion and epoxy fracture appear only when the loading responsible for disturbances exceeds the maximum level achieved in the previous loading sequence. When an epoxy-impregnated magnet is energized for the first time, epoxy fracture occurs soon after the Lorentz stress in the winding exceeds the epoxy's local fracture stress. As the current is increased, the Lorentz stress continues to rise and epoxy cracking persists. At a current level Ft1, the charging is stopped and current is slowly brought back to zero. During the second charging sequence, epoxy fracture does not appear for currents between 0 and Ft1; it only begins to appear when current is raised above Ft2. The trend continues in subsequent charging sequences"*(see Fig. II.6.89).

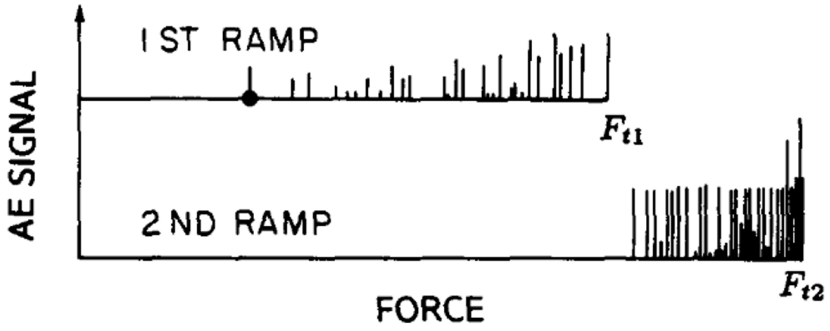

Fig. II.6.89: Kaiser effect: acoustic emission recorded during two consecutive current ramps: during the second charging sequence, epoxy fracture does not appear for currents between 0 and F_{t1}; it only begins to appear when current is raised above F_{t2} (from [18]).

II.6.6.4.3 Examples of training

To conclude the discussion on training, we show here four examples of quench performance which can be considered representative of typical magnet trainings. Figure II.6.90 shows in the top left panel the training of the Nb_3Sn quadrupole magnet MQXFS01.

At 1.9 K, the magnet had a first quench at 14.2 kA, corresponding to 66% of the short sample current I_{ss} at 1.9 K of 21.5 kA. Then, after six quenches, it exceeds the nominal current of 16.23 kA, the current at which the magnet is supposed to operate in nominal conditions (7 TeV) once installed in the LHC accelerator. In 13 quenches the magnet reached a current value corresponding to the ultimate operational condition of the LHC accelerator (7.5 TeV). Once it passed 18 kA, the temperature was increased to 4.5 K, and the magnet quenched at the same current, showing a significant temperature margin. After the thermal cycle (i.e. the magnet was warmed up to room temperature and cooled down again at 1.9 K), the first quench was at 18.2 kA, so higher than the last quench before the thermal cycle. In this case the magnet remembered the training, so it exhibited "perfect memory". Memory is an extremely important aspect of a magnet performance. A magnet with perfect memory can in fact be tested, prior to the installation in the accelerator, in a test facility, where it can be trained up to the current at which it is

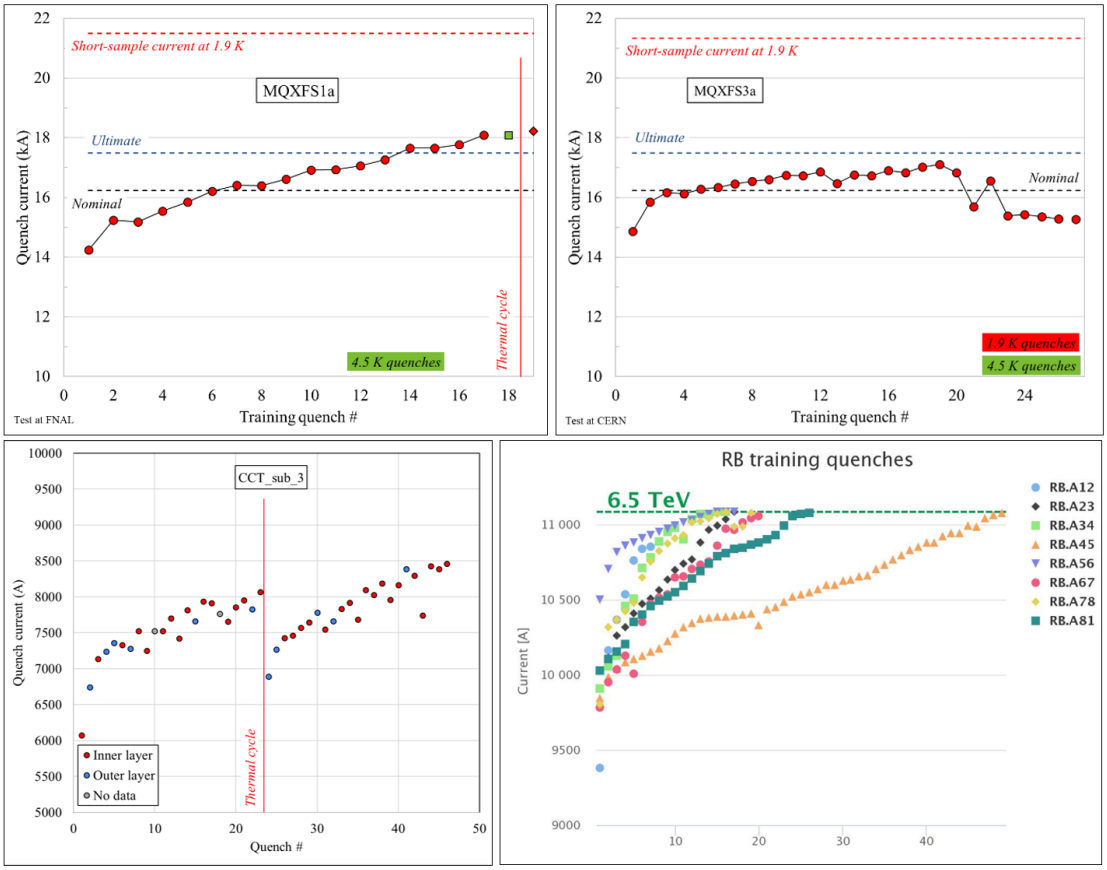

Fig. II.6.90: Examples of training, from top left clockwise: Nb_3Sn quadrupole magnet MQXFS01, Nb_3Sn quadrupole magnet MQXFS03, Nb_3Sn dipole magnet CCT_sub_3, and training of the 8 sectors, each composed by 154 Nb-Ti LHC MB dipole magnets.

expected to operate in the accelerator (so called nominal current). Then once installed in the collider, the magnet with full memory is not expected to undergo any quench during operation.

The second example in Fig. II.6.90 (top right) shows another magnet (the Nb_3Sn quadrupole magnet MQXFS03) whose quench performance is characterized by an initial increase in quench current (although slower than that of MQXS01), but with a sudden decrease after quench 18. This behaviour is called de-training, and it is the result of a degradation of the superconducting coil. Especially with strain sensitive conductor like Nb_3Sn, the strain induced by the Lorentz force on a not-well supported coil may damage the superconductor and results in a reduced quench current. Also, it is important to notice that, at the end of the training, the magnet reaches a degraded plateau, significantly lower than the short sample current. The third plot (Fig. II.6.90, bottom left) shows the training of the subscale CCT Nb_3Sn dipole magnet CCT_sub_3: the quench performance constitutes an example of erratic training, where the quench current does not increase monotonically, but it features several drops (fall-backs). Also, the magnet did not show full memory after a thermal cycle. This behaviour is often seen in CCT magnets, and it is attributed to the large number of surfaces where the cable is bonded via epoxy to the support structure (in a CCT, each cable is contained within a groove). The debonding and epoxy cracking in different regions of the coil may trigger a large number of quenches.

Finally, the fourth plot (Fig. II.6.90, bottom right) shows the training of the LHC. The LHC accelerator is subdivided in 8 octants, each of them composed by 1232/8=154 superconducting dipole magnets, each about 15 m long. The plot shows the training of each octant, with all the magnets in that octant connected in series, to a current corresponding to a 6.5 TeV collision energy. Each marker represents the quench in an individual superconducting dipole of the arc. The training is attributed to the lack of memory of some of the magnets, which were trained to nominal current in the CERN test facility before installation, but they required additional quenches to reach the target current once installed in the machine. In this case, we talk about partial loss of memory.

II.6.7 Conclusions

In this chapter, we provided a brief overview the science and technology of superconducting magnets for particle accelerators, starting from the motivations of their use in particle colliders and concluding with the training of the LHC magnets. As conclusive remarks, we would like to recall the key points discussed in this chapter with short statements and figures.

II.6.7.1 Particle accelerators and magnets

Dipole magnets are used in particle colliders to bend the trajectories of charged particles; quadrupole magnets are used to stabilize and focus the beam. The higher the field, the higher the collision energies and the focusing strength. In electro-magnets, the higher the field, the higher needs to be the current density in the coil. Superconducting materials allow reaching much higher current densities compared to normal conducting magnets.

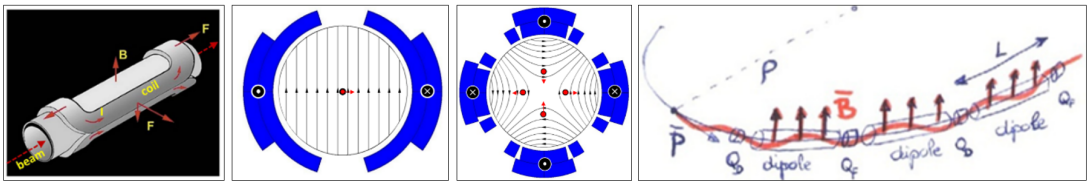

Fig. II.6.91: Particle accelerators and magnets.

II.6.7.2 Practical superconductors

In order to maximize their capability to be superconductive, superconductors need to operate below the critical surface. Practical superconductors are used in the form of strands with small twisted filaments (for minimizing flux jumps, magnetization and AC losses within the filaments and between the filaments) in a copper matrix (for stability and quench protection), and twisted in Rutherford cables (to minimize cable magnetization and AC losses, magnet inductance, strand unit length).

II.6.7.3 Magnetic design and coil fabrication

A perfect $\cos\theta$ current distribution produces a perfect dipole field. We simulate this current distribution with $\cos\theta$ coils, where the turns are combined in blocks separated by wedges. The coil width, or the

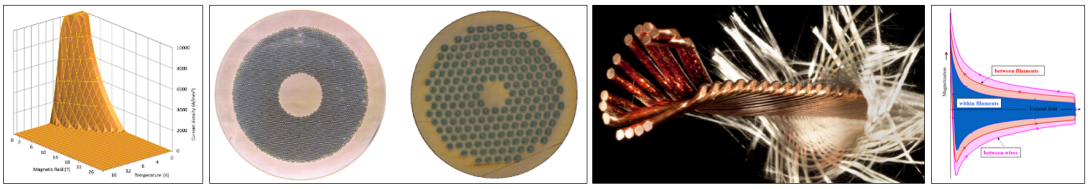

Fig. II.6.92: Practical superconductors.

number of layers, is proportional to the maximum field the coil can produce. The wedges, the positions and numbers of blocks are chosen to minimize field errors, and improve field quality. The iron is used to shield the flux lines and to increase the bore field for a given current. The Nb-Ti coil fabrication is characterized by winding and curing. In Nb_3Sn coils, heat treatment and impregnation steps are added.

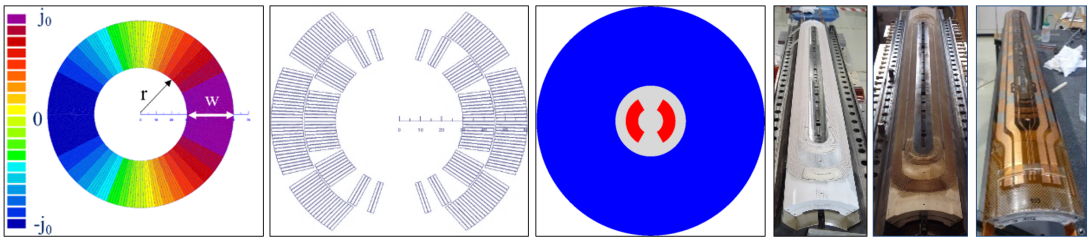

Fig. II.6.93: Magnetic design and coil fabrication.

II.6.7.4 Mechanical design and magnet fabrication

The e.m. forces push the turns of the coils vertically towards the mid-plane and horizontally outwards. In the end region, the coil ends are pushed longitudinally outwards. To minimized coil displacement during powering, pre-stress is applied. The support structure is often characterized by collars, iron yoke and stainless-steel shell. Alternative designs use aluminium shells pre-tensioned with bladders, and stress-managing coils to minimize coil stresses.

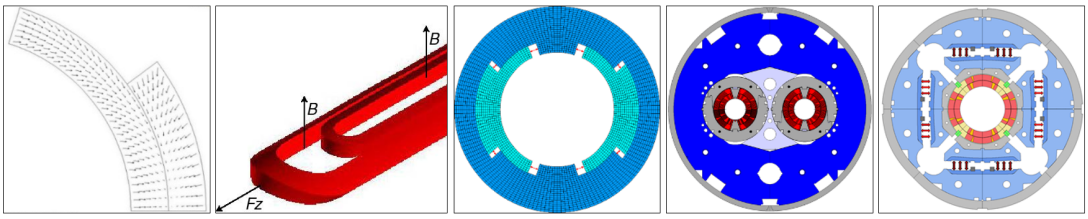

Fig. II.6.94: Mechanical design and magnet fabrication.

II.6.7.5 Quench, quench protection, and training

Quench is the irreversible transition of a superconductor from the superconducting state to the normal conducting state. When quench occurs, the coil starts dissipating heat and the coil temperature increases. To protect the coil from excessively high temperatures, the magnet is protected with quench heaters.

Training is the phenomenon consisting in the progressive increase in quench current during consecutive current ramps.

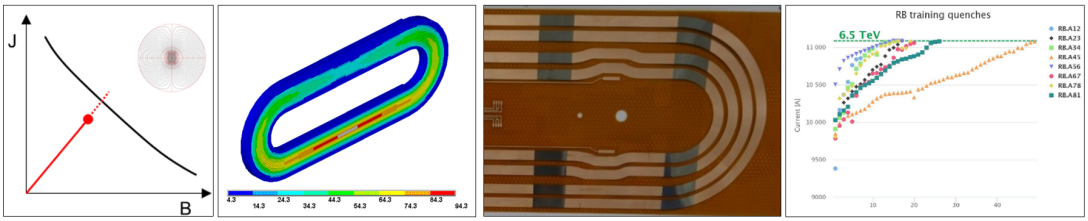

Fig. II.6.95: Quench, quench protection, and training.

II.6.8 Case study: design of an 11 T Nb_3Sn dipole magnet

CERN is considering an upgrade of its collimation system to enable proton and ion beam operation at higher intensities. To improve the collimation efficiency, additional collimators are foreseen in the room temperature insertions and in the dispersion suppression (DS) regions. To provide the required longitudinal space of about 3.5 m for additional collimators, a solution based on the substitution of a pair of 5.5-m-long 11 T dipoles with several 14.3-m-long 8.33 T LHC main dipoles (MB) is being considered. The goal of this case study is to design a Nb_3Sn superconducting dipole magnet with a 60 mm aperture and an operational field of 11 T, at 1.9 K and at 80% of the current limit I_{ss} .

II.6.8.1 Exercise 1: Critical curves

Question: Plot the critical curves (j_{sc} vs. B) for Nb_3Sn and Nb-Ti at 1.9 K.

For Nb-Ti, temperature and field dependence of B_{C2} and T_C use Lubell's formulae [19]

$$B_{C2}(T) = B_{C20}\left[1-\left(\frac{T}{T_{C0}}\right)^{1.7}\right] \quad , \tag{II.6.64}$$

$$T_C(B)^{\frac{1}{1.7}} = T_{C0}\left[1-\left(\frac{B}{B_{C20}}\right)^{\frac{1}{1.7}}\right] \quad , \tag{II.6.65}$$

where B_{C20} is the upper critical flux density at zero temperature (14.5 T), and T_{C0} is the critical temperature at zero field (9.2 K). Temperature and field dependence of j_c is given by Bottura's formula [20]

$$\frac{J_C(B,T)}{J_{C,\text{ref}}} = \frac{C_{\text{Nb-Ti}}}{B}\left[\frac{B}{B_{C2}(T)}\right]^{\alpha_{\text{Nb-Ti}}}\left[1-\frac{B}{B_{C2}(T)}\right]^{\beta_{\text{Nb-Ti}}}\left[1-\left(\frac{T}{T_{C0}}\right)^{1.7}\right]^{\gamma_{\text{Nb-Ti}}} \quad , \tag{II.6.66}$$

where $j_{C,\text{ref}}$ is the critical current density at 4.2 K and 5 T ($3000\text{A}/\text{mm}^2$) and $C_{\text{Nb-Ti}}$ (27 T), $\alpha_{\text{Nb-Ti}}$ (0.63), $\beta_{\text{Nb-Ti}}$ (1.0), and $\gamma_{\text{Nb-Ti}}$ (2.3), are fitting parameters.

For Nb_3Sn, temperature, field, and strain dependence of j_{sc} is given by Summers formulas [21]

$$J_C(B,T,\epsilon) = \frac{C_{\mathrm{Nb_3Sn}}(\epsilon)}{\sqrt{B}} \left[1 - \frac{B}{B_{\mathrm{C2}}(T,\epsilon)}\right]^2 \left[1 - \left(\frac{T}{T_{\mathrm{C0}}(\epsilon)}\right)^2\right]^2 \quad , \tag{II.6.67}$$

$$\frac{B_{\mathrm{C2}}(T,\epsilon)}{B_{\mathrm{C20}}} = \left[1 - \left(\frac{T}{T_{\mathrm{C0}}(\epsilon)}\right)^2\right] \left\{1 - 0.31 \left(\frac{T}{T_{\mathrm{C0}}(\epsilon)}\right)^2 \left[1 - 1.77 \ln\left(\frac{T}{T_{\mathrm{C0}}(\epsilon)}\right)\right]\right\} \quad , \tag{II.6.68}$$

$$C_{\mathrm{Nb_3Sn}}(\epsilon) = C_{\mathrm{Nb_3Sn,\,0}} \left(1 - \alpha_{\mathrm{Nb_3Sn}} |\epsilon|^{1.7}\right)^{\frac{1}{2}} \quad , \tag{II.6.69}$$

$$B_{\mathrm{C20}}(\epsilon) = B_{\mathrm{C20m}} \left(1 - \alpha_{\mathrm{Nb_3Sn}} |\epsilon|^{1.7}\right) \quad , \tag{II.6.70}$$

$$T_{\mathrm{C0}}(\epsilon) = T_{\mathrm{C0m}} \left(1 - \alpha_{\mathrm{Nb_3Sn}} |\epsilon|^{1.7}\right)^{\frac{1}{3}} \quad , \tag{II.6.71}$$

where $\alpha_{\mathrm{Nb_3Sn}}$ is 900 for $\epsilon = -0.003$, T_{C0m} is 18 K, B_{C20m} is 27.6 T, and $C_{\mathrm{Nb_3Sn,\,0}}$ is a fitting parameter equal to $43.1\,10^8 \mathrm{AT}^{1/2}\mathrm{mm}^{-2}$ for a $J_c = 2900 \mathrm{A/mm}^2$ at 4.2 K and 12 T. Assume $\epsilon = 0.000$.

Solution The critical curves are reproduced in Fig. II.6.96.

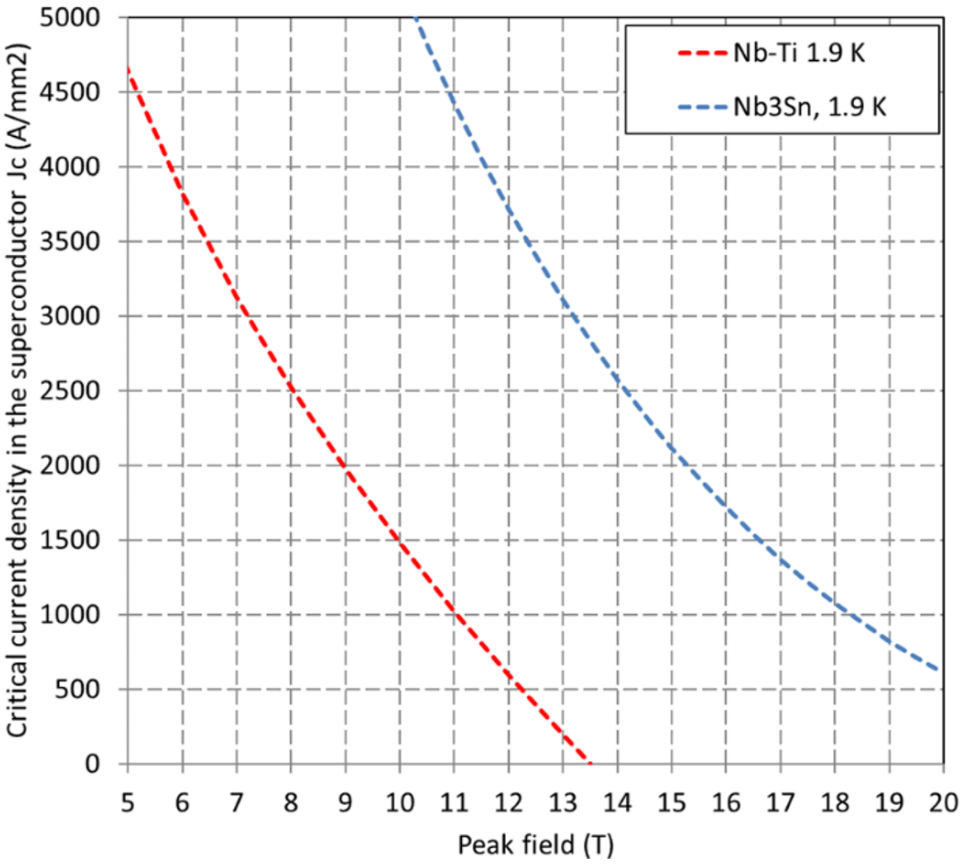

Fig. II.6.96: Critical curves of Nb-Ti and Nb_3Sn.

Table II.6.2: Parameters of the 11 T cable for exercise 2.

Nb_3Sn cable parameters	
N_{strand}	40
Strand diameter (mm)	0.7
Cable width (mm)	14.7
Cable inner thickness (mm)	1.149
Cable outer thickness (mm)	1.351
Keystone angle (degrees)	0.79
Insulation thickness (mm)	0.100
Cu %	54.5
Sc %	45.5
Cu/Non-Cu ratio	1.20
Area superconductor in cable (mm^2)	7.004
Area copper in cable (mm^2)	8.390
Area insulated cable (mm^2)	21.605
Filling factor	0.32

II.6.8.2 Exercise 2: Filling factor

Question

Determine the coil filling factor κ ($\frac{j_0}{j_{\text{sc}}}$ ratio or $\frac{A_{\text{non-Cu\_cable}}}{A_{\text{insulated\_cable}}}$), assuming a $\frac{\text{Cu}}{\text{non-Cu}}$ ratio of 1.2 and using the strand and the cable parameters from Fig. II.6.97.

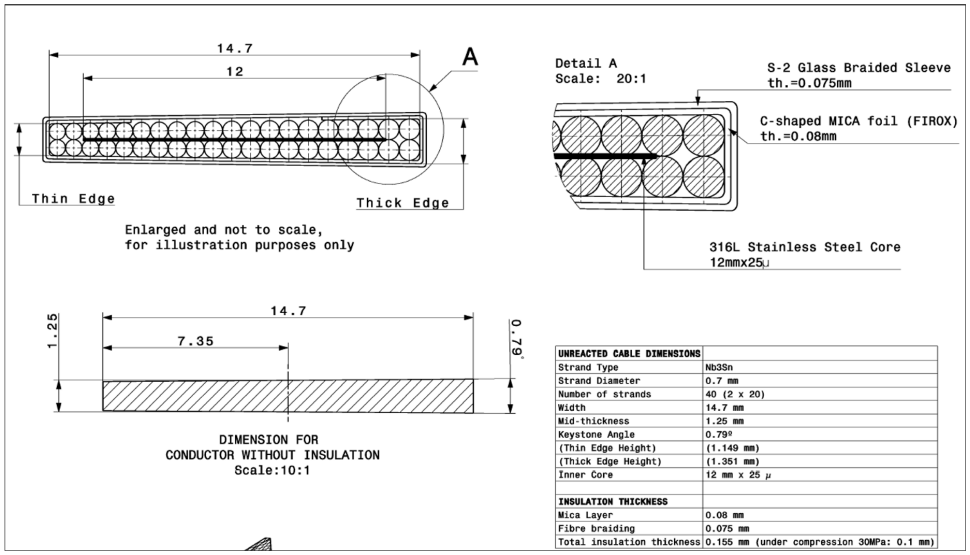

Fig. II.6.97: 11 T dipole cable parameters.

Solution

The filling factor is 0.32. The table 2 presents all the different cross-section areas of the cable. It is important to observe here that a Cu/non-Cu ratio of 1.2 corresponds to 54.5% of Cu and 45.5% of non-Cu.

II.6.8.3 Exercise 3: Load-line, coil size and margins with Nb_3Sn superconductor

Question:

Having determined the load-line (j_{sc} vs. B) for a sector coil (60°) with constant current density, and assuming:

1. The critical curve for Nb_3Sn of the previous exercise II.6.8.1,
2. An operational bore field B_{bore_op} of 11 T,
3. A load-line margin of 20% (I_{op}=80% of I_{ss}), and
4. A λ_{peak} (the ratio between the conductor peak field and the bore field) of 1.04,

determine:

1. The coil width w;
2. The superconductor and overall current densities, and bore and conductor peak field, both in operational conditions and at short-sample:
   operational j_{sc_op}, j_{0_op} , B_{bore_op} ,
   and Short sample B_{peak_op} j_{sc_ss} , j_{0_ss} , B_{bore_ss} , B_{peak_ss};
3. The temperature, superconductor current density and peak field margins at the operational conditions: T, j_{sc} , B_{peak} margins.

Solution:

With a $B_{bore\_op} = 11$ T, and assuming a 20% loadline margin, the B_{bore_ss} is equal to $B_{bore\_op}/0.8 = 13.75$ T. Then assuming a $\lambda_{peak} = 1.04$, the B_{peak_ss} is equal to $B_{bore\_ss}\,1.04 = 14.3$ T.

Using the critical curves plots of the previous exercise, one can see that at $B_{peak\_ss} = 14.3$ T, the $j_{sc\_ss} = 2460$ A/mm2. And using the formula of the sector coil (with a 60°angle)

$$B_1 = -\frac{2\,\kappa\, j_{sc}\mu_0}{\pi} w\, \sin\alpha \quad ,$$

$$B_{peak} = -\lambda_{peak}\frac{2\,\kappa\, j_{sc}\mu_0}{\pi} w\, \sin\alpha \quad .$$

One obtains a coil width of 25.25 mm, and the other results are

- $j_{sc\_ss} = 2460$ A/mm^2,
- $j_{0\_ss} = j_{sc\_ss}\lambda = 786$ A/mm^2,
- $B_{bore\_ss} = 13.75$ T,
- $B_{peak\_ss} = 14.3$ T,
- $j_{sc\_op} = 1965$ A/mm^2,
- $j_{0\_op} = j_{sc\_op}\lambda = 629$ A/mm^2,
- $B_{bore\_op} = 11$ T,
- $B_{peak\_op} = 11.44$ T.

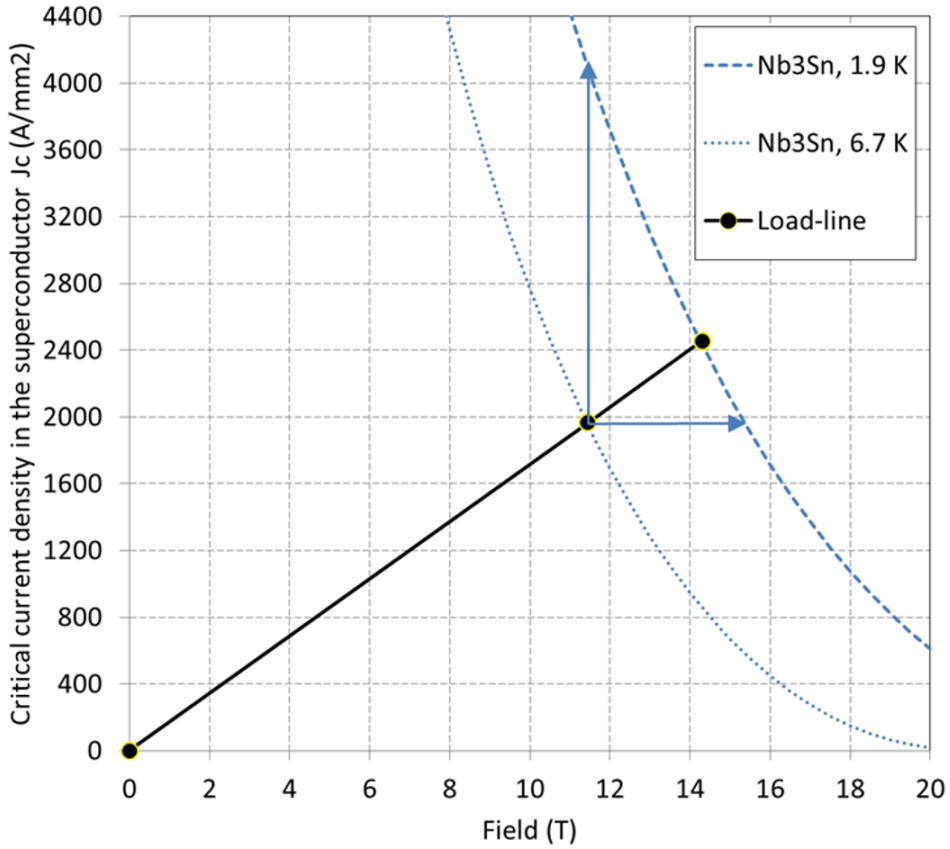

Fig. II.6.98: Load-line and margins of a sector coil with an 11 T operational bore field and Nb_3Sn superconductor.

The current density and field margin are estimated by respectively moving on the plot vertically and horizontally towards the critical curve. The temperature margin is obtained by increasing the temperature in the parametrization formula until the operational point is crossed. Therefore:

- $j_{\text{sc\_margin}} = 2140$ A/mm^2,
- $B_{\text{peak\_margin}} = 4$ T,
- $T_{\text{margin}} = 6.7$ K.

II.6.8.4 Exercise 4: Load-line, coil size and margins with Nb-Ti superconductor

Question:

Compare the "short sample" at 80% of I_{ss} operational conditions and margins if the same design uses Nb-Ti superconducting technology (use the parametrization curve of exercise II.6.8.1 reproduced in Fig. II.6.96) with the same coil size w.

Solution:

Using a coil width the same width as in the previous exercise (25.25 mm), one gets

- $j_{\text{sc\_ss}} = 1660$ A/mm^2,

- $j_{0\_ss} = j_{sc\_ss}\,\lambda = 532$ A/mm^2,
- B_{bore_ss} = 9.3 T,
- B_{peak_ss} = 9.7 T,
- j_{sc_op} = 1330 A/mm^2,
- $j_{0\_op} = j_{sc\_op}\,\lambda = 425$ A/mm^2,
- B_{bore_op} = 7.45 T,
- B_{peak_op} = 7.74 T,
- J_{margin} = 1370 A/mm^2,
- B_{margin} = 2.5 T,
- T_{margin} = 2.1 K.

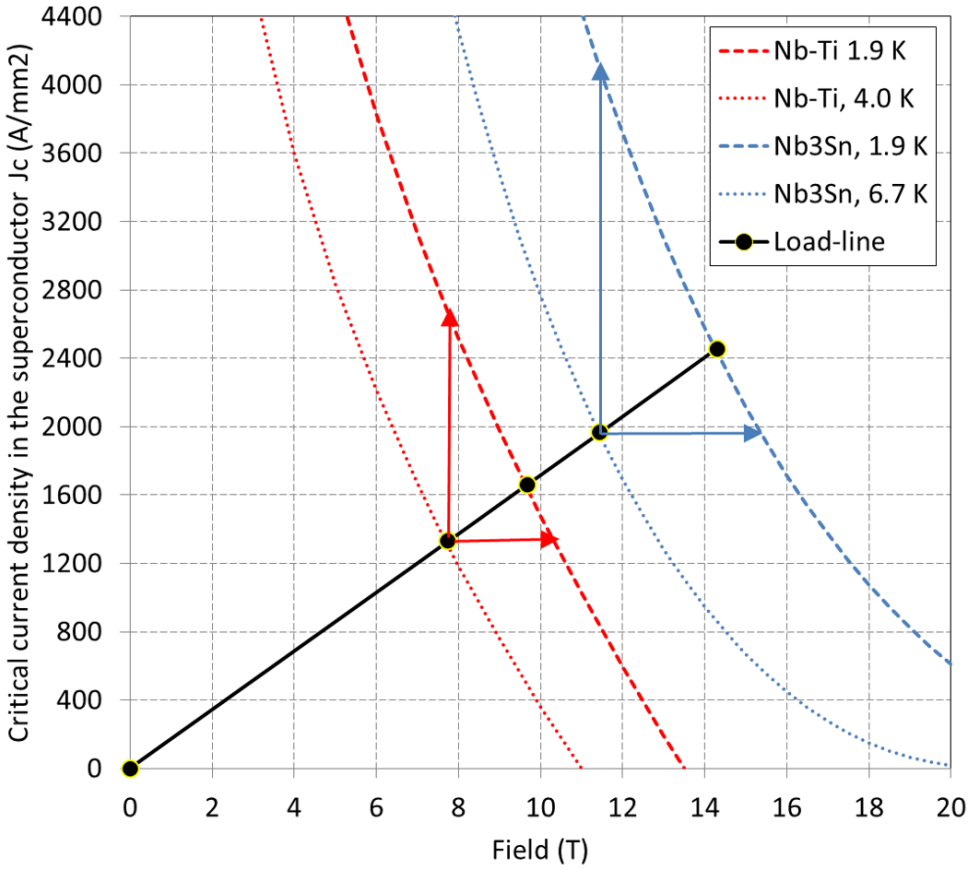

Fig. II.6.99: Load-line and margins of a sector coil with an 11 T operational bore field and Nb-Ti superconductor (Curves superimposed on the plot of Fig. II.6.96.)

II.6.8.5 Exercise 5: Forces and stresses

Question:

Determine e.m forces F_x and F_y and the accumulated stress on the coil mid-plane in the operational conditions with sector coil approximation.

Solution:

In the operational conditions ($B_{\text{bore\_op}}$ = 11.0 T)

- F_x (quadrant) = +2.29 MN/m,
  F_x (total) = +4.60 MN/m = 460 t/m,
- F_y (quadrant) = −2.10 MN/m.

The accumulated stress on the coil mid-plane is shown in Fig. II.6.100.

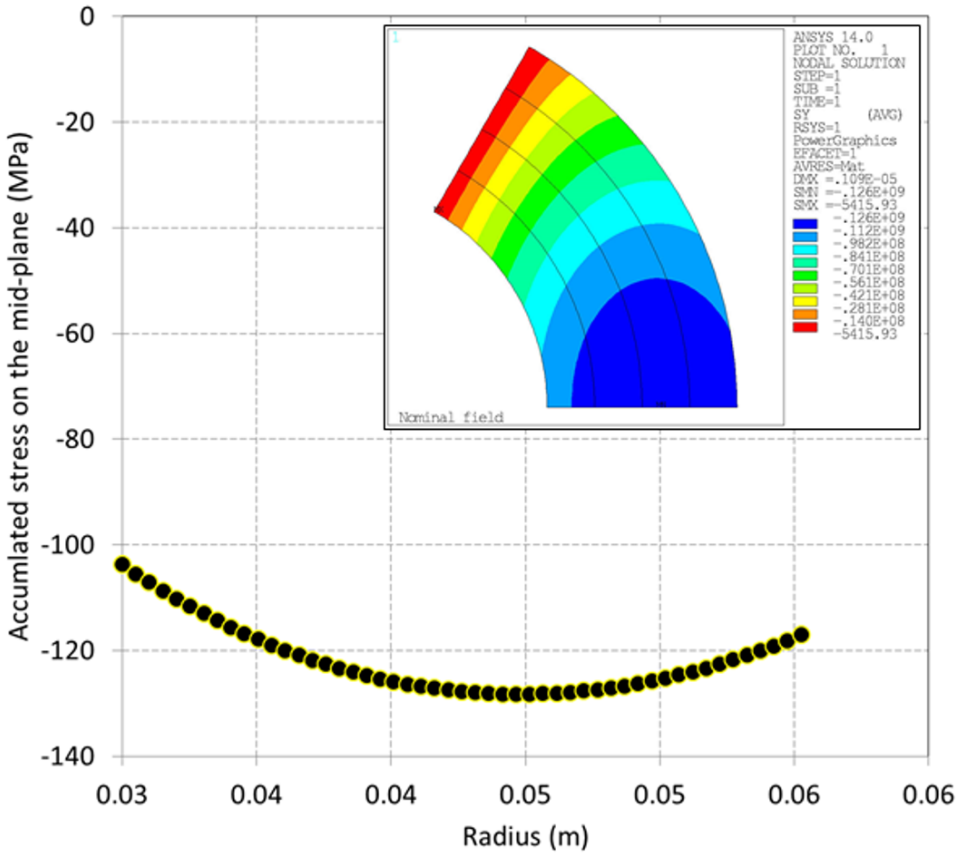

Fig. II.6.100: Azimuthal stress on the mid-plane as a function of the radial position. In the inset, plot of azimuthal stress in the sector coil computed by a finite element model.

II.6.8.6 Exercise 6: Support structure

Question:

Evaluate the dimensions of the iron yoke, and of the shrinking cylinder, assuming that the support structure is designed to reach 90% of I_{ss}. Assume a collar thickness of 25 mm (see overview of collared structure in Fig. II.6.101). Also, assume that the stainless-steel shell will close the yoke halves with the same force as the total horizontal e.m. force at 90% of I_{ss}. We assume an azimuthal shell stress after cool-down of $\sigma_{\theta\_\text{shell}} = 200$ MPa.

Solution:

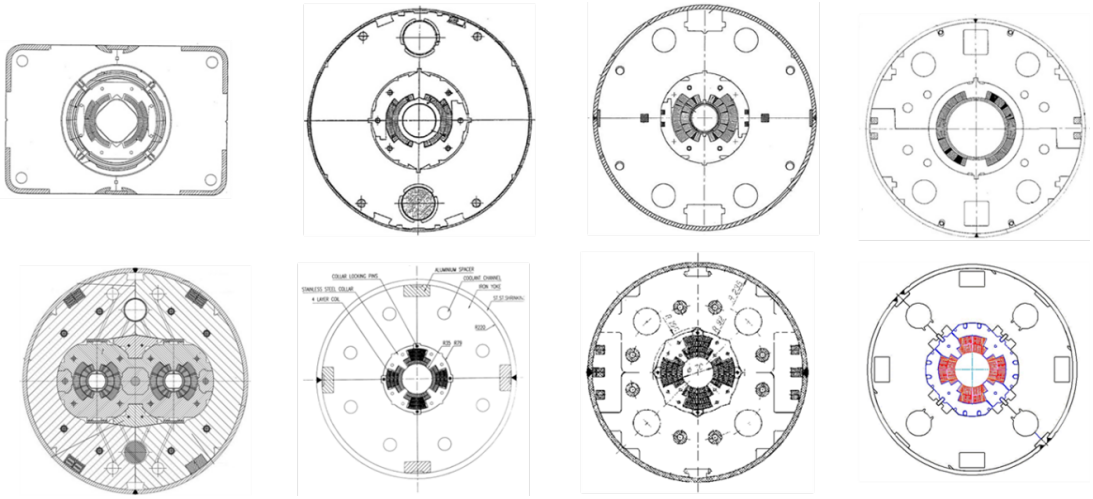

Fig. II.6.101: Overview of different support structures based on collars.

The iron yoke thickness can be estimated with the formula

$$r\,B_{\mathrm{bore}} \sim t_{\mathrm{iron}}\,B_{\mathrm{sat}} \quad .$$

Therefore, being B_{bore} = 12.2 T (at 90% of I_{ss}), r = 30 mm and B_{sat} = 2 T, we obtain $t_{\mathrm{iron}} \sim$ 190 mm. Then, using the assumption that the shell will close the yoke halves with the same force as the total horizontal e.m. force at 90% of I_{ss} , we have

$$F_{x\_\mathrm{total}} = F_{x\_\mathrm{quadrant}}\,2 = +6.8\ \mathrm{MN/m} \quad .$$

Assuming an azimuthal shell stress after cool-down of $\sigma_{\mathrm{shell}} = 200$ MPa, the thickness of the shell is

$$t_{\mathrm{shell}} = F_{x\_\mathrm{total}}/2/1000/\sigma_{\mathrm{shell}} \sim 17\ \mathrm{mm} \quad .$$

By combining all the results of the analytical model, we can now compare the final results with the ones of a real 11 T dipole (see Fig. II.6.102).

One can see how from simple formulas, we can obtain a preliminary design of the magnet, with reasonable parameters compared to the final design.

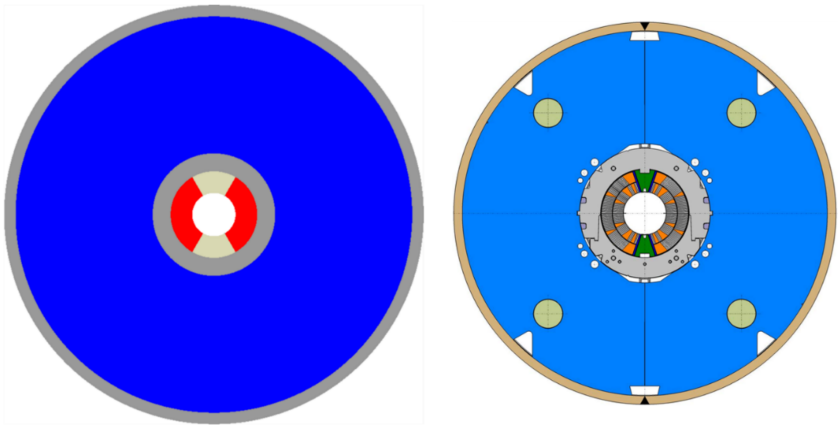

Fig. II.6.102: The 11 T dipole.

References

[1] P. Ferracin, E. Todesco and S. Prestemon, Superconducting accelerator magnets, US Particle Accelerator School, www.uspas.fnal.gov.

[2] E. Todesco, "Masterclass - Design of superconducting magnets for particle accelerators", https://indico.cern.ch/category/12408/.

[3] M.N. Wilson, Superconducting magnets, Clarendon Press, Oxford, 1983.

[4] K.H. Mess, P. Schmuser and S. Wolff, Superconducting accelerator magnets, World Scientific, Singapore, 1996.

[5] F.M. Asner, High Field Superconducting Magnets, Oxford Science Publication, 1999.

[6] A. Devred, Practical Low-Temperature Superconductors for Electromagnets, CERN Yellow Report, CERN-2004-006, 2004.

[7] S. Russenschuck, Analytical and Numerical Methods for Electromagnetic Design and Optimization, WILEY-VCH Verlag GmbH & Co. KGaA, 2010.

[8] S. Izquierdo Bermudez, Field Quality in Nb_3Sn Superconducting Accelerator Magnets, PhD thesis, Universidad Politecnica de Madrid, 2023.

[9] D. Schoerling and A. Zlobin, Nb_3Sn Accelerator magnets, Eds. Berlin, Germany: Springer, 2019, doi:10.1007/978-3-030-16118-7.

[10] LHC design report v.1: the main LHC ring, CERN-2004-003-v-1, 2004.

[11] WAMSDO 2013: Workshop on Accelerator Magnet, Superconductor, Design and Optimization, edited by E. Todesco, CERN Yellow Report CERN-2013-006, 2013.

[12] C.P. Bean, "Magnetization of High-Field Superconductors", Rev. Mod. Phys. 36, 31, 1 January 1964.

[13] B. Bordini *et al.*, "Impact of the Residual Resistivity Ratio on the Stability of Magnets", IEEE Trans. Appl. Supercond., VOL. 22, NO. 3, JUNE 2012 4705804.

[14] B. Bordini, Thermo-Magnetic Instabilities in Superconducting Accelerator Magnets", Fermilab-thesis-2006-45.

[15] A. Devred, "Quench origins", AIP Conference Proceedings 249, edited by M. Month and M. Dienes, 1992, p. 1309-1372.

[16] A.K. Ghosh *et al.*, "Minimum quench energies of Rutherford cables and single wires", IEEE Trans. Appl. Supercond. , Vol. 7, No. 2, June 1997, pp. 954–957.

[17] Brechna, *et al.*, Proceedings of the 6th International Conference on Magnet Technology, 1978. p. 597.

[18] Y. Iwasa, "Mechanical disturbances in superconducting magnets – A review", IEEE Trans. Magn., Vol. 28, No. 1, January 1992, pp. 113–120.

[19] M.S. Lubell, "Empirical scaling formulas for critical current and critical fields for commercial NbTi", IEEE Trans. Magn., Vol. MAG-19 No. 3, pp. 754–757, 1983.

[20] L. Bottura, "A practical fit for the critical surface of NbTi," IEEE Trans. Appl. Supercond., Vol. 10, No. 1, pp. 1054–1057, 2000, doi:10.1109/77.828413.

[21] L.T. Summers, M.W. Guinan, J.R. Miller and P.A. Hahn, "A model for the prediction of Nb_3Sn critical current as a function of field, temperature, strain and radiation damage," IEEE Trans. Magn., Vol. 27, No. 2, pp. 2041–2044, 1991.